Topological states on surfaces and interfaces of perovskite transition metal oxides

Manali Vivek

université PARIS-SACLAY

NNT: 2018SACLS216

Thèse de doctorat

UNIVERSITÉ PARIS SUD
Comprendre le monde, construire l'avenir

États topologiques aux surfaces de perovskites d'oxydes de métaux de transition

Thèse de doctorat de l'Université Paris-Saclay
préparée à l'Université Paris-Sud

École doctorale n°564 Physique en Ile-de-France (PIF)
Spécialité de doctorat : Physique

Thèse présentée et soutenue à Orsay, le 05/09/2018, par

Manali Vivek

Composition du Jury :

Anuradha Jagannathan Professeur, Laboratoire de Physique des Solides, Orsay	Présidente du Jury
Giovanni Sordi Professeur, Royal Holloway University of London, Egham	Rapporteur
Jérôme Cayssol Professeur, Laboratoire Ondes et Matière d'Aquitaine, Bordeaux	Rapporteur
Jacek Goniakowski Directeur de Recherche, Institut des Nanosciences de Paris, Paris	Examinateur
Jean-Marc Triscone Professeur, Université de Genève	Examinateur
Marc Gabay Professeur, Laboratoire de Physique des Solides, Orsay	Directeur de thèse
Mark-Oliver Goerbig Directeur de Recherche, Laboratoire de Physique des Solides, Orsay	Invité

Titre : États topologiques aux surfaces de perovskites d'oxydes de métaux de transition.

Mots clés : topologie, oxydes, métaux de transition, surfaces, interfaces

Résumé : Le sujet de la topologie dans les oxydes, en particulier à la surface des oxydes de perovskite comme $SrTiO_3$, ou à l'interface de $LaAlO_3$ / $SrTiO_3$ sera étudié dans cette thèse. Les deux materiaux, à leurs surfaces orientées (001), contiennent un état métallique limité à quelques nanomètres de la surface. De plus, nous montrerons qu'il existe certaines croisements de trois bandes autour desquelles des perturbations vont provoquer l'apparition d'un spectre de bandes inversées et gappées. Ceux-ci conduiront à des états de bord topologiques qui peuvent être détectés via la supraconductivité induite comme dans le cas des puits quantiques topologiques ou des nanofils des supraconducteurs-semi-conducteurs.
Ensuite, la surface orientée (111) de $LaAlO_3$ / $SrTiO_3$ sera étudiée lorsque les mesures de transport de Hall révèlent une transition de un à deux porteurs par dopage électrostatique. Une explication basée sur un modèle de liaison fortes incluant des corrélations U de Hubbard sera proposée, ce qui donnera lieu à des croisements de bandes entre les sous-bandes favorisant les états topologiques.
Enfin, une étude ab-initio de $CaTiO_3$ sera effectuée pour expliquer l'état métallique qui existe à sa surface (001) orientée et pour prédire le magnétisme dans le système. $CaTiO_3$ est différent des autres composés étudiés précédemment, en raison de la grande rotation et de l'inclinaison des octaèdres d'oxygène entourant le Ti, ce qui complique les faits. La structure avec et sans lacunes d'oxygène sera étudiée en profondeur pour fournir des détails sur la bande de conduction et leurs caractères orbitaux.

Title : Topological states on surfaces and interfaces of perovskite transition metal oxides

Keywords : topology, transition metal oxides, surfaces, interfaces

Abstract : The subject of topology in oxides, in particular at the surfaces of perovskite oxides like $SrTiO_3$, or at the interface of $LaAlO_3$ / $SrTiO_3$ will be investigated in this thesis. Both compounds, at their (001) oriented surfaces, contain a metallic state confined to a few nanometers at the surface. In addition, we will show that there exist certain three band crossings around which perturbations will cause an inverted and gapped band spectrum to appear. These will lead to topological edge states which can be detected via induced superconductivity as in the case of topological quantum wells or superconductor-semiconductor nanowires.
Next, the (111) oriented surface of $LaAlO_3$ / $SrTiO_3$ will be studied where Hall transport measurements reveal a one to two carrier transition via electrostatic doping. An explanation based on a tight binding modelling including Hubbard U correlations, will be proposed which will give rise to band crossings between sub-bands promoting topological states.
Finally, an ab-initio study of $CaTiO_3$ will be performed to explain the metallic state which exists at its (001) oriented surface and to predict magnetism in the system. $CaTiO_3$ is different from the other compounds studied previously, due to the large rotation and tilting of the oxygen octahedra surrounding the Ti, which complicates the picture. The structure with and without oxygen vacancies will be studied in-depth to provide details about the conduction band and their orbital characters.

Université Paris-Saclay
Espace Technologique / Immeuble Discovery
Route de l'Orme aux Merisiers RD 128 / 91190 Saint-Aubin, France

Topological states at the surfaces and interfaces of perovskite metal oxides

Manali Vivek

September 24, 2018

Acknowledgements

This PhD would not have been possible without the support of the most wonderful people that I met and whom I have had the opportunity to interact with during the course of these three odd years.

Firstly, I would like to thank Marc Gabay, who while overseeing my master's internship, saw in me, a future PhD student. During these three years that we have worked together, you have been a true mentor, guide and philosopher, never losing your patience with me and always being there to answer my incessant questions. While giving me the opportunity to work on different projects with varied people and enabling me to teach with you, you have instilled in me a hunger for knowledge and an enormous amount of patience. You have also taught me the art of paying attention to minute details. Thank you for the continued support, even in my decision to not pursue a career in Physics.

Secondly, a big thank you to the Theory group of LPS, who took me in when I was a Master's student and have always made me feel a part of the group, no matter how much more experienced or senior they were. Thanks to Mark for all the discussions we have had, physics or otherwise and here is hoping you come around to giving a SIESTE in my memory someday. I will never forget your hearty laugh which resonated in the corridors and your limitless knowledge about any subject (and also your wonderful sense of humour). Fred, Gilles and Jean-Noel, thanks for being there whenever I needed to ask a stupid question and for making me feel like a part of the group. A heartfelt thank you to the other members of the group, be it the administrative side comprising Sophie, Veronique and Marie-France, who have always helped me no matter what or the scientific side, with Giuseppe, Rik and Claudia, who have been very welcoming.

Thirdly, all the collaborators like Jean-Marc Triscone, Jacek Goniakowski and Andres Santander, among many other who have helped me immensely with their inputs and their advice.

Next, I need to thank all my friends who were my lab mates or vice versa, who have made these three years extremely enjoyable with the numerous tea (and not coffee) breaks where all kinds of varied discussions have been had. Be it scientific or worldy problems,

we have found solutions for most things together. A special mention to Vardan Kaladzhyan and Serguei Tchoumakov who have been my best mates and with whom we have explored many restaurants in Paris, all the while discussing Landau levels and Majoranas and with whom many clandestine tea breaks have been taken. Nicolas Mace, you have been the most awesome office mate, even if it was for a very short time and I will always remember the discussions we had, be it for brainstorming for the PhD gifts of others or even life after PhD. Thank you for also being a constant for all the soiree thesards that I have organised and for being the calm and joyous person that you are. For my ex-office mates, Arnaud, who I can now talk to despite his over achieving and awe-inspiring self, Fred, for being the only other PhD student in my year in the Theo group and for teaching me Hanabi and Yunlong, who has been my personal Mathematica bible, thank you for kicking me out of the office. Thank you also to my current office mate, Susana, for being such a bubbly, happy and wonderful person, it was a great pleasure to be your friend and hope we validate many more Mexican restaurants in Paris in the future. Hope you get more work done with us not talking all the time in the office. A shout out also to Rebecca for being so happy and cheerful all the time and to Sebastien, Mircea, Hridis, Olesia and Andrej among all the other wonderful people that I met in LPS for making me feel at home even when I was just a first year and for all the trips back and forth on the RER, which was made bearable because of your awesome company. Thank you Maxime for being a great first year and for all the fun that we have had, including printing n copies of my thesis from your computer. A big thank you to Anais, Thibaut, Stephanie, Marion and Marceau for first showing me the ropes and then helping me to organise the PhD weekends. It has been great fun working with you and hope we continue this tradition we started.

I would also like to thank my Master's friends, specially Ines, who has always been there to help me understand concepts about Physics or about life and for also being part of our dance troupe, Paris Panga. A heartfelt thank you to the Paris Panga members, Oza, Samta, Aditya, Samarth and Anirudh with whom a deep bond of friendship was forged while discussing physics while dancing and all the other members with whom it was a pleasure collaborating and dancing.

I cannot thank my parents, Aseem and Sarika, enough, for always being there for me,

teaching me how to dream and then how to achieve them. Thank you for always supporting me in my decisions, be it encouraging me to go to France and then pursue my Masters and PhD here or later leaving Physics and working here in Paris. Thank you for being my pillars of support, both emotional and physical, and for spending hours talking over Skype, advising me how to deal with life or planning trips to Europe. My younger brother, Varun, also deserves a special mention in tolerating my rants and monologues and giving the best non-baby brother-like advice. A heartfelt thank you to my two grandmothers and the rest of my family who have always encouraged me to pursue my dreams.

A special thank you to Neeraj, Paula and Matteo for being the best friends, confidantes and conspirators that one needs and only hopes to find.

Resume in English

Materials science has shown great progress in the recent years leading to a revival in the interest of the scientific community with new and novel phases of matter being discovered.One of the possible candidates to substitute conventional materials are transition metal complexes, displaying exotic phases promoted by strongly correlated electronic phenomena which have been recently unearthed. In *transition metal complexes* the d orbitals are partly filled, which is different from conventional materials which comprise of mostly s or p electrons. This difference has a great effect on the electronic and structural properties of transition metal complexes. Of the transition metal compounds which are of interest, oxides provide an excellent playground to probe the interplay between the different degrees of freedom present, be it kinetics and/or correlations among electrons, orbital dichotomy or multiple valence states of the d orbitals. Ranging from simple binary oxides like ZnO, a transparent conductor or the more complex quaternary compounds like $YBa_2Cu_3O_7$, a high temperature superconductor, TMO provide varied functionalities.

However, we shall focus on the simpler ternary oxides like $SrTiO_3$ (STO) which belong to the family of perovskite compounds. These have an ABO_3 type of stoichiometry with the A and B cations being surrounded by an oxygen octahedron cage which creates crystal field splitting of the d orbitals into two groups- a lower energy t_{2g} and a higher energy e_g.STO, a perfect cubic crystal, has a host of interesting bulk properties - when stochiometric, it is a quantum para-electric insulator, when doped, it becomes a superconductor [3] and under strain, it transforms to a ferroelectric. We also know that the ideal cubic lattice, such as STO, can accomodate different sizes of the A and B cation for the perovskites. Despite this fact, when the size of A and B cations is changed, the lattice undergoes different types of structural distortions which lower its symmetry. Replacing Sr with a smaller cation like Ca, leads to an antiferrodistortive ordering, where successive oxygen octahedra undergo out of phase rotations. If Sr is replaced by a larger atom, like Ba, the oxygens tend to move away from it and generate a dipole, giving rise to ferro-electricity. From these examples, it is clear that the oxygen octahedra play an important role in the functionality of a material.

At the interfaces or the surfaces of these compounds, new behaviour is expected to emerge, as various symmetries are broken. Interfaces can be realised with different members of the perovskite TMO family, owing to their structural compatibility, leaving the field

open to heterostructures. An important effect is the breaking of inversion symmetry at the surface or even at the interface, which will mean that the Bloch theorem is no longer valid for one particular direction. If spin-orbit coupling is added to the inversion symmetry breaking, a new interaction in the form of Rashba interaction arises.Interestingly enough, the strength of the Rashba coupling can be tuned with an electric field in the case of a heterostructure of $LaAlO_3/SrTiO_3$ (LAO/STO) where a steep rise in the Rashba coupling is noticed as the transition from an insulating to superconducting takes place [29].

However, this interaction can also be present in semi-conductors or insulators which sometimes lead to surface states with novel properties as in the case of topological insulators like Bi_2Se_3 and Bi_2Te_3 [30, 31]. The two main families exhibiting topological properties are materials showing band inversion driven by SOC and those where crystalline symmetry is important. But topological states are not just limited to conventional semiconductors or insulators and can even be present in TMO. Interfaces or surfaces inherently satisfy the condition of breaking of inversion symmetry and if they also possess the Rashba interaction, with a band inversion, they could become a playground for topological states. Not only this, but if symmetry arguments are to be taken into account, then the $(1\,1\,1)$ surfaces of certain TMO can show topological states [35] where band inversion is not even needed.

A new class of materials, that of topological metals will be further investigated with a detailed discussion on the topological states present at the surface of STO in the $(0\,0\,1)$ orientation where a 2DEG already exists and the co-existence of topology with the metallic gas will be explored. For the possible experimental detection, certain gedanken (thought experiments) will be proposed, opening the discussion for favouring topological states over the metallic gas and even inducing topological superconductivity at the surface.

The only interesting orientation will not be the $(0\,0\,1)$ as was already explained above, the $(1\,1\,1)$ orientation can also possibly host topology. In that respect, the parent compound of STO, LAO/STO will be explored in the $(1\,1\,1)$ orientation where strange transport properties are measured in Hall measurements. Normally, with gating or increase of the carrier concentration, one would expect to find more and more carriers. However, much to everyone's chagrin, multi-band transport is seen and the carriers being populated in a new band

at the expense of carriers in the original band measured at low gate voltages. It will be shown that correlations and the quantum confinement at the surface will play a very important role in explaining this strange behaviour. The role of topology will also be discussed in this framework to see if both the multi-band transport and topology can co-exist. However this question of correlations is not limited to LAO/STO and another material $CaTiO_3$ (CTO) will also display a 2DEG in the presence of correlations. However in this case, the correlations will drive a metal-insulator transition and show signatures of magnetism at the surface. This will open up the debate for the co-existence or competition between magnetism and topology owing to the localised preference of magnetism and the delocalised preference of topological edge states. This question also is present for STO where reports of magnetism have surfaced and the reason for the existence of the 2DEG might not be so clear. Another question which can be asked is that of topology at the surface of CTO which remains unanswered.

The thesis has been organised as follows- the first chapter will deal the important issue of topology and will serve as a guide for the kinds of topologies seen in the systems under study. Once the different classes of topological materials, be it spin-orbit protected Topological insulators, Topological Crystalline insulators, have been introduced in 2D and 3D, the surface states, if any, will be discussed. Next, we will talk about topology as applied to TMO and will focus on the issue of topological surface states co-existing with metallic surface states for the case of TMO.

The second chapter will consist of a detailed tight binding analysis of the $(0\,0\,1)$ oriented surface of $SrTiO_3$, beginning with a general introduction to the elements which will be needed, like tight binding formulation, crystal field and bulk spin-orbit coupling (SOC). It will then continue to explain the bulk and surface properties of $SrTiO_3$ experimentally observed, and in particular, the metallic state found at the surface. Next, a theoretical modelling will be proposed inclusive of certain surface induced perturbations like the confinement potential and the orbital mixing both of which will be explained in great detail in order to better understand their impact. The effects of all the perturbations mentioned before will then be seen on the band structure as they are added step by step, leading to inverted and gapped bands. This band inverted structure will then be variationally mapped

to a Bernevig, Hughes, Zhang (BHZ) [42] Hamiltonian and be solved for edge states. Finally, the topological signatures of phase winding and edge states will be discussed. A similar system, LAO/STO, in the $(0\,0\,1)$ orientation will also be discussed and a similar modelling will be done. Similar topological signatures will then emerge and a proposal of the experimental detection of these states will be made. [79]

The third chapter will continue with LAO/STO but at a different orientation, the $(1\,1\,1)$, where a 2DEG exists and anomalous transport measurements have been revealed. As the carrier concentration is tuned with a gate voltage, one band gets populated. On increasing the carriers in the system, another band starts getting populated at the expense of the first one. Theoretical modelling of this system will first try to understand the differences induced due to the $(1\,1\,1)$ orientation which leads to a hexagonal structure if two layers of Ti atoms are projected along the $(1\,1\,1)$ plane. Terms like inter and intra layer coupling between the Ti layers, bulk SOC and trigonal crystal field will be added. The odd experimental behaviour will be explained by inspecting the sub-band structure seen in Poisson Schrodinger calculations due to the confinement at the surface and adding it to the tight-binding modelling. The introduction of correlations in the form of a Hubbard U will be needed in order to explain the band inversion. Two sub-bands close to the Fermi Energy (E_F), due to the quantum confinement of the gas at the surface, will contribute to the inversion of the two electron-like band population. During this investigation, certain band crossings will be unearthed which when mixed with certain perturbation terms will give rise to unexpected topological states.

The final chapter will consist of a detailed ab-initio study of another compound CTO at its $(0\,0\,1)$ orientation, which will prove to be very different and yet similar to STO. It is known that bulk CTO has certain tiltings and rotation of the octahedra which might have an impact on its electronic properties. Experimental studies have revealed a 2DEG at its $(0\,0\,1)$ surface in the presence of oxygen vacancies and comparisons to the gas present at the STO $(0\,0\,1)$ oriented surface will be made. A strong hybridization of the Fermi Surface (FS) indicates a hybridization of the orbitals involved, notably the five d orbitals of Ti. The band structure also indicates a different effective mass as compared to the bands observed in STO. An ab-initio study will then be carried out in the bulk to asses the impact of the

structural distortions on the electronic structure. Once the bulk is characterised, a surface slab will be investigated with the possibility of having some defects and its electronic properties investigated. The impact of defects will lead to a metallic state at the surface and a localised state at the gap, both of which are present in the ARPES study done by Tobias et al [25] and Muff et al [129]. The metallic state at the surface will be characterised and the possibility of magnetism at the surface also delved into. Topology in this system, will only rest as a perspective and one can only hope to inspire future studies for topological states in CTO.

To conclude with, certain perspectives on all three systems, STO, LAO/STO and CTO will be discussed and future work on similar systems laid down some of which are explained below.

While the interfaces and surfaces proved to be interesting beasts on their own when compared to the bulk, there are still mysteries to be understood. For example, surface rumplings, which try to compensate for the polarity of the surfaces, inadvertently play a part in removing the degeneracy of the bulk bands and also introduce the necessary element for band inversion. But could there be other effects hitherto not thought of? For example, defects or vacancies are seen to be important players in creating a confinement potential in the case of STO but in the case of LAO/STO, this is just one of the possible mechanisms at play. Could there be a way to distinguish the vacancies as the sole mechanism responsible for the gas? [142, 16]

In LAO/STO, there exists another interesting line of thought- addition of capping layers to reduce the number of LAO layers required to create the metallic state. Ab-initio studies have shown that using metallic capping layers can make this possible [143]. Experimental work has already been done in this direction by using capping layers of metals to reduce the number of LAO layers required, albeit for the purpose of making spin pumping effective to make possible spintronic devices [144, 145]. One of the mecanisms proposed to explain this phenomena is the oxidation of the metal capping layer. The metal present will oxidise itself by sucking oxygen out of the LAO layer, thus creating vacancies in the topmost LAO layer, liberating electrons which then form the 2DEG. This neat idea has already been used in the case of the (001) STO surface by Santander et al to create the 2DEG [83].

Instead of using metals, another idea is to use layers of STO as capping layers. In order to explore this line of thought, we are trying to work on capping layers of STO, which translates into using STO twice, once as a substrate and another as the capping layer itself. Preliminary experiments have shown that such a scenario is indeed possible [146] where only 4 unit cells are needed (n of LAO and m of capped STO where n+m=4). Preliminary DFT studies however do not find this behaviour and seem to suggest insulating behaviour for 1 unit cell thick LAO capped with STO. The origin of this behaviour as to why STO is an effective means to reduce the number of LAO layers needed, should be studied further, by the means of ab-initio studies and it is possible that surfaces or interfaces might again play an important role. And where surfaces or interfaces enter, topology again might manifest itself which could be another avenue to be explored.

In all, topology and transition metal oxides are inextricably linked and could provide a rich playground to probe for novel properties of matter.

Resume en français

La science des matériaux a connu de grandes avancées, marquées par la découverte de nouvelles phases de la matière, conduisant à un intérêt renouvelé de la communauté scientifique pour ce type d'activité. Parmi les candidats possibles appelés à remplacer les matériaux traditionnels, on compte les composés de métaux de transition pour lesquels des phases exotiques et des phénomènes découlant de leurs fortes corrélation électroniques ont été récemment mis en lumière. Dans les *complexes de métaux de transition* les orbitales d sont partiellement remplies, ce qui est différent des matériaux conventionnels qui comprennent principalement des électrons s ou p. Cette différence a un grand effet sur les propriétés électroniques et structurelles des composées de métaux de transition. Dans cette catégorie, les oxydes (TMO) constituent un excellent terrain de jeu pour étudier l'interaction entre les différents degrés de liberté présents, cinétiques et/ou corrélations entre électrons, dichotomie orbitale ou états de valence multiples des orbitales d. Depuis les simples oxydes binaires tels ZnO, un conducteur transparent jusqu'aux composés quaternaires plus complexes comme $YBa_2Cu_3O_7$, un supraconducteur à haute température, les TMO offrent des fonctionnalités variées.

Cependant, nous nous concentrerons sur les oxydes ternaires plus simples comme $SrTiO_3$ (STO) qui appartient à la famille des composés de perovskites. Leur formule chimique est du type ABO_3 où les cations A et B sont entourés d'une cage octaédrique d'oxygène qui crée un splitting cristallin des orbitales d en deux groupes - une qui a une énergie plus basse, t_{2g}, et l'autre avec une énergie plus haute, e_g. STO, un cristal cubique parfait, a de nombreuses propriétés intéressantes - lorsqu'il est stochiométrique, c'est un isolant paraélectrique quantique; lorsqu'il est dopé, il devient supraconducteur [3] et sous tension, il devient ferroélectrique. Alors qu'un réseau cubique idéal, comme dans le cas de STO, est à même d'accommoder différentes tailles de cations A et B pour une perovskite, on observe en réalité qu'un changement de taille des cations A ou B entraine des distorsions structurelles de la maille cristalline qui réduisent sa symétrie. Le remplacement de Sr par un cation plus petit comme Ca conduit à une structure antiferrodistortif, où les octaèdres d'oxygène successifs subissent des rotations déphasées. Si Sr est remplacé par un atome plus grand, comme Ba, les oxygènes tendent à s'en éloigner et à générer un dipôle, donnant lieu à la ferro-électricité. De ces exemples, il apparait clairement que les octaèdres

d'oxygène jouent un rôle important dans la fonctionnalité d'un matériau.

Au niveau des interfaces ou des surfaces de ces composés, un nouveau comportement est attendu, car diverses symétries sont brisées. Les interfaces peuvent être réalisées avec différents membres de la famille TMO perovskite, en raison de leur capacité à accommoder des déformations structurelles, laissant le champ ouvert aux hétérostructures. Aux interfaces et ainsi qu'aux surfaces, un effet important est la rupture de la symétrie d'inversion, ce qui signifie que le théorème de Bloch n'est plus valable pour une direction particulière. L'effet combiné de la brisure de symétrie d'inversion et de l'interaction spin-orbite (SOC) donne naissance à une nouvelle interaction, nommée Rashba. De manière intéressante, la force du couplage Rashba peut être modulée avec un champ électrique dans le cas d'une hétérostructure de $LaAlO_3$ / $SrTiO_3$ (LAO / STO) où une forte augmentation du couplage de Rashba est constatée en variant la tension de grille [29].

Cependant, cette interaction peut également être présente dans les semi-conducteurs ou les isolants ; ce qui conduisent parfois à des états de surface aux propriétés nouvelles comme dans le cas des isolants topologiques comme Bi_2Se_3 et Bi_2Te_3 [30, 31]. Les deux principales familles présentant des propriétés topologiques sont les matériaux présentant une inversion de bande due à l'effet de SOC et ceux où la symétrie cristalline est importante. Mais les états topologiques ne se limitent pas aux semi-conducteurs ou aux isolants conventionnels et peuvent même être présents dans les TMO. Les interfaces ou les surfaces satisfont de manière inhérente à la condition de rupture de la symétrie d'inversion et, dans cette mesure elles peuvent abriter des états topologiques, dans le cas où une inversion de bande est causée par l'interaction Rashba. En outre, la présence de symétries particulières dans le cas de surfaces orientées $(1\,1\,1)$ de TMO peut mener à des états topologiques en l'absence d'inversion de bande due à l'effet Rashba [35].

Dans cette thèse, une nouvelle classe de matériaux, celle des métaux topologiques, sera étudiée plus en détail avec une discussion approfondie des états topologiques présents à la surface de STO dans l'orientation $(0\,0\,1)$ où un gaz électronique 2D (2DEG) existe déjà et la co-existence de la topologie avec le le gaz métallique sera explorée. Un ensemble de propositions expérimentales seront exposées permettant de mettre en évidence les états topologiques de la couche métallique voire induire de la supraconductivité topologique

aux surfaces. L'orientation (001) n'est pas la seule présentant un intérêt à cet égard. Des états topologiques peuvent également exister dans le cas de l'orientation (111) où des propriétés de transport inattendues ont été mises en lumière. Ainsi, le composé parent de STO, LAO/STO sera exploré dans l'orientation $(1\,1\,1)$ où où des comportements singuliers sont révélés par le biais de mesures d'effet Hall. Normalement, avec l'augmentation de la concentration de porteurs, on pourrait s'attendre à trouver de plus en plus de porteurs. Cependant, contrairement à toute attente on observe un transport multi-bande caractérisé par le fait que des porteurs occupent une nouvelle bande au détriment des porteurs dans la bande originale mesurée à basse tension de grille. On montrera que les corrélations et le confinement quantique à la surface jouent un rôle très important dans l'explication de ce comportement étrange. Le rôle de la topologie sera également discuté dans ce cadre pour voir si le transport multi-bande et la topologie peuvent coexister. Cependant cette question de corrélations n'est pas limitée à LAO/STO et un autre matériau $CaTiO_3$ (CTO) présente également un 2DEG en présence de corrélations. Cependant, dans ce cas, les corrélations peuvent mener à une transition métal-isolant et favoriser le magnétisme à la surface. Cela ouvrira le débat sur la coexistence ou la compétition entre magnétisme et topologie en raison du caractère localisé du magnétisme et du caractère délocalisé des états de bord topologiques. Cette question est également présente dans le cas de STO où la coexistence suggérée du magnétisme et d'une phase métallique de type 2DEG soulève de nombreuses questions. Une autre question qui peut être posée est celle de la topologie à la surface de CTO qui reste pour le moment, sans réponse.

La thèse est organisée comme suit: le premier chapitre traitera l'importante question de la topologie et servira d'un guide pour les types de topologies observés dans les systèmes étudiés. Une fois introduites les différentes classes de matériaux topologiques en 2D et 3D, aussi bien dans le cas où le couplage spin-orbite est l'effet dominant que dans le cas où la symétrie cristalline est à la base de l'état topologique, nous discuterons des états de surface. Ensuite, nous parlerons de la topologie appliquée au TMO et nous nous concentrerons sur la question des états de surface topologiques coexistant avec les états de surface métalliques.

Le second chapitre consistera en une analyse basée sur des modèles de liaison fortes à la surface orientée $(0\,0\,1)$ de $SrTiO_3$. Nous débutons par une introduction générale aux

éléments qui seront nécessaires, comme la modèle aux liaisons fortes, le champ cristallin et le couplage spin-orbite (SOC). Nous poursuivons par une description des propriétés expérimentales de STO en ce qui concerne le volume, puis la surface, notamment l'état métallique mis en évidence à la surface. Ensuite, une modélisation théorique sera proposée en incluant certaines perturbations induites par la surface, telles le potentiel de confinement et le mélange orbital, qui seront discutés en détail afin de mieux comprendre leur impact. Les effets de toutes les perturbations mentionnées précédemment seront alors visibles sur la structure de bande au fur et à mesure de leur ajout, ce qui conduira à des bandes inversées et à des bandes gappées. Cette structure avec les bandes inversées sera ensuite mise en correspondance avec un Hamiltonien Bernevig, Hughes, Zhang (BHZ) [42] et sera résolue pour les états de bord. Enfin, les signatures topologiques des états des bords seront discutées. Un système similaire, LAO/STO, dans l'orientation $(0\,0\,1)$ sera également discuté et une modélisation similaire sera effectuée. Des signatures topologiques similaires apparaîtront alors et une proposition de détection expérimentale de ces états sera faite [79].

Le troisième chapitre continuera avec LAO/STO mais avec une orientation différente, à savoir $(1\,1\,1)$, où un 2DEG existe et des mesures de transport anormales ont été révélées. Lorsque la concentration des porteurs, modulée avec une tension de grille, augmente, une bande commence à se remplir. Si le nombre de porteurs dans le système continue d'augmenter, une autre bande commence à se peupler au détriment de la première ce qui n'est pas attendu. La modélisation théorique de ce système tentera d'abord d'expliquer les différences induites par l'orientation $(1\,1\,1)$ qui conduit à une structure hexagonale si deux couches d'atomes de Ti sont projetées sur le plan $(1\,1\,1)$. Des termes tels que le couplage inter et intra-couche entre les couches de Ti, le bulk SOC et le champ cristallin trigonal seront ajoutés. Le comportement expérimental étrange sera expliqué en inspectant la structure sous-bande vue dans les calculs de Poisson Schrödinger en raison du confinement à la surface et en l'ajoutant au modèle des liaisons fortes. L'introduction des corrélations sous la forme d'une interaction U de Hubbard sera nécessaire pour expliquer l'inversion de bandes. Deux sous-bandes proches de l'énergie de Fermi (E_F), en raison du confinement quantique du gaz à la surface, contribueront à l'inversion de la population de deux bandes de type électrons. Au cours de cette étude, certains croisements de bandes seront mis en

lumière et ce phénomène, combiné à des perturbations caractéristiques du 2DEG, donnera lieu à des états topologiques inattendus.

Le dernier chapitre consiste en une étude ab-initio détaillée d'un autre composé CTO orienté $(0\,0\,1)$, qui se révélera à la fois très différent et pourtant semblable à STO. Les octaèdres d'oxygènes entourant Ti dans ce matériau présentent des inclinaisons et des rotations par rapport aux arêtes de la maille pseudo-cubique de CTO, ce qui impacte les propriétés électroniques de ce composé.

Des études expérimentales ont révélé la présence d'un 2DEG à sa surface $(0\,0\,1)$ en présence de lacunes d'oxygène et mis en lumière des différences avec le gaz présent à la surface orientée STO $(0\,0\,1)$. La forme de la surface de Fermi (FS) indique une hybridation des orbitales impliquées, notamment les cinq orbitales d de Ti. La structure de bande indique également une masse effective différente par rapport aux bandes observées dans STO. Une étude ab-initio a permis de caractériser la structure électronique dans le volume de CTO en présence des configurations tournées des octaèdres déterminée la structure de bande dans le volume nous nous sommes tournés vers l'étude des états électroniques de surface en l'absence, comme en présence de défauts. L'impact des défauts conduira à un état métallique à la surface et à un état localisé dans le gap, tous deux présents dans l'étude ARPES réalisée par Rodel et al [25] et Muff et al [129]. L'état métallique à la surface sera caractérisé et la possibilité de magnétisme à la surface également discuté. La topologie dans ce système, ne restera que comme une perspective et on ne peut qu'espérer inspirer de futures études pour les états topologiques dans CTO.

En conclusion, certaines perspectives sur les trois systèmes, STO, LAO/STO et CTO seront discutées et des travaux futurs sur des systèmes similaires seront exposés dont certains sont expliqués ci-dessous.

Alors que les interfaces et les surfaces se sont avérées être intéressantes par rapport au bulk, il y a encore des mystères à résoudre. Par exemple, les reconstructions de surface qui tentent de compenser la polarité des couches successives du matériau, contribuent à éliminer la dégénérescence des bandes et introduisent également l'élément nécessaire pour l'inversion des bandes. Mais pourrait-il y avoir d'autres effets auxquels on n'a pas pensé jusqu'ici? Par exemple, les défauts ou les lacunes sont considérés comme des acteurs

importants dans la création d'un potentiel de confinement dans le cas de STO mais dans le cas de LAO/STO, ce n'est que l'un des mécanismes possibles en jeu. Pourrait-il y avoir un moyen de distinguer les lacunes en tant que seul mécanisme responsable du gaz? [142, 16]

Dans le cas de LAO/STO, il existe un autre axe de réflexion intéressant: ajouter des couches de sur-couches (capping) pour réduire le nombre de couches de LAO nécessaires à la création de l'état métallique. Des études ab-initio ont montré que l'utilisation de couches de sur-couches métalliques peut rendre possible cette métallisation [143]. Des travaux expérimentaux ont déjà été effectués dans ce sens en utilisant des sur-couches de métaux pour réduire le nombre de couches de LAO nécessaires, mais dans le but de rendre le pompage de spin efficace pour développer les dispositifs spintroniques. Un de mécanismes proposé pour expliquer ce phénomène est l'oxydation de la couche de capping métallique. Le métal présent s'oxyde en aspirant l'oxygène de la couche de LAO, créant ainsi des lacunes dans la couche supérieure de LAO, libérant des électrons qui forment alors le 2DEG. Cette idée intéressante a déjà été utilisée dans le cas de la surface $(0\,0\,1)$ STO de Santander et al pour créer le 2DEG [83]. Au lieu d'utiliser des métaux, nous mettons en oeuvre des calculs DFT relatifs à des hétérostructures LAO/STO où la sur-couche est elle-même un film STO à la surface supérieure de LAO, ce qui se traduit par l'utilisation de STO deux fois, une fois comme substrat et une autre comme couche de recouvrement elle-même. Des expériences préliminaires ont montré qu'un tel scénario est en effet possible [146] où seulement 4 cellules sont nécessaires (n de LAO et m de la sur-couche STO où n + m = 4). Or, les études préliminaires de DFT ne trouvent toutefois pas ce comportement et semblent suggérer un comportement isolant si n=1 et m=3. L'origine de ce comportement, à savoir pourquoi STO est un moyen efficace de réduire le nombre de couches LAO nécessaires, devrait être étudié plus avant par le biais d'études ab initio et il est possible que les surfaces ou les interfaces jouent à nouveau un rôle important. Et là où des surfaces ou des interfaces entrent, la topologie peut encore se manifester, ce qui pourrait être une autre voie à explorer.

En tout, la topologie et les oxydes de métaux de transition sont inextricablement liés et pourraient constituer un terrain de jeu fertile pour sonder de nouvelles propriétés de la matière.

Contents

Chapter 1

Introduction to transition metal oxides

1.1 Introduction to Materials Science

All progress is based upon a universal innate desire of every organism to live beyond its means.

Samuel Butler

Materials science has shown great progress in the recent years leading to a revival in the interest of the scientific community with new and novel phases of matter being discovered. Prior to this renaissance, the field was dominated by conventional materials whose properties were understood and who had wide industrial applications. These materials were classified into three broad classes, that of metals, insulators and semi-conductors. They had mostly been used in electronics, with the entire technological revolution being based on semi-conductors like Silicon (Si) used in devices like chips and transistors. Si however, has its limitations - it cannot be made at the nanoscale becoming unstable and it is also prone to heating when processing large swathes of information. As the demand for fabricating more efficient and smaller devices is ever rising, hence, the search for new materials other than Si, to fabricate these devices, has also picked up speed.

One of the possible candidates to substitute conventional materials are transition metal complexes, displaying exotic phases promoted by strongly correlated electronic phenomena which have been recently unearthed. In *transition metal complexes* the d orbitals are partly filled, which is different from conventional materials which comprise of mostly s or p electrons. This difference has a great effect on the electronic and structural properties of transition metal complexes. In a nutshell, the electronic structure of materials can be analytically described in two limits

- **Nearly free electrons**: This corresponds to the situation when, due to small interatomic distances and large electronic orbital overlaps, bandwidths are sizable. Screening is very effective because of a small Thomas Fermi wavelength. Electron-electron interactions can be safely neglected and electron-ion interactions are only felt close to the periodic distribution of positive ions. Hence electronic wavefunctions are free electron-like; the lattice periodicity only plays a role close to the edges of the Brillouin zone (Bloch states). This

describes solids with s and p -type of carriers. We note however that, for semiconductors, the filling is usually low and thus, the kinetic energy is comparable or even smaller than the Coulomb energy and the above description needs to be amended. This limit of *no interactions* seemed pretty well understood in simple terms. However the condensed matter community was in for a big surprise some 15 odd years ago, when it was predicted that the particle eigenfunctions of select compounds would exhibit a singular behaviour, manifested in a singular phase, signalling a topological regime. These materials could support a dissipationless conducting state at the surface, while their bulk remained insulating. This current was shown to be stable to certain perturbations of the sample and as it was not superconducting, it did not need low temperature cooling. Such materials, now experimentally realised, are now in a class of their own, that of topological materials, and would be of great industrial interest if developed further as they could replace semiconductors and metals. The topological properties of such materials will be discussed later.

- **Nearly localised electrons** : This corresponds generically to the situation when the spatial extension of the electronic wavefunctions of the constitutive atoms in the solid is limited to a narrow range around the ionic core. We can then construct molecular orbitals (known as the Linear Combination of Atomic orbitals or LCAO approach) and discuss the interplay of kinetics and correlations in that framework. It is to be noted that we can use this method to treat s and p bands as well, even though the nearly free electron approach is perfectly suitable, but it becomes warranted when we are considering d or f electrons. We shall focus only on the d electrons. The covalent bonding in the d electrons produces narrow bands and might enhance the effects of correlations like the Coulomb interactions. The latter can be approximated by the Hubbard term, U, which prohibits carriers to occupy the same site by adding a repulsion term to the energy of the carriers. Owing to multiple d orbitals being present, the situation is more complex as one identifies intra-orbital contributions, inter-orbital contributions and Hund exchange terms. For transition metal compounds, the LCAO description accounts for the formal valence of the d (transition element) and p (oxygen components) thus leading to iono-covalent bonding and charge transfer mechanism. The interplay of U and kinetic terms having similar energy scales causes a broad range of phase changes, such as metal to insulator transition (MIT) or magnetic

instabilities (due to the double exchange or the superexchange mechanisms).

Of the transition metal compounds which are of interest, oxides provide an excellent playground to probe the interplay between the different degrees of freedom present. The kinetics, itself, of the electron is different, as now the oxygen and the metal atom are both involved. This changes the bandwidth of the conduction band and has an impact on the ordering of the d orbitals. Owing to the capability of transition metals to have multiple valence states, many electronic configurations and bonding modalities now become possible. The energies of these multi-valence states are compatible to the energies of the different oxygen charge states and a charge transfer can also take place. From the above discussion, we also know that correlations also play an important role in these d electron systems and there will, thus, be an interplay between kinetics and correlations in these oxides. The presence of multiple orbitals in d electron systems also opens up the way for orbital dichotomy which is the path to be taken for the coexistence of contrasting properties like magnetism and superconductivity.

1.2 Transition metal oxides and their functionalities

Transition metal oxides (TMO), as their name suggests, generally comprise of oxygen involved in bonds (covalent and/or ionic) with transition metals and other atoms which play mainly a structural role. Earlier, the band theory applied to the s, p, d orbitals was discussed which assumed that the electrons were mostly delocalised. Instead, we use the LCAO model where electrons are mostly localised on the lattice and are supposed to *hop* from one site to another in an iono-covalent periodic background or the lattice, which gives rise to kinetic terms in the energy of the electrons. The oxygens provides pathways for electron hopping as they bridge one transition metal ion to another. This hopping from a transition metal ion to oxygen changes the bandwidth and the effective masses of the d electrons and leads to the lowest energy conduction band being comprised mostly of the transition metals and the highest energy that of the valence bands of oxygen. As the five d orbitals come closer to each other in energy, there is a greater probability of correlations, like the Coulomb interactions (U) or the exchange interaction, coming into play. Magnetism is one

of the properties, which most of the partially filled d electrons system share, arising as a result of correlations. Correlations in the form of exchange interactions, are symmetry-constrained Coulomb interactions that have the effect of coupling electronic spins and they can be inter or intra-site in nature. The J_H or Hund's rule exchange, couples electrons in a partially filled shell on an ion so as to maximize the total spin (Hund's first rule). U couples the spin up and down occupations at every site (in order to abide by Pauli's principle), and is responsible for the magnetic order which leads to ferro or anti-ferro magnetism in the system. Due to the multiplicity of the d orbitals, these two terms can be both on the same site, acting between different orbitals.

However, this is too simplified a picture and works for free atoms or ions; once the oxide is formed, the crystal field or the ligand field effect, due to the oxygens, influences the atoms drastically. There is a competition between Hund's rule and the crystal field splitting. In addition, charge or orbital ordering might take place in transition metal complexes [1], or even double exchange or superexchange which involves the oxygens and the transition metal ions, complicating the picture of magnetism in oxides even further. Superconductivity also arises as a result of correlations (attractive interactions between electrons to form Cooper pairs) and transition metal oxides also exhibit normal and high temperature superconductivity. It is interesting to note that as the energy scales are comparable for the correlations and the kinetics, they compete or couple with each other, leading to interesting phenomena like giant magnetoresistance (GMR) and unconventional superconductivity. But this is just the tip of the iceberg. Since there is a presence of multiple valence states for the transition metals, it leads to different structures being realised between the same transition metal and oxygen. Structural and electronic transitions also have comparable energy scales and thus, all the degrees of freedom are in competition with each other. Apart from the interplay of correlations, kinetics and structural transitions, there is another factor which controls the functionalities of these oxides - distortions of the lattice by doping.

Ranging from simple binary oxides like ZnO, a transparent conductor or the more complex quaternary compounds like $YBa_2Cu_3O_7$, a high temperature superconductor, TMO provide varied functionalities. In the case of binary compounds like ZnO or VO, the structure resembles that of semi-conductors, which can be halite (NaCl like) or wurtzite (ZnS

like). Nevertheless, they can have interesting properties of being transparant conductors, piezoelectrics or pyroelectrics or even have a competition between structural and electronic transitions, the winner of which is still open to debate [2]. The more complex oxides, like the cuprates, are the family known to exhibit high temperature superconductivity. However, we shall focus on the simpler ternary oxides like $SrTiO_3$ (STO) which belong to the family of perovskite compounds. These have an ABO_3 type of stoichiometry with the A and B cations being surrounded by an oxygen octahedron cage which creates crystal field splitting of the d orbitals into two groups- a lower energy t_{2g} and a higher energy e_g. We had already seen the impact of this term when discussing magnetism but we shall see that it will also be important for the electronic properties.

STO, a perfect cubic crystal, has a host of interesting bulk properties - when stochiometric, it is a quantum para-electric insulator, when doped, it becomes a superconductor [3] and under strain, it transforms to a ferroelectric. We also know that the ideal cubic lattice, such as STO, can accomodate different sizes of the A and B cation for the perovskites. Despite this fact, when the size of A and B cations is changed, the lattice undergoes different types of structural distortions which lower its symmetry. Replacing Sr with a smaller cation like Ca, leads to an antiferrodistortive ordering, where successive oxygen octahedra undergo out of phase rotations. If Sr is replaced by a larger atom, like Ba, the oxygens tend to move away from it and generate a dipole, giving rise to ferro-electricity. From these examples, it is clear that the oxygen octahedra play an important role in the functionality of a material. The rotations and tilting of octahedra lead to distortions in the B-O-B bond angle which have consequences for the electronic and magnetic properties of the compounds. The rare-earth nickelates $RNiO_3$ undergo a metal to insulator transition (MIT) when the Ni-O-Ni angles are increased.[4] [5]. The magnetic super-exchange interaction will depend on the bond angle in manganites [6].

Thus, there are various ways to control the functionalities of these TMO-

(a) the interplay between correlations and kinetics,

(b) the interplay of structural and electronic transitions and

(c) controlling the distortions in the lattice leading to changes in the local and global environment.

But so far we have only discussed bulk effects and it is not only the bulk of these materials which can be probed for new and exotic phases of matter. At the interfaces or the surfaces of these compounds, new behaviour is expected to emerge, as various symmetries are broken. Interfaces can be realised with different members of the perovskite TMO family, owing to their structural compatibility, leaving the field open to heterostructures. However, an interface needs almost atomic like precision which is difficult to achieve but owing to recent advancements in technologies like pulsed laser deposition and molecular beam epitaxy, we now have access to atomic-level control of complex oxide heterostructures. Entirely new properties manifest once we start creating interfaces between two TMO as was seen in the discovery of a metallic interface of band insulators $LaAlO_3$ and $SrTiO_3$ (LAO/STO) [7]. Surfaces also manifest unique properties as in the case of $SrTiO_3$ which gave rise to metallic sub-bands and even spin windings at its surface. [8][9]

1.3 Probing Surfaces and Interfaces of transition metal oxides

1.3.1 Interfacial effects and properties

Interfaces between two materials are interesting areas to probe for new functionalities. One would naively expect that the host materials forming the interface will maintain their properties at the interface, albeit a slight mixing between them. However, the discovery of the metallic interfaces between TMO greatly changes this simple minded picture. Thus, the question arises, what is the difference between the bulk and an interface and what effects can we expect to occur at the interface?

Firstly, if the two materials forming the interface have different lattice parameters, a lattice mismatch might induce a tensile or compressive strain in one or both of the systems, leading to changes in the bond length and in the distortion of the bond angle. This might strain or distort the lattice, lowering the symmetry and driving a structural transition, which can have a direct effect on the electronic properties.These structural phases are very close in energy. Added to this fact is a large coupling between strain and polarisation in perovskites

and these two properties have led to the creation of a new domain of strain engineering where it can be used to stabilize alternative ground states and to control the functionalities.

Secondly, if one of the two materials has a polar termination while the other does not, there can be a charge discontinuity, leading to a charge transfer. This is already observed in semi-conductors, when the two materials have a different chemical potential and it has been used in devices like p-n junctions and Schottky diodes. This mismatch in polarity has another effect - the interface will try to reduce the discontinuity in polarity and to accommodate it by distorting the surface of the two materials in question. This will lead to an intermixing of the two materials at the interface which might have an impact of the charge which can spill over from the polar material to the other non polar material.

Thirdly, there is the issue of length scales. If unscreened or poorly screened Coulomb interactions or magnetic or strain fields were to be considered, they would have an impact even away from their sources. Even if the screening is not effective, their impact would be felt for a couple of layers and after that, the material would regain its bulk-like behaviour. This leads to gradients in polarisation or magnetization or strain, earlier forbidden by symmetry arguments in the bulk, which contribute to the free energy, leading to new phenomena like flexoelectricity in non-polar dielectrics [10][11]. The gradients in charge can also lead to a non-uniform doping profile at the interface, which in layered compounds can produce different electronic concentrations on the atomic planes. This has been used in high temperature superconductivity when making an interface between metallic $La_{1.55}Sr_{0.45}CuO_4$ and insulating La_2CuO_4 as Bozovic et al showed that a single layer of CuO could contain all the superconductivity [12].

This approach of a gradient of polarisation or an electric field penetrating the system up to a depth, will be the basis of one of the theories used to explain the metallic interface in the LAO/STO system, which is popularly called the polar catastrophe theory [13, 14]. In this system, both LAO and STO are wide band gap insulators (E_{gap} = 5.6 eV for bulk LAO and E_{gap} = 3.2 eV for bulk STO) and yet deposition of a film of LAO, greater than four unit cells on top of the STO substrate, yields a metallic interface. It is to be noted that the metallic interface is only produced if the STO is TiO_2 terminated and the LAO is LaO terminated near the interface. [7, 15]. LAO is known to have alternating charged

planes and the gradient of electric field is such that the electrons are transferred from the topmost layer of LAO to the interface to compensate for this charge discontinuity. The other theory used to explain the origin of the metallic interface comes from defects [16] at the top surface of LAO, which contribute to extra electrons used for forming the 2 D electronic gas (2DEG). The value of the carrier density, observed either in Angle-Resolved Photo-emission Spectroscopy (ARPES) or transport, for the gas corresponds more to this scenario rather than that predicted by the polar catastrophe. The oxygen vacancy scenario finds even more credibility as a 2DEG was found at the surface of STO without the polar LAO to create the polar catastrophe. For STO, it is found that the defects arising because of the oxygen vacancies have a double role - they provide the electrons for the gas and keep the gas confined to the surface. Alternatively, a phenomenon can have an origin far way from the interface/surface and yet be prone to proximity effects. This proximity effect is studied in magnetic-superconducting structures where a theoretical prediction of strange superconducting states with spin-triplet Cooper pairs has been done. [17].

There is another important factor that we have not considered so far which is that of dimensionality. A thin film can be considered as three dimensional in diffusive transport and characterised with respect to its elastic scattering length. However, if temperatures are lowered, the same film might prove to be superconducting in just two dimensions. Hence, even for the same material, dimensionality can be tuned just as a function of temperature. [18] Magnetism is also an important element at this interface of LAO/STO as there is a tendency toward phase segregation into ferromagnetic and superconducting regions [19]. The first evidence for magnetic order was indirect, from magnetoresistance measurements [20], but recent experiments have shown evidence of magnetization corresponding to possible magnetic moments of order 1 μ_B per unit cell, persisting up to room temperature, and superconductivity below 60 mK [21].

However, interfaces are not the only interesting places to look for new phases of matter- surfaces which are nothing but an interface with vacuum on one side and a material at the other - can also be equally intriguing.

1.3.2 Surfaces as simplified interfaces

Surfaces are extremely interesting even though most of the above mentioned effects for interfaces are valid here as well. Normally, a surface is created by cleaving the system and removing certain bonds which were earlier present in the bulk, thus, creating dangling bonds. This leaves the surface open to distortions as the atoms at the surface have an additional degree of freedom and can move more freely than earlier. Another effect to consider is the ionic nature of the compounds due to which the surface might become polar for a specific termination which makes it unstable. The polarity and the dangling bonds are then accommodated by the distortion of the bond angle (or rumpling) which might also entail the rotation and tilting of the oxygen octahedra, both of which have an impact on the electronic properties. These rotations have been observed in the (001) orientation for the Ruddlesden-Popper layered superconductor Sr_2RuO_4 and are believed to couple to spin fluctuations, stabilizing a local ferromagnetic state [22].

But inducing oxygen rotations is not the only role of the surface. In certain ferroelectric materials, the surface also entails a change in the electrostatic boundary conditions. If the continuity of the displacement vector across the surface is enforced and the lack of polarisation in the vacuum considered, then there will exist strong depolarising fields within the material. This depolarising field will suppress the out of plane polarisation and can also create domains of alternating polarisation which were not earlier present in the bulk. [23, 24]

The surface is also extremely sensitive to the environment it is kept in and often for measurements, one needs to protect them. For $SrTiO_3$ or $CaTiO_3$, the sample needs to be protected by a thin film of Al to carry out transport measurements [25]. For characterising the surface, often ARPES is performed which affects the surface and creates defects. The important role that defects play will be interesting to investigate as will be seen in Chapter 1 where their presence is needed in order to have certain type of surface states. Thus, defects can be used to our advantage and can lead to interesting effects.

1.4 Conditions for topology in transition metal oxides

An important effect is the breaking of inversion symmetry at the surface or even at the interface, which will mean that the Bloch theorem is no longer valid for one particular direction. If spin-orbit coupling is added to the inversion symmetry breaking, a new interaction in the form of Rashba interaction arises. This interaction has already been used to tune the spin precession in a 2DEG confined in conventional semiconductor heterostructures [26, 27, 28]. Interestingly enough, the strength of the Rashba coupling can be tuned with an electric field in the case of LAO/STO where a steep rise in the Rashba coupling is noticed as the transition from an insulating to superconducting takes place [29]. However, this interaction can also be present in semi-conductors or insulators which sometimes lead to surface states with novel properties as in the case of topological insulators like Bi_2Se_3 and Bi_2Te_3 [30, 31]. The two main families exhibiting topological properties are materials showing band inversion driven by SOC and those where crystalline symmetry is important. The members of the first family include the famous quantum wells of HgTe/CdTe, tetradymite semi-conductors among others. The second family consists of the distorted bulk of $(1\,1\,1)$ HgTe, a semi-metal where a slight perturbation is enough to open a gap between the bands. [32]. Ternary Heusler compounds also exhibit similar band structure and around fifty have been identified [33, 34].

But topological states are not just limited to conventional semi-conductors or insulators and can even be present in TMO. Howver, we have to look at the right place for topological states in the case of TMO. In the bulk, the correlations become too important and the gaps so big that it will be difficult to look for topological signatures there. Luckily, interfaces or surfaces inherently satisfy the condition of breaking of inversion symmetry and if they also possess the Rashba interaction, with a band inversion, they could become a playground for topological states. Not only this, but if symmetry arguments are to be taken into account, then the $(1\,1\,1)$ surfaces of certain TMO can show topological states [35] where band inversion is not even needed.

This subject of topology warrants our full attention and it shall be given its due respect in the first chapter which will deal with a brief historical perspective of topology

and will then introduce different categories of topological materials, be it spin-orbit driven topological insulators or topological crystalline insulators. Another class of materials apart from these two called topological metals will have examples from oxides which can have topological states and open up the domain of topological oxide electronics.

The class of topological metals will be further discussed with a detailed discussion on the topological states present at the surface of STO in the $(0\,0\,1)$ orientation where a 2DEG already exists and the co-existence of topology with the metallic gas will be explored. For the possible experimental detection, certain gedanken (thought experiments) will be proposed, opening the discussion for favouring topological states over the metallic gas and even inducing topological superconductivity at the surface.

The only interesting orientation will not be the $(0\,0\,1)$ as was already explained above, the $(1\,1\,1)$ orientation can also possibly host topology. In that respect, the parent compound of STO, LAO/STO will be explored in the $(1\,1\,1)$ orientation where strange transport properties are measured in Hall measurements. Normally, with gating or increase of the carrier concentration, one would expect to find more and more carriers. However, much to everyone's chagrin, multi-band transport is seen and the carriers being populated in a new band at the expense of carriers in the original band measured at low gate voltages. It will be shown that correlations and the quantum confinement at the surface will play a very important role in explaining this strange behaviour. The role of topology will also be discussed in this framework to see if both the multi-band transport and topology can co-exist. However this question of correlations is not limited to LAO/STO and another material $CaTiO_3$ (CTO) will also display a 2DEG in the presence of correlations. However in this case, the correlations will drive a metal-insulator transition and show signatures of magnetism at the surface. This will open up the debate for the co-existence or competition between magnetism and topology owing to the localised preference of magnetism and the delocalised preference of topological edge states. This question also is present for STO where reports of magnetism have surfaced and the reason for the existence of the 2DEG might not be so clear. Another question which can be asked is that of topology at the surface of CTO which remains unanswered.

1.5 Organisation of the thesis

The thesis has been organised as follows- the first chapter will deal the important issue of topology and will serve as a guide for the kinds of topologies seen in the systems under study. Once the different classes of topological materials, be it spin-orbit protected Topological insulators, Topological Crystalline insulators, have been introduced in 2D and 3D, the surface states, if any, will be discussed. Next, we will talk about topology as applied to TMO and will focus on the issue of topological surface states co-existing with metallic surface states for the case of TMO.

The second chapter will consist of a detailed tight binding analysis of the $(0\,0\,1)$ oriented surface of $SrTiO_3$, beginning with a general introduction to the elements which will be needed, like tight binding formulation, crystal field and bulk spin-orbit coupling. It will then continue to explain the bulk and surface properties of $SrTiO_3$ experimentally observed, in particular, the metallic state found at the surface. Next, a theoretical modelling will be proposed inclusive of certain surface induced perturbations like the confinement potential and the orbital mixing. The effects of all the perturbation mentioned before will then be seen on the band structure, leading to band inversion and finally, the topological signatures of phase winding and edge states will be discussed. A similar system, LAO/STO, in the $(0\,0\,1)$ orientation will also be discussed and a similar modelling will be done. Similar topological signatures will then emerge and a proposal of the experimental detection of these states will be made.

The third chapter will continue with LAO/STO but at a different orientation, the $(1\,1\,1)$, where a 2DEG exists and anomalous transport measurements have been revealed. As the carrier concentration is tuned with a gate voltage, one band gets populated. On increasing the carriers in the system, another band starts getting populated at the expense of the first one. Theoretical modelling of this system will explain this odd behaviour by inspecting the sub-band structure due to the confinement at the surface and by introducing correlations in the form of a Hubbard U. During this investigation, certain band crossings will be unearthed which when mixed with certain perturbation terms will give rise to unexpected topological states.

The final chapter will consist of a detailed ab-initio study of another compound CTO at its $(0\,0\,1)$ orientation, which will prove to be very different and yet similar to STO. It is known that bulk CTO has certain tiltings and rotation of the octahedra which might have an impact on its electronic properties. Experimental studies have revealed a 2DEG at its $(0\,0\,1)$ surface and comparisons to the gas present at the STO $(0\,0\,1)$ oriented surface will be made. An ab-initio study will then be carried out in the bulk to asses the impact of the structural distortions on the electronic structure. Once the bulk is characterised, a surface slab will be investigated with the possibility of having some defects and its electronic properties investigated. The metallic state at the surface will be characterised and the possibility of magnetism at the surface also delved into. Topology in this system, will only rest as a perspective and one can only hope to inspire future studies for topological states in CTO.

To conclude with, certain perspectives on all three systems, STO, LAO/STO and CTO will be discussed and future work on similar systems laid down.

Chapter 2

Topology in Materials Science and oxides

2.1 Introduction to Topology

God runs electromagnetics by wave theory on Monday, Wednesday, and Friday, and the Devil runs them by quantum theory on Tuesday, Thursday, and Saturday.

Sir William Bragg

Before we delve into the possible topological properties of TMO, let us take a step back and look into the introduction of topology to Materials Science and why it opened up new avenues of research.

Topology in itself was not a new concept in Physics, the language, methods, and theorems of algebraic topology, particularly homotopy theory, had been used in the study of relativistic field theories for over fifty years. Defects and topology were known to play an important role in soft matter physics like screw or edge dislocations in liquid crystals [36]. It was shown that the singularities arising in real space in the order parameter around these defects could have signatures or manifestations in the space surrounding it and thus, give rise to different phases in these crystals. But in Materials Science, topology was not known to play any special role. Up until the 20th century, people believed that all the states of matter had been discovered and classified. In condensed matter physics, the classification of any new state of matter was defined by the Landau theory of spontaneous symmetry breaking. A crystalline solid broke translational symmetry, a magnet broke rotational symmetry and a superconductor broke a more subtle gauge symmetry leading to Josephson effects and flux quantization. This pattern of symmetry breaking was characterized in terms of order parameters having a finite value in the ordered state.

A breakthrough occurred when Berezinskii-Kosterlitz-Thouless proposed a new description of phase transitions in two-dimensional systems involving defects, notably vortices, leading to the so called 2D XY universality class. These vortices, which were known in the context of superconductors and superfluids, were necessary to describe the phase transition and thermodynamic states of the 2D XY model. At low temperatures (below the T_{BKT}), there was an anti-vortex vortex binding but as the temperature was raised, there

was a proliferation of anti-vortices and vortices that became unbound. This was a new kind of phase transition which involved certain singularities in real space. Moreover, this phase transition occurred without the spontaneous symmetry breaking familiar from Landau theory.

Another breakthrough occured in 1980, when a new state- the Quantum Hall (QH) state- was discovered where the bulk of the sample remained insulating while the edge carried a dissipationless current. A two-dimensional electron gas produced at a semiconductor hetero-junction and subjected to a strong magnetic field, had a vanishing longitudinal conductivity and resistivity while quantum plateaus appeared in the Hall conductance at integer values $\sigma_{xy} = \mu e^2/h$ for $\mu = 1, 2...n$ [37]. This quantization was universal and independent of all microscopic details such as the type of the material, the purity of the sample, the precise value of the magnetic field, and so forth. Clearly the system was showing signs of undergoing some sort of sequence of phase transitions into a highly idealized dissipationless states just as in a superconductor. The fractional QH effect was discovered soon after where μ now took fractional values. A variational wave function proposed by Laughlin, consisting of a phase factor α_{ij} was used to explain this incompressible state giving rise to the conductance plateaus [38]. But the experimental observation of the above transitions was quite challenging as it required very large carrier mobilities and sizeable magnetic fields. A new development in the field of condensed matter topology took place when Haldane predicted that in a graphene-like system, with alternating magnetic flux to break the time reversal (TR) symmetry, dissipationless edge states would exist [39]. This idea was then refined by Kane and Mele to include other more realistic models [40, 41]. The Spin QH (QSH) effect was discovered in quantum wells and Bernevig, Hughes and Zhang proposed a theoretical model leading to the prediction of 1D edge states [42]. Similar to the QH state, a dissipationless current at the edges of semi-conductors was found, except this time it was a spin-polarised current instead of being a charge current. A Z_2 invariant, which arose from the singularities of the Berry curvature of the wave function in reciprocal space, was also predicted.

With this it became clear that we needed a new class of materials for the classification of these aforementioned materials, all of which are now grouped under the name **topological**

insulators (TI). The topological states present at the surface, were protected from impurity scattering by symmetries, notably the TR symmetry combined with a spin-orbit coupling or with other crystalline symmetries . And surprisingly enough, the same singularities of phase, this time in reciprocal space, would give rise to topological invariants just as in the case of liquid crystals, leading to a better classification of materials.

2.2 Topology in Condensed Matter

The word ”topological” arises in crystalline solids because the wave states which describe their electronic states span a Hilbert space with a non trivial topology. In these solids, the wave vector k is a good quantum number and then the wave function can be seen as a mapping from the k-space to a manifold in the Hilbert space (or in its projection), and hence the topology becomes relevant to electronic states in solids. One very important consequence of topology is that if a topological material (which shows gapped states at the Fermi energy (E_F)) is sandwiched with another (vacuum for example) which is non topological, there will be an abrupt change at the surface, signalled by the presence of allowed energy dispersions within the gap and the appearance of dissipationless edge states. This is what happens if a topological insulator encounters a surface or is terminated. This necessity of gapless interface states to go from one gapped state to another, is called bulk boundary correspondence in topological phases. Depending on the way the Hilbert space topology becomes nontrivial, there can be various different kinds of TI. They can be divided into two major classes-that which have spin-orbit coupling and TR protecting the topological states and another which a priori, do not need spin-orbit coupling and are instead protected by some other crystalline symmetry. The latter are called Topological crystalline insulators (TCI). We shall first begin by characterising 3D TI and their surface states before doing the same for their 2D counterparts.

2.3 Topological insulators in three dimensions

The nature of the topological surface states depends on the Z_2 invariant used to characterise them. The Z_2 invariant can be simply expressed as the number of times a generic Fermi surface inside the bulk gap intersects the surface bands. If the number is even, it gives rise to topologically trivial states and if the number is odd, it gives rise to topological surface states. The Z_2 invariant is normally calculated at the Time Reversal Invariant Momenta (TRIM). It can also be defined as the product of the parities of the eigenvalues of the band states at TRIM or the number of Dirac cones (lines in 2D) cross the fermi energy [40].

In 3D, there are four Z_2 invariants which characterize the topology [43, 44]. Three of the four invariants are based on the translational symmetry of the lattice and are thus, not robust in the presence of disorder, leading to "weak topological insulators." They are based on a product of the parities of the TRIM which lie in the same plane and depend on the choice of the reciprocal lattice vectors used to calculate them. If the product is then calculated, one will get always an even parity because either all will be positive or two will be negative and two positive. The fourth invariant, however, is a product of all 8 TRIM and is independent of the choice of reciprocal lattice vectors. It can have one TRIM which will give rise to a negative sign and thus, overall, it will be of odd parity. It is thus, robust and is called the *strong topological insulator* (STI). We shall mainly focus on the latter as can be seen in Figure 2.1 and for details on the former, the reader is advised to refer to [44].

2.3.1 Spin-orbit protected Topological Insulators

Among the 3D TI with band inversion and negative parity at an odd number of TRIM, one of the first TI, to be studied and then later confirmed, was the $Bi_{1-x}Sb_x$ alloy. The band inversion in this case, occurs at 3 TRIM, known as the L points. The surface band structure is rather complex, with an odd number of Dirac cones and additional surface states. There are also other 3D materials which consist of a single Dirac cone which are the binary tetradymite compounds Bi_2Se_3 (as seen in Figure 2.1) and Bi_2Te_3 where the atomic

p orbitals of Bi or Sb are important. A strong spin-orbit coupling reverses the order of two bands, of dominant p_z character and of opposite parities, at Γ. Other materials like Bi_2Te_2Se and alloyed tetradymite compounds $Bi_{2-x}Sb_xTe_{3-y}Se_y$ also show clear signatures of surface state transport [45, 31]. In thin films of 3D TI, similar surface dominated transport is seen in strained HgTe and in $Bi_{2-x}Sb_xTe_3$. This domain is extremely challenging experimentally due to the complicated fabrication of these materials. Added to this, additional conductivity in the bulk (because of sample doping) complicates things further. In the 3D STI case, any perturbation or disorder which preserves TR symmetry cannot introduce a gap for the surface states. However, magnetic impurities can destroy or induce gaps in the surface states and their interplay with magnetism will be discussed to some extent in Chapter 3. It is to be noted that prior to BHZ, the bulk doping with Hg of CdTe had already shown the presence of band inversion and it can be called the forefather of the BHZ model [46]. Apart from spin-orbit driven TI, there is another category of TI called crystalline TI which will be discussed next.

2.3.2 Topological Crystalline Insulators

This is a broader category of TI which relies on the presence of certain symmetries apart from TR and can be adiabatically transformed to a trivial phase if this underlying symmetry is removed. They are also defined by topological invariants encoded in the wave-functions of the particles in k-space. These crystal symmetries can be a reflection or a rotation for example C_{4v} point group which requires four fold rotation and a reflection. In fact a reflection or a mirror plane M is equal to a product of spatial inversion P and a two-fold rotation C_2. In spin-orbit coupled systems which we shall be dealing with in Chapter 3, C_2 is a combined rotation of the spatial coordinates and the spin of an electron. It is interesting to note here that spin-orbit coupling is, a priori, not needed for topology; it is the underlying symmetries or the orbital degrees of freedom which play a similar role. However, the lack of SOC also has implications for the stability of the edge states as the crystalline symmetries are not all present at the surface. One needs to make careful considerations while projecting the bulk symmetries on the surface to see which of them are maintained at a particular surface. We will introduce the mirror Chern number in the 2D case because it is simpler

to analyse. The concept of a mirror Chern number can be generalised to the 3D case. The 3D crystals can have one or more mirror planes. In momentum space, each of these will be indexed by its own mirror Chern number and thus, there will be a set of mirror Chern numbers which classify the 3D TI. Compared with TIs, TCI surface states have a much wider range of tunable electronic properties under various perturbations, such as structural distortion, magnetic dopant, mechanical strain, thickness engineering, and disorder [47, 48, 49].

2.3.3 2D Surface states for 3D Topological Insulators

The presence of symmetries has implications on the surface states and makes them either trivial or topological. Fore example, if the mirror or the M symmetry is present, then it has implications for the eigenenergies and eigenstates of the system. In fact, it leads to a mirror Chern number which can have a non zero value even if the total Chern number is zero. Unlike TR, these symmetries can be broken at the surfaces of samples even if certain others which preserve these symmetries will still have these gapless surface states. Let us illustrate the TCI class by taking the example of SnTe - the existence of a non zero mirror Chern number guarantees the existence of topological surface states on the $(0\,0\,1)$, $(1\,1\,0)$ and the $(1\,1\,1)$ surfaces as seen in Figure 2.1. The first two belong to the first type of TCI surface states where a pair of L points are projected onto the same TRIM on the surface. The massless Dirac fermions at these points hybridize with each other and give rise to unprecedented surface states. The second type of surface states in the $(1\,1\,1)$ orientated surface has one of the four L points projected onto the $\bar{\Gamma}$ point of the surface Brillouin Zone (BZ) and the other three L points to the $\bar{M}$. This surface has four branches of massless Dirac fermions with one branch located at $\bar{\Gamma}$ and the other three at $\bar{M}$ and they are so connected so as to give a topological state. ARPES measurements show this peculiar kind of surface state consisting of 4 Dirac cones. [50, 48]. The edge band structures discussed above are directly related to the mirror Chern number of TCIs. The $(0\,0\,1)$ surface exhibits surface band crossings in the ΓX direction between bands of opposite mirror eigenvalues, and the $(1\,1\,1)$ surface shows similar crossings in the ΓM direction. These crossings protected by mirror symmetry guarantee the gapless nature of

TCI surface states, replacing the role of Kramers degeneracy in spin-orbit coupling driven Z_2 TIs. For a detailed discussion, the reader is referred to read [49, 51].

Kane and Mele gave a method based on the parity eigenvalues of the band states at TRIM which can be used to calculate the Z_2 invariant [44]. These TRIM can be seen in Figure 2.1. The surface states are then calculated along a path connecting the surface time-reversal invariant momenta. On this basis, the $BiSb_{1-x}$ alloy has been predicted to be a topological insulator for a small range of x and recently surface states with odd number of crossings at the Fermi energy have been seen in ARPES [52]. Other kinds of symmetries can give rise to a variety of topological phases like topological superconductors [43, 44, 53]

2.4 Topological Insulators in two dimensions

In 2D, there are far fewer topological invariants and in fact all TIs are classified according to only one Z_2 invariant which is even (odd) for trivial (topological) states. In 2D again, we make the distinction between spin-orbit driven TI and TCI.

2.4.1 Spin-orbit coupling driven Topological Insulators in 2D

A major category of the TIs which have been uncovered consist of semi-conductors with band inversion driven by spin-orbit coupling [55]. One standard example is the quantum wells of CdTe/HgTe, uncovered by BHZ, where the band inversion takes place at the Γ point [42]. This is in part related to the natural band inversion in HgTe due to the large spin-orbit coupling coming from the heavy atom, Hg, and in part to the quantum well structure which brings the different sub-bands into play. The barrier material constituted of CdTe has a normal band structure with the conduction band composed of the s-type Γ_6 and the valence band composed of the p-type Γ_8. The well material HgTe, which has an inverted band structure, has the s-type Γ_6 forming the valence band and the p-type Γ_8 forming the conduction band. It is important to note that the valence and the conduction band near Γ, which intersect to form the band inverted structure have different (opposite) parities. As the thickness of the material in the well is changed, a transition from a gapped

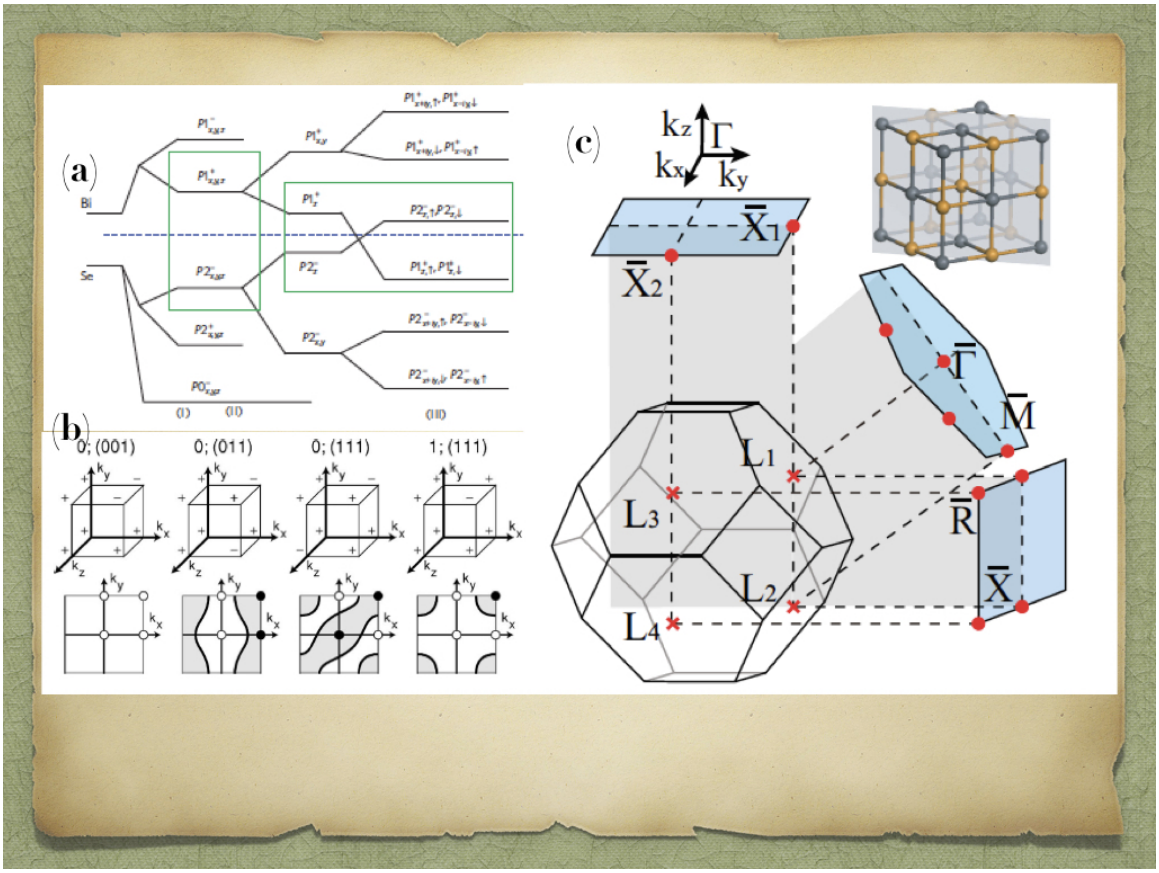

Figure 2.1: (a) The band inversion as seen in Bi_2Se_3 shown by means of bonding and anti-bonding orbitals derived from the atomic orbitals of Bi and Se . Adapted from [54] (b) The trivial (0) and topological (1) phases of a 3D TI as derived by Kane and Mele using the parities of the wavefunction at TRIM [44]. (c) Surface topological states arise at TRIM given by the projections on the $(0\,0\,1)$, $(1\,1\,1)$ and $(1\,1\,0)$ surfaces respectively of the bulk symmetries. Adapted from [51].

to an inverted gapped structure is seen and this transition is corresponds to the closing of a gap. The band inversion can be tuned by varying the strength of the spin-orbit coupling in the system. Another example of 2D TI is in a InAs/GaSb heterojunction where the band inversion is still at Γ but the band inversion is created by the anti-crossing of the inverted electron sub-band in InAs and the hole sub-band in GaSb. [56]

2.4.2 1D surface states for 2D spin-orbit driven topological insulators

The nature of the topological surface states depends on the Z_2 invariant used to characterise them. The Z_2 invariant can be simply expressed as the number of times a generic

Fermi surface inside the bulk gap intersects the 1D edge states. Similar to the 3D case, if the number is even, it gives rise to topologically trivial states and if the number is odd, it gives rise to topological surface states. The Z_2 invariant is normally calculated at TRIM (Γ, X, Y, M of a square BZ in 2D). The inverted band gaps which occur in these TI must appear at an odd number of TRIM for a nontrivial Z_2 index to be found. In this case, the Z_2 invariant is calculated near $k = 0$ or the Γ point. The edge states so formed in TIs are protected against any disorder by TR (Kramers' degeneracy) and by the spin-orbit coupling. The 1D helical edge states, present in both materials, live at the same edge and are polarised in spin [57, 58]. Experimentally, both materials are difficult to grow for the edge states to be observed easily but gating can tune the electronic carrier concentration or the Fermi level allowing those to be seen. Similar to the 3D case, any impurity at the surface which breaks TR will perturb the states.

Another class of compounds, which show topological states and which do not require spin-orbit protection, are the crystalline symmetry protected TI.

2.4.3 Topological Crystalline Insulators in 2D

In 2D, the concept of a mirror Chern number is easier to understand. In k-space, the M symmetry operates on the wave function to give an odd/even parity. For example, $z \to -z$ leaves the Hamiltonian invariant and yields two classes of Bloch states $|\psi_{k,\eta}\rangle$ with mirror eigenvalues $\eta = \pm i$. For each of the values of η, one can define a mirror Chern number corresponding to it which leads to two topological invariants, a mirror Chern number and a total Chern number. The interesting thing is that a system can have a total zero Chern number while having a non-zero mirror Chern number. Theoretical predictions using ab-initio methods have predicted QWs of trivial insulators, e.g. (Sn/Pb)Te and Na(Cl/Br), with mirror Chern number $\eta = -2$ to be 2D TCI [59]. The crystalline symmetries however are unstable at the surface and so far only a few of the 2D TCI have been found as it is very difficult to stabilize thin films of 3D TCI. In the next section, we shall discuss this crossover to the 2D regime from the 3D case in great detail.

2.5 Dimensionality : two dimensions vs three dimensions

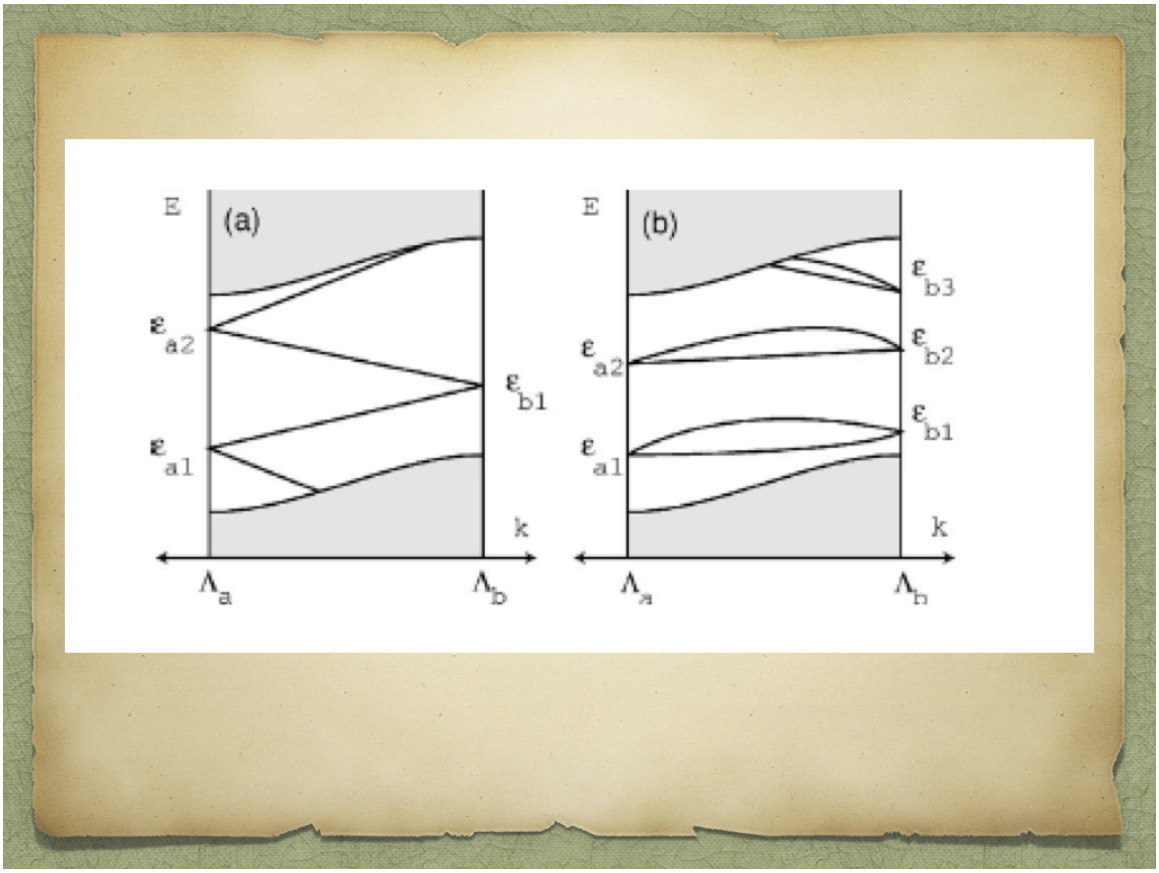

Figure 2.2: The edge states crossing the Fermi energy odd (a) and even b) number of times leading to topological and trivial surface states. The grey area is the bulk continuum. Adapted from [44].

In 2D, one can see that a QSH or topological state is achieved if the edge states traverse the bulk energy gap, crossing the Fermi energy E_F an odd number of times between two TRIM at the 1D edge λ_a and λ_b as is seen in Figure 2.2 (a). In the insulating phase, the edge states are not topologically protected and cross E_F an even number of times if at all seen in Figure 2.2 (b). In 3D, for the $(0\,0\,1)$ case, there can be three situations- one with 0 (4) Dirac cones, one with 1 (3) Dirac cones and another with 2 Dirac cones. Apart from the first case, the last two must have surface states connecting the bulk conduction and valence band. But unlike 2D, these surface states can exist at different surfaces, i.e the top or the bottom surface. For clarity, one can consider that in the 3D bulk , k_x, k_y, k_z are

good quantum numbers but on the surface, k_z is no longer a good quantum number and can be replaced by $-i\partial/\partial z$. This would imply that the two solutions (or the two surface states) live on opposite edges of the material and are separated by the bulk in between them. They can be interpreted as layered 2D QSH phases stacked in a particular direction. For the first and the last case, a doubling of the unit cell will bring the Dirac cones to lie on top of each other and any perturbation can open up a gap. These are what we refer to as the "weak" TI while the situation with 1 (3) Dirac cones is robust and is the "strong" TI. If E_F lies at the Dirac point, then this system becomes a TR invariant system with 1D parity anomaly devoid of fermion doubling [60, 61, 62, 39] . This occurs due to the fact that the Dirac point partners lie on opposite surfaces. And at one of the surfaces, a generic surface Fermi arc will enclose a single Dirac point. This will then define a 2D *topological (semi) metal* that has topological protection because of a quantized π Berry phase. For a thin slab of 3D TI, the boundary modes from the opposite surfaces may be coupled by quantum tunnelling, so that a small, thickness-dependent gap is opened up. In Bi_2Se_3 films, the gapped surface states also exhibit sizeable Rashba-type spin-orbit splitting because of the substrate-induced potential difference between the two surfaces. For thick films or the bulk-like limit, there is a clear signature of the surface state conduction due to one Dirac cone. But as thickness is reduced, the lack of inversion symmetry leads to a Rashba-like spin-splitting of the cones [63]. But could these topological surface states also exist in TMOs? The next section details the answer to this question.

2.6 Topology in oxides

A priori, there was no reason to expect that TMOs, which are seemingly trivial insulators with large band gaps and were very difficult to tune (greater than semi-conductor topological insulators at any rate), would be of any topological interest. But with the discovery of a metallic state at the surface of certain TMOs and strong spin-orbit coupling, interest began to be revived. STO $(0\,0\,1)$ at its surface has a confined 2DEG and as we shall see in the following chapter, it will be the spin-orbit coupling due to the Ti atom that will lead to a band inversion near some points at the surface BZ. These band inverted points,

reminiscent of a BHZ type model, will then be predicted to give topological edge states. But this is not just the only interesting candidate; at the $(1\,1\,1)$ surface of STO itself, there might be a possibility of having both band inversion and a topological crystalline metallic phase. In KTO $(1\,1\,1)$ which had a very strong SOC due to the Ta atom, a parity inversion a la Kane and Mele was predicted to occur at the $\bar{M}$ points in the BZ, leading to a topological state [35]. This could very well be the case for LAO/STO $(1\,1\,1)$ where all the necessary ingredients for a TCI are present. Another possibility of having a topological state driven by spin-orbit coupled band inversion is also presented in Chapter 4. The last compound to be discussed in Chapter 5, CTO $(0\,0\,1)$, where a 2DEG is also present, may very well turn out to be topological as well. From ab-initio calculations, it seems like the structure of CTO might resemble that of iridates which are predicted to be topological metals. The only difference being that SOC does not appear to be particularly substantial in CTO as it is in the case of iridates.

Thus, we shall show in the coming chapters that all kinds of topology might exist in TMOs, protected by different symmetries. We shall focus only on the perovskite family of TMOs, namely STO, LAO/STO and CTO. These oxides, which have a metallic sheet confined to a few nanometres within the surface, will be considered effectively as 2D systems. Thus, in order to explain their topological properties, we shall always draw parallels from 2D TI or TCI rather than their 3D counterparts. Even though transition metal iridates can be considered to be 3D topological metals, we shall not delve into their details for we shall restrict ourselves to those oxides which can be considered as effective 2D materials. One of the biggest challenges experimentally will be the detection of these topological states which is to be discussed in the next chapter. The co-existence with metallic states at the surface could be a challenge as disentangling the metallic and topological states will not be trivial.

Chapter 3

$SrTiO_3$ and $LaAlO_3/SrTiO_3$ at their $(0\,0\,1)$ oriented surfaces

3.1 Introduction

The more original a discovery, the more obvious it seems afterwards.

Arthur Koestler

$SrTiO_3$ (STO) has been extensively studied since the last fifty years and has a plethora of interesting properties even in the bulk, some which will be briefly mentioned. In the absence of doping, it behaves like a quantum paraelectric insulator which is indicative of the presence of quantum fluctuations at a low temperature ($\sim$ 4 K [64]) preventing the establishment of ferroeletricity. Despite this fact, if temperatures are raised and strain added, then STO becomes ferroelectric. On doping with Nb, STO also shows signs of superconductivity [3]. However we shall be interested in the undoped and unstrained bulk of STO which remains a band insulator, with a direct gap of $E_g = 3.5$ eV (indirect 3.2 eV) and we shall focus our attention on the band structure. To better understand the band structure, first at the bulk and then later at the surface, each of the different perturbations affecting STO will be discussed. Firstly, the crystal field splitting will be invoked to narrow down the number of pertinent orbitals required for the band structure by using symmetry arguments. Once crystal field has simplified our life, bulk conduction bands are investigated using tight-binding theory, and are found to be of d character and more specifically of t_{2g} character which is the lower manifold of the crystal field split d orbitals. The valence bands are found to have mainly an O $2p$ character. Thus, a simplified model using just the $3d$ conduction bands of Ti and the O $2p$ bands can be made to understand the band structure of STO. Once the interesting orbitals have been established, we will add bulk spin-orbit coupling to the mix and see the consequences on the band structure. Then we shall move to the surface by briefly recapping the experimental results, namely that of finding a 2D electronic gas confined to the surface, and then theoretically explain each of the perturbations that come into play at the surface. To this effect, we shall first begin by understanding the role of the confinement potential, then the role of the orbital mixing term. Once we have established all the perturbations qualitatively, we shall delve into the quantitative understanding of each of these perturbations and their impact on the band

structure. For each of these perturbations to have considerable impact on the underlying band structure, the energy scales have to be kept in mind. However the energy scales evolve with the band structure in the Brillouin Zone (BZ) and unexpected results will be found at unusual points in the BZ. The manifestation of topology will again be governed by the energy scales and it will be a challenge to be able to observe them.

3.2 Introductory elements for studying band structures

3.2.1 Effect of the Crystal field on $SrTiO_3$

In this section, we shall omit the spin state of each energy state as well as couplings like the spin-orbit coupling which will be treated in great detail in the next section. We shall discuss the effects of the crystal field or the ligand field on the symmetry of the five d orbitals and how their degeneracy in energy is affected. Orbitals belonging to the same irreducible representation (hence having the same label) are degenerate in the crystal field theory. The amplitudes and signs of the splitting, however, have to be determined from numerical calculations or experimental data, as they depend on the specific crystal distortion under study. In the absence of ligands (spherical symmetry), all the five d orbitals $d_{xy}, d_{yz}, d_{xz}, d_{z^2}, d_{x^2-y^2}$ remain degenerate in energy as they belong to the same irreducible representation of the continuous group of rotations labelled by the angular momentum $L = 2$. The first three orbitals have their lobes 45° with respect to the axes while the last two have lobes pointing along the axes as shown in Figure 3.1. Their form will become important when the ligand field is applied to determine how the degeneracy is removed. In the presence of ligands in an octahedron formation (represented by the O_h point group), the orbitals with their lobes pointing in the apical direction ($\hat{z}$) or the planar ($\hat{x}, \hat{y}$) directions, experience the ligand field strongly.

The d orbitals split to two manifolds of degenerate orbitals - the d_{xy}, d_{yz}, d_{xz} which is denoted by t_{2g} and the $d_{z^2}, d_{x^2-y^2}$ denoted by the e_g, owing to their different forms. This splitting in experimentally observed to be about $2eV$ with the e_g manifold being raised in energy with respect to the t_{2g}. As a consequence, the conduction band manifold is

composed of a majority of the t_{2g} orbitals.

Below 105 K, STO undergoes a structural transition from cubic to tetragonal (D_{4h} point group) with a rotation of the oxygen octahedra accompanied by a small extension of the c-axis (at 4 K $c/a \equiv 1.001$) [65, 66, 67]. This transition slightly handicaps the planar orbitals, shifting the d_{xy} state 3 meV higher in energy relative to the d_{yz} and d_{xz} orbitals. A similar effect is observed for the e_g with the $d_{x^2-y^2}$ orbital being raised 3 meV in energy as compared to the d_{z^2} orbital [65]. If now a symmetry change due to either a trigonal or a tetragonal ligand field in the plane is assumed, this splits the two manifolds further. At the surface, the inversion symmetry along the $\hat{z}$ direction is broken which will also remove the degeneracy of the three t_{2g} orbitals. For the rest of the discussion, we shall focus on the t_{2g} manifold as it is lowest in energy and the difference in energy for the two manifolds is significant so as not to have any impact of the e_g on the properties of STO in the bulk or the surface.

3.2.2 Tight-binding formulation

Once the nature of the conduction band is understood, the next step is to move to a kinetic description of the motion of electrons in the conduction band. An efficient way to do so is to consider the tight-binding approach or the Linear Combination of Atomic Orbitals (LCAO) approach. In the LCAO formulation, the electron is assumed to be localised at a site in a lattice and has a finite amplitude of moving from one site to another. It is to be noted that the basis used in this approach is that consisting of the localised atomic orbitals (in our case of Ti). In STO, the orbitals involved are t_{2g} and the hopping is mediated by an oxygen in between two Ti atoms. The hopping amplitude is distance and direction dependent in the case of STO. For each of the planar t_{2g} orbitals, if the hopping is restricted to the nearest neighbours, there are two *light* and one *heavy* direction of hopping depending on the direction of their lobes. For the d_{xy} orbital, the hopping in the $\hat{x}$ direction is facilitated by a O p_y orbital orientated along the $\hat{x}$ direction which leads to an effective overlap. Similarly, in the $\hat{y}$, direction, the hopping is facilitated by O p_x orbital along the $\hat{y}$ direction. These are the so-called *light* directions of hopping. However along the $\hat{z}$ direction, no orbital of O has an effective overlap and hence the hopping is weak. This is the *heavy* direction of hopping.

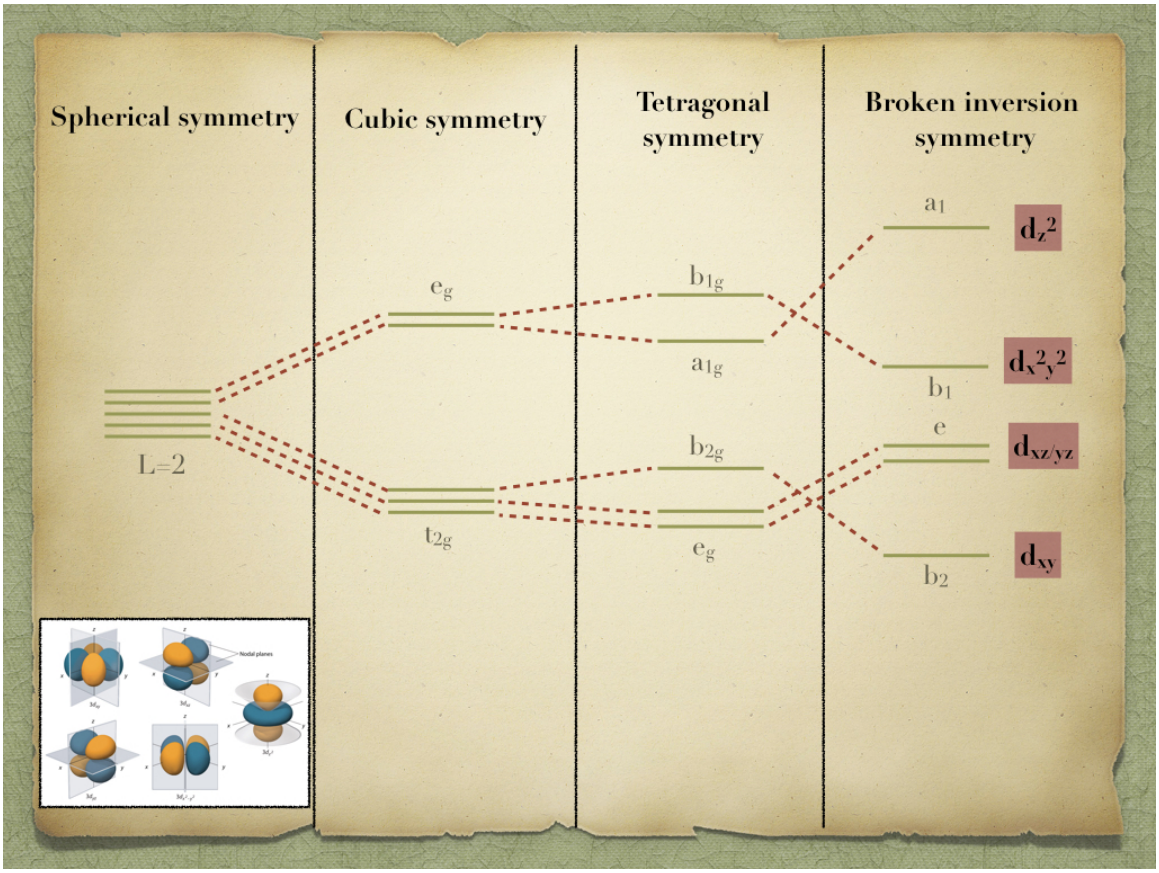

Figure 3.1: The effects of crystal field on the Ti atom is shown. First all the d orbitals are degenerate in spherical symmetry and then the splitting is seen in cubic, tetragonal symmetry to finally the surface where inversion symmetry is broken. An inset on the lower left corner shows the form of all the five d orbitals.

The rest of the hopping terms involving other p orbitals are prohibited by symmetry as the t_{2g} electrons cannot change the nature of the electrons as they hop from one site to another either. For example, an electron cannot hop from d_{xy} orbital to a d_{yz} orbital as there is no overlap with any surrounding oxygen atom.

For this p-d hybridization, we can assign a t_{pd} hopping amplitude for the process described above. Owing to a parity difference in the p and d orbitals, the t_{pd} changes sign as the direction of the hopping is changed. To the leading order of this virtual hopping t_{pd} via the oxygens, the Hamiltonian in the basis of spin independent d_{xy}, d_{yz}, d_{xz}, the nearest

neighbour hopping, in the absence of any defects, is given by

$$H_0 = \begin{bmatrix} E_{d_{xy}} & 0 & 0 \\ 0 & E_{d_{yz}} & 0 \\ 0 & 0 & E_{d_{xz}} \end{bmatrix} \tag{3.1}$$

where the diagonal entries are

$$E_{d_{xy}} = -2t_1(1-\cos(k_x a)) - 2t_1(1-\cos(k_y a)) - 2t_2(1-\cos(k_z a)) \tag{3.2}$$

$$E_{d_{yz}} = -2t_2(1-\cos(k_x a)) - 2t_1(1-\cos(k_y a)) - 2t_1(1-\cos(k_z a)) \tag{3.3}$$

$$E_{d_{xz}} = -2t_1(1-\cos(k_x a)) - 2t_2(1-\cos(k_y a)) - 2t_1(1-\cos(k_z a)) \tag{3.4}$$

with a being the lattice parameter and t_1 and t_2 signifying the light and the heavy hopping for each of the t_{2g} orbitals and $t_{1,2} = (t_{pd}^2)_{1,2}/\Delta E_{pd}$ where ΔE_{pd} is the splitting between the p and d atomic orbitals of oxygen and titanium respectively. These effective metal-metal hopping are composed of even terms and do not lead to any Rashba-like splitting (which needs odd terms if combined with the on-site bulk SOC which will be treated in the next section). The next nearest neighbours have been excluded for simplicity and for the fact that the coupling or hopping is too weak to make a significant impact on the band structure. The symmetries preserved here are the spin, space inversion and time-reversal and hence these bands are four times degenerate. The other states, for example, the core states of Ti, O and Sr lie far below the E_F and other unoccupied bands of Ti, O and Sr lie much higher up in energy. Thus, a low energy Hamiltonian can be constructed from the reduction of the Hilbert space from a hybridization between O $2p$ states and Ti t_{2g} states and then to an effective model with hopping from Ti to Ti sites. Another effect which will become important at both the bulk and at the surface is the spin-orbit coupling (SOC) in its bulk form.

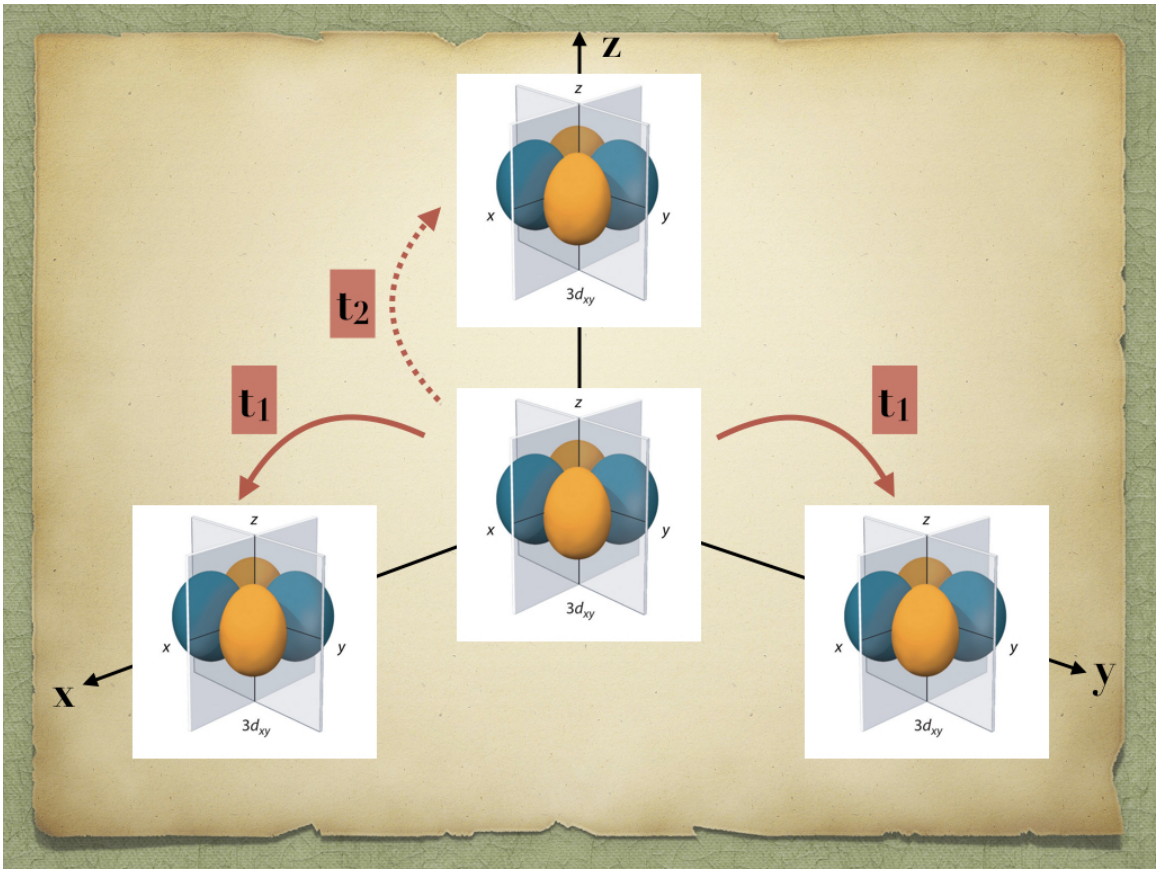

Figure 3.2: The effective model with Ti to Ti hopping is shown for a d_{xy} orbital with t_1 being the "light" directions along the $\hat{x}$ and the $\hat{y}$ directions and t_2 being the "heavy" direction along the $\hat{z}$ direction.

3.2.3 Bulk spin-orbit coupling

The spin-orbit interaction is a relativistic effect that couples the angular momentum of an electron with its spin, leading to a spin-momentum locking. In the rest frame of the electron, which is in fact, moving around the nucleus, the electron experiences an effective magnetic field $\mathbf{B_{eff}} = -\mathbf{v}/c \times \mathbf{E}$. For an electron with a magnetic moment $\mathbf{m}$ (given by its spin $\mathbf{S}$), it results in an interaction between $\mathbf{B_{eff}}$ and $\mathbf{m}$ that can be expressed with a Hamiltonian term of the form $H_{SO} = -\mathbf{m} \cdot \mathbf{B_{eff}}$. This can be simplified to

$$H_{SO} = -\frac{\hbar}{4m_e^2c^2}\boldsymbol{\sigma} \cdot \mathbf{p} \times \nabla \mathbf{U} \tag{3.5}$$

where c is the velocity of light, σ the Pauli matrices, p the linear momentum and ∇U the

gradient of the potential. For a simple atom like hydrogen, this is just the atomic potential and after some simplifications, this term can be written as

$$H_{SO} = -\lambda \mathbf{L} \cdot \mathbf{S} \tag{3.6}$$

with $\lambda = \frac{e^2}{8\pi m_e^2 c^2 \epsilon_0 r^3}$ [68]. However this simple form cannot be assumed in the lattice as the periodic potential is different from the atomic one. Fortunately in the bulk of a material, the gradient of this potential is expected to be relatively close to the heavy (Ti) atoms composing the bulk. In addition to the atomic potential approximation, the tight-binding method also supposes that the atomic orbitals are a good approximation to the Bloch states. Thus, the matrix elements of the H_{SO} with the crystal wave functions can be replaced by those with the atomic orbitals of Ti. The action of the bulk SOC or the$\lambda \mathbf{L} \cdot \mathbf{S}$ on the Ti t_{2g} orbitals is given in the basis of $|xy;\uparrow\rangle, |yz;\uparrow\rangle, |xz;\uparrow\rangle, |xy;\downarrow\rangle, |yz;\downarrow\rangle, |xz;\downarrow\rangle$ as-

$$\begin{bmatrix} 0 & 0 & 0 & 0 & \lambda' & -i\lambda' \\ 0 & 0 & i\lambda' & -\lambda' & 0 & 0 \\ 0 & -i\lambda' & 0 & i\lambda' & 0 & 0 \\ 0 & -\lambda' & -i\lambda' & 0 & 0 & 0 \\ \lambda' & 0 & 0 & 0 & 0 & -\lambda' a \\ i\lambda' & 0 & 0 & 0 & i\lambda' & 0 \end{bmatrix} \tag{3.7}$$

where $\lambda' = \lambda/3$.

If the bulk SOC is added to the tight-binding Hamiltonian in Eq. (3.1), electronic states with different spatial symmetries are mixed and the initial t_{2g} states (or the Γ_5^+ states) are no longer eigenstates of the system. This results in two states, one twice degenerate Γ_8^+ states, lower in energy and a spin-split off state Γ_7^+, raised by 25-30 meV at the Γ point as seen in the theoretical calculations by Zhong et al [69]. Γ_7^+ and Γ_8^+ correspond to the irreducible representations of the O_h double group to which the Γ point spin-orbit split bands belong. It is to be noted that spin degeneracy has been removed and the effect of the bulk SOC is felt most at the Γ point where the t_{2g} orbitals were earlier degenerate. It is also at the Γ point where the eigenstates have a mixed t_{2g} character but regain their pure orbital character

as one moves away from the Γ point. At low temperatures, the SOC splitting overcomes the splitting due to the tetragonal distortion of the STO lattice at Γ. Due to their relative energies, confinement at the surface dominates the SOC at Γ. However, it is to be kept in mind that the only interesting point in the BZ is not Γ and we shall find another effective Γ point where the bulk SOC will become a very important effect. It is also to be noted

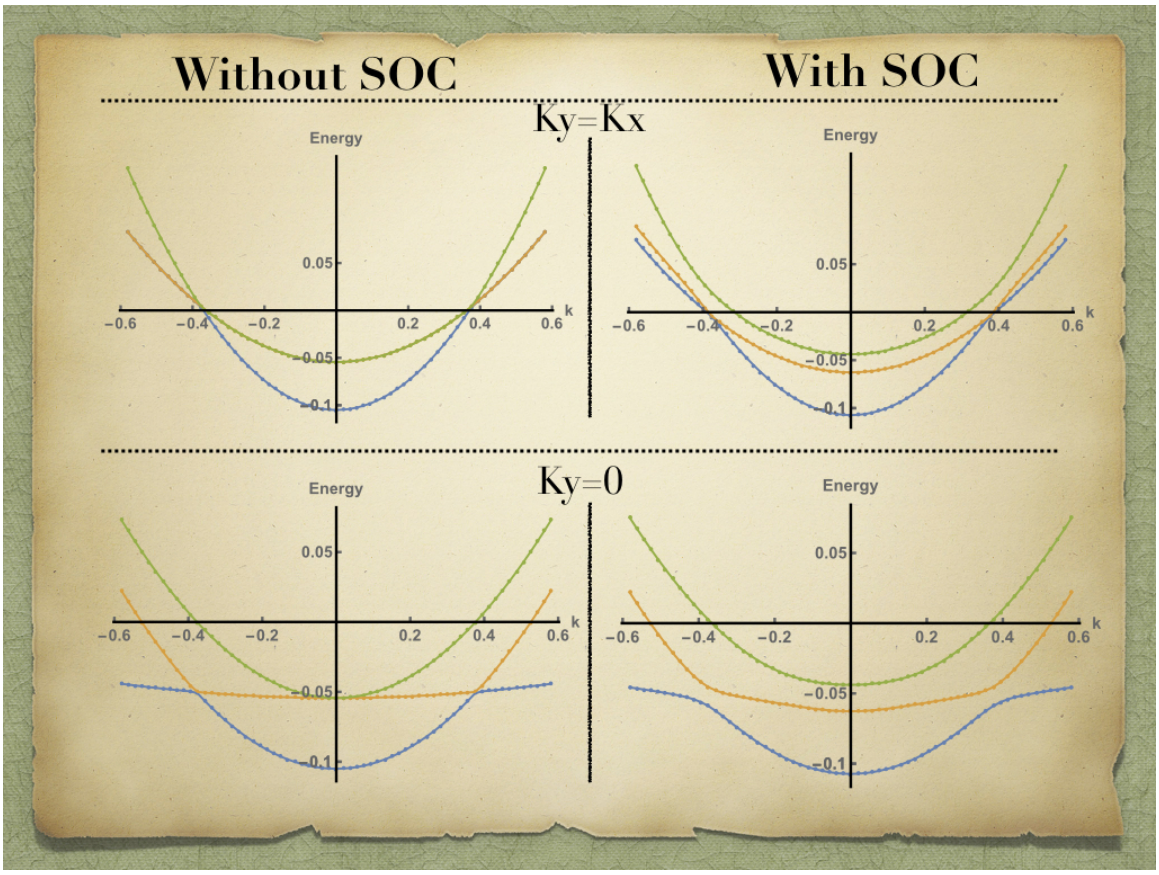

Figure 3.3: The bulk tight-binding bands with and without bulk SOC are shown in two orientations in the BZ- $k_y = k_x$ and $k_y = 0$ to contrast the difference in the band structures.

that at this stage, $H_{tb} + H_{SO}$ preserves inversion symmetry ($\mathbf{R} \rightarrow -\mathbf{R}$) but at the surface, this symmetry will be broken. Now that we have understood the effect of each perturbation in the bulk on the band structure, the time is ripe to move on to the surface. In the next section, we shall discuss the surface of STO, first experimentally and then theoretically.

3.3 Experimental discovery at the $(0\,0\,1)$ surface of $SrTiO_3$

In 2011, interest was revived in STO, when a 2DEG was found to exist at its (001) surface [8, 70]. Its origin is ascribed to oxygen vacancies confined to the surface of STO. To characterise it theoretically, the electronic structure, derived from spin-integrated ARPES experiments, was interpreted in terms of sub-bands . The sub-band structure is thought to be caused by the confinement potential, modelled by a triangular quantum well, which pins the 2DEG at the surface. This confinement potential also has another important effect; it overcomes the bulk SOC effect to lower the d_{xy} states by about 200 meV below E_F, giving metallicity and raising the d_{xz}, d_{yz} states above the d_{xy}, thus, reversing the order of the bands. The two dimensionality of the gas was also revealed by the lack of dispersion in the $\hat{z}$ direction. The dominant orbitals in the conduction bands were shown to be the t_{2g} d states of Ti and those in the valence bands were shown to be O $2p$ states.

Subsequently, Spin-Polarised ARPES was performed and spin polarisation was found for the two sub-bands seen earlier in spin-integrated ARPES [9]. The data was interpreted as spin split bands with oppositely winding spin chiralities at the Fermi surface. The spin textures observed were a consequence of the surface Rashba effect, which arises due to the assymetry of the potential going from the bulk to the vacuum at the surface and a bulk SOC. The consequence is a momentum dependent spin-splitting of the bands and for more details about the Rashba effect, the reader is referred to an excellent book by R. Winkler [71].

An issue raised with the detection of spin polarised bands was the presence of internal magnetism and spin-split bands [9, 72], which is one we will discuss further when we probe our system for possible topological states.

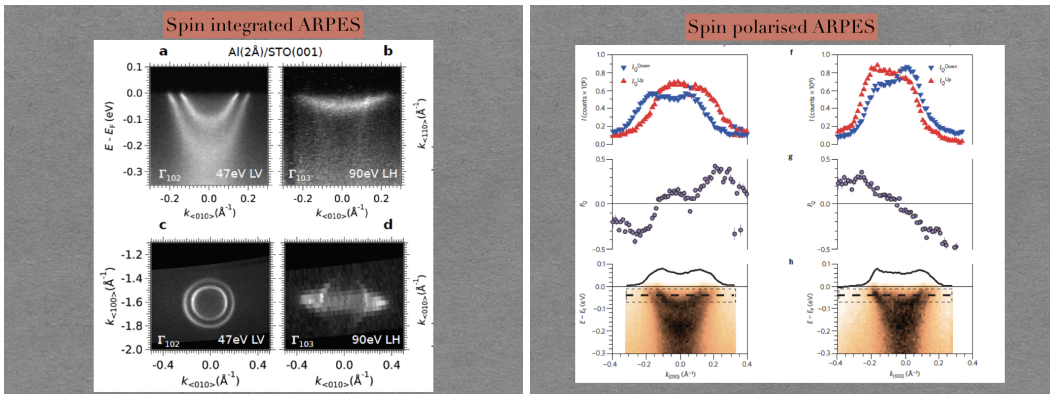

Figure 3.4: Spin integrated and spin polarised ARPES band dispersion and Fermi surface maps show two dispersive bands of dominant d_{xy} character and less dispersive band of dominant $d_{xz/yz}$ character which are also spin polarised. Taken from [8, 70, 9].

3.4 Theoretical modelling for understanding the surface spectrum of $SrTiO_3$

3.4.1 Confinement potential created by vacancies

The oxygen vacancies created either due to the ARPES beam (uv radiation) or the layer of Al deposited on the sample, lead to two effects. Firstly, they supply the necessary electrons for the 2DEG and secondly they give rise to the confinement potential which keeps the gas pinned to the surface. They can be seen as donors of electrons and as regions of positive localized charges which create a potential. This potential is modelled by a wedge or a triangular well which confines states close to the surface. Its form is given by $V(z) = V_0 + eFz$ [8] and acts only in the direction perpendicular to the surface, i.e. $\hat{z}$. Here, V_0 is a constant for all the bands and is negative, resulting in a downward shift for all the bands (conduction and valence) and F is the strength of the electric field. The eigenenergies of states confined in this quantum well are given by [73, 74]-

$$E_n = V_0 + \left(\frac{\hbar^2}{2m_z^*}\right)^{1/3} \left[\left(\frac{2\pi}{2}\right)\left(n - \frac{1}{4}\right) eF\right]^{2/3} \tag{3.8}$$

where $n = 1, 2, 3...$ and m_z^* is the effective mass in the $\hat{z}$ direction. The exact eigenenergies have $n - \frac{1}{4}$ in this equation replaced by $0.7587, 1.7540,$ and 2.7575, respectively, for the three lowest solutions [74]. Following this approach, one can get the form of the well using the experimental data as used in [8] using the effective masses also derived from experiments. This gives the position of the d_{xy} sub-bands 1 and 2 in the well, which is lower in energy than the first heavy d_{xz}/d_{yz} sub-bands in the well. This constitutes a change in the orbital (or band) order and induces the bands to cross. This valuable information can be then used in the tight-binding modelling to give us the finer details of the band structure.

But this is not the only means to model the shape of the confinement potential. Poisson-Schrodinger calculations, which use the charge density and the spatial extension of the wave functions, give a much better approximation to the triangular wedge. At the beginning, an assumption for the shape of the potential is made and in our case, it is that of a triangular wedge. Owing to the confinement, the k momentum can be decomposed into the periodic in-plane $k_{||}$ and the envelope function $\xi_n^\alpha(z)$ which is the solution of the 1D Schrodinger equation in the confining potential $V(z)$ denoted by-

$$-\frac{\hbar^2}{2m_z^{*,\alpha}}\frac{\partial^2\xi_n^\alpha(z)}{\partial z^2} + eV(z)\xi_n^\alpha(z) + E_0^\alpha\xi_n^\alpha(z) = \epsilon_n^\alpha\xi_n^\alpha(z) \tag{3.9}$$

The term E_0^α signifies the bottom of the band α in the bulk and since the three t_{2g} bands are degenerate if one neglects the tetragonal distortion and the bulk SOC, the E_0^α can be set to zero. The wave function is then written as $\psi_{n,\mathbf{k}_{||}}^\alpha(\mathbf{r}) = \frac{e^{i\mathbf{k}_{||}\mathbf{r}_{||}}}{2\pi}\xi_n^\alpha(z)$ and its energy given by $E_n^\alpha(\mathbf{k}_{||}) = \frac{\hbar^2k_x^2}{2m_x^{*,\alpha}} + \frac{\hbar^2k_y^2}{2m_y^{*,\alpha}} + \epsilon_n^\alpha$. It is to be noted that the effective masses used here are the experimental values at the surface so as to incorporate any change of bandwidth at the surface that could have taken place for the bulk bands - $m_y^* \approx 0.7m_e$ and $m_z^* = 10 - 20m_e$ where m_e is the rest mass of an electron. Under these assumptions, the 3D charge density profile is given by-

$$\rho_{3D}(z) = e\sum_{n,\alpha}\Theta(E_f - \epsilon_n^\alpha)\frac{\sqrt{m_x^{*,\alpha}m_y^{*,\alpha}}}{\pi\hbar^2}(E_f - \epsilon_n^\alpha)|\xi_n^\alpha(z)|^2 \tag{3.10}$$

with Θ being the heaviside function assuming the calculations be done at $T = 0K$. This 3D

density obtained from the Schrodinger equation can then be input in the Poisson equation to give the new profile of the potential.

$$-\frac{\partial}{\partial z}\left(\epsilon_0\epsilon_r(E)\frac{\partial V(z)}{\partial z}\right) = \rho_{3D}(z) \tag{3.11}$$

This new potential obtained is compared to the initial guess and for the next step, a mixture of the two is taken. The Schrodinger equation is again solved to get a charge density and then the Poisson equation is solved with this charge density to get a new potential profile. This procedure is repeated until self-consistency is achieved at a chosen convergence criterion and a final form of the potential well along with the sub-band structure for the three t_{2g} orbitals is obtained [75]. It is to be noted that there is a change in the boundary conditions when a gate voltage is applied.

This procedure gives an excellent idea of the different sub-bands involved and their energies at Γ which can be then used in tight-binding modelling. It should be mentioned that the dielectric constant depends strongly on the temperature and the electric field applied. Being extremely high at low T and reaching a value of $\epsilon_r = 21600$ [75, 76], it leads to a very effective polarization and a complete screening of the electric field. There is also a dependence on the electric field which is given by Ueno [73] and Stengel [77] and experimentally [75] which suggests an $\epsilon_r \propto E^{-2/3}$ dependence. Thus, the larger the field, the stronger the depolarising field for STO. This has consequences on the charge density ρ_{3D} and changes the confinement of the gas as a gate voltage is applied; the gas becomes more confined for a negative back gate and less confined for a positive back gate voltage. It also has effects on the surface where the defects lie and the interplay between the two will be crucial for understanding the next term to be added to the modelling, that of orbital mixing.

3.4.2 Orbital mixing term at the surface

At the surface, another term comes into play due to the defects caused by the oxygen vacancies. As discussed earlier in the introduction, having a surface entails a rotation and tilting of the octahedra and impacts the electrostatic energy and these features are amplified if defects are introduced. It is to be noted that these effects will also have a

dependence on the electric field as the dielectric constant and hence the shape and strength of the confinement potential depends on the field. The excess electrons are believed to originate from these defects/vacancies and give rise to a carrier density of the 2DEG which is uniform and extremely high reaching up to an order of $1.5\times\ 10^{14}$ cm^{-2}. The defects at the surface can be presumed to be uniform because of this large value of the carrier density. The defects will also induce new hopping pathways for the electrons as the Ti-O-Ti bond angle is changed. In particular, it is the defect induced confining potential which will induce new pathways and these can be grouped under lattice polarization and orbital polarization. Lattice polarization is the motion of the Ti and O atoms away from their equilibrium position while orbital polarization is the deformation of the lobes of the atomic orbitals of Ti and O. Due to their positive ionic charge, the Ti atoms are pushed away from the interface while the O atoms are attracted to the interface. This results in the rumpling or the buckling of the TiO_2 plane. It is this latter phenomenon rather than the orbital polarization which will lead to new hopping pathways according to Khalsa et al. [78]. This would mean that a d_{xz} orbital will now be connected to a d_{xy} via an O p_x in the $\hat{y}$ direction and similarly a d_{yz} orbital will now be connected to a d_{xy} via an O p_y in the $\hat{x}$ direction. We can think of this as a perturbation arising from a potential of the triangular wedge form that we had explicited earlier $-eEz$ and the induced hopping as $E\gamma_1$ where $\gamma_1 = \langle d_{xz}, \mathbf{R} = \mathbf{0}| \, |-ez| \, |p_x, \mathbf{R} = a/2\hat{y}\rangle$. In addition, the metal-oxygen bond angle has also been distorted from the planar one (zero $\hat{z}$ component) which introduces a non zero $\hat{z}$ component in the direction cosine of the bond axis. These terms will change sign depending upon the direction due to the nature of the d-p orbitals involved and will result in the odd terms which will produce the Rashba effect. The Hamiltonian in the basis of spin independent d_{xy}, d_{yz}, d_{xz}, is given by

$$H_{OM} = \begin{bmatrix} 0 & 2it_r \sin(k_x a) & 2it_r \sin(k_y a) \\ -2it_r \sin(k_x a) & 0 & 0 \\ -2it_r \sin(k_y a) & 0 & 0 \end{bmatrix} \tag{3.12}$$

where $t_r = (\gamma_1 t_{pd} E)/\Delta E_{pd} + (n t_{pd}^2/\Delta E_{pd})$. It is to be noted that the space inversion symmetry $\mathbf{R} \rightarrow -\mathbf{R}$ is broken here resulting in a removal of degeneracy in the bands

which will be shown later. There is, however, no overlapping between a d_{yz} and a d_{xz} orbital as no oxygen can mitigate the electron transfer.

3.5 Band structure at the $(0\,0\,1)$ surface of $SrTiO_3$

To begin understanding the surface band structure, it is important to start from scratch, or in other words, begin from the bulk. STO is known to be a band insulator in the bulk in the absence of any defects. In the cubic phase, the empty conduction band is composed of the three t_{2g} states of the d-orbital of Ti, namely the d_{xy}, d_{yz} and d_{xz} orbitals, twice degenerate because of spin. If the band structure is observed then at the Γ point there is a degeneracy of all three t_{2g} orbitals and no band crossings. In the presence of bulk spin-orbital coupling, $\lambda L.S$, the spin and orbital degrees of freedom for the t_{2g} are interlocked, resulting in degenerate Γ_8^+ states and a spin-split off state Γ_7^+, raised by 25-30 meV at the Γ point.

3.5.1 Impact of the confinement potential

At the surface, confinement modifies the bands but affects each of the t_{2g} orbitals differently. This yields two terms, a global offset $-V_0$ impacting all three t_{2g} orbitals equally but also an individual offset term $\epsilon_{1/2}$ which affects each band differently. The latter is the term coming from the quantization of k_z in the direction perpendicular to the interface due to confinement. Since this is a term depending on the effective mass in the $\hat{z}$ direction, the orbitals $d_{xz,yz}$ are lowered less than the d_{xy} because the latter has a heavier mass in this direction than the other two. The energies now become

$$E^c_{d_{xy}} = -2t_1(1-\cos(k_x a)) - 2t_1(1-\cos(k_y a)) + \epsilon_1 + V_0 \tag{3.13}$$

$$E^c_{d_{yz}} = -2t_2(1-\cos(k_x a)) - 2t_1(1-\cos(k_y a)) + \epsilon_2 + V_0 \tag{3.14}$$

$$E^c_{d_{xz}} = -2t_1(1-\cos(k_x a)) - 2t_2(1-\cos(k_y a)) + \epsilon_2 + V_0 \tag{3.15}$$

and the Hamiltonian having these energies as diagonal entries will be noted as H^c_{TB}. It is to be remembered that V_0 is a constant and is negative while $\epsilon_{1,2}$ depends on the effective mass

of the band w.r.t. the $\hat{z}$ direction . The result is that the 1st (2nd) d_{xy} band is lowered by 200 (100) meV and the d_{yz}/d_{xz} bands by 50 meV. This results in a difference of 150 (50) meV between the first (second) light d_{xy} and first heavy $d_{yz/xz}$ bands. This effect dominates the bulk spin orbit coupling at Γ and removes the degeneracy of the bands. But this effect is even more dramatic, as the d_{xy} bands are lowest in energy, there is a reversal of the orbital order as compared to the bulk resulting in crossing of the bands in multiple directions in the BZ. These crossings are of two types-one involving two orbitals, one heavy and one light along the ΓX and ΓY direction while the other involves three orbitals in the ΓM or $\Gamma \bar{M}$ direction. It is the latter that we will investigate as interesting effects are observed in the vicinity of these points. By symmetry, there exist 4 such crossing points, each of which can be noted as Γ_{dp}. At this point, the three bands are degenerate again, leading to an effective Γ point being formed at this point, Γ_{dp}. So although confinement breaks the symmetry of the bands at Γ, in a certain sense this degeneracy is restored at the Γ_{dp} bringing in a new symmetry at the surface which now has four new "Γ" like points. The bands at Γ_{dp} will have a linear dispersion as compared to a quadratic dispersion at Γ. At Γ_{dp},

$$|k_x| = |k_y| = k_c = 2 \arcsin \left\{ \sqrt{\left[\left(\epsilon_2 - \epsilon_1 \right) / \left(t - t_h \right) \right]} \right\} \tag{3.16}$$

and the value of this crossing point can be predicted for any value of $\epsilon_{1,2}$, thus leading to the prediction of new crossing points between different sub-bands. The crossings here as seen in ARPES are between the first heavy and the second light sub-band close to the E_F but others might exist between other sub-bands above the E_F. The energy of Γ_{dp} can also be calculated and is shown to be

$$E^c(kc) = V_0 + \epsilon_1 + 2t_1 \frac{\epsilon_2 - \epsilon_1}{t_1 - t_2} \tag{3.17}$$

With this information, of the position of Γ_{dp} in k space and in energy, we can unearth various three band crossings.

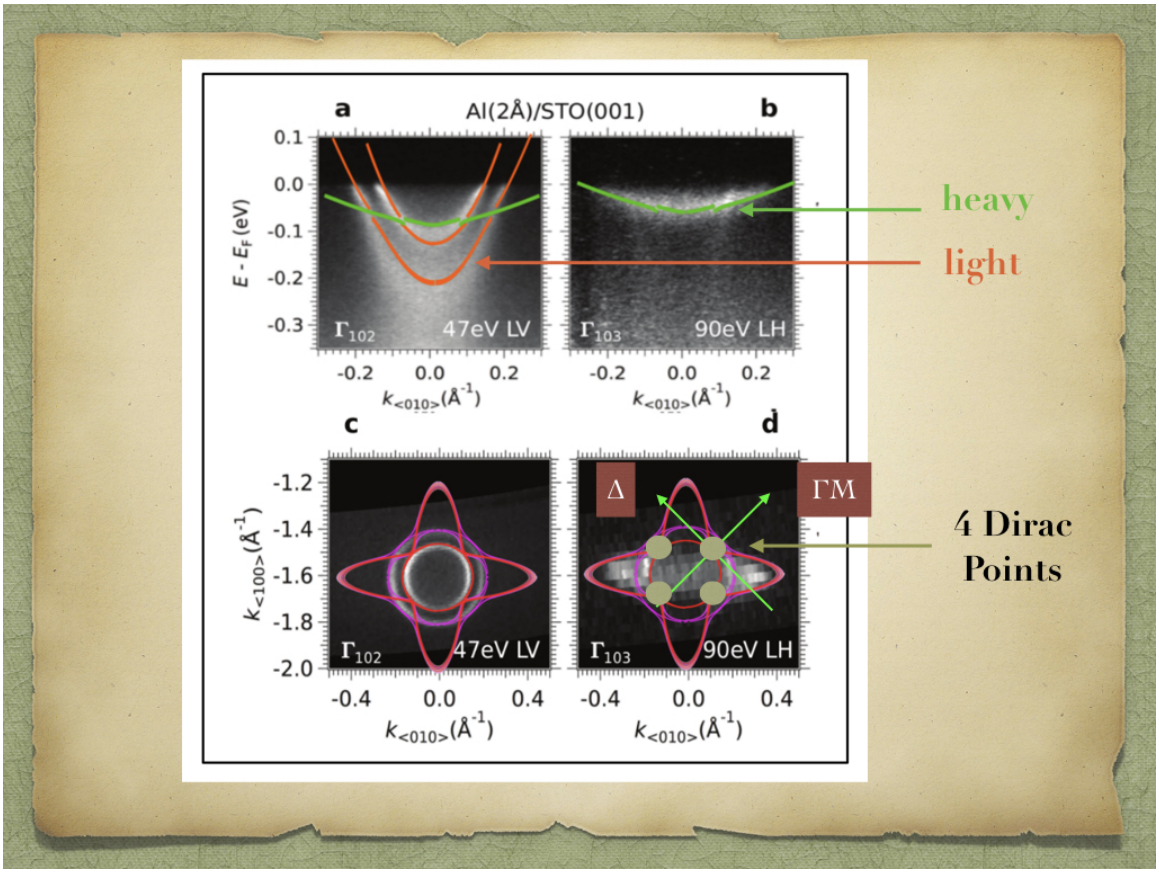

Figure 3.5: The surface tight-binding bands are overlaid on the ARPES band dispersion for $k_x = 0$ and Fermi surface map. Two kinds of bands, light and heavy are observed . The crossing points between all three orbitals, four by symmetry, are also shown. Adapted from [79].

3.5.2 The impact of bulk spin-orbit coupling on the surface spectrum

The bulk SOC is still important even if it is dominated by the confinement potential at Γ; the pure t_{2g} orbitals now become mixed and at Γ, even if the d_{xy} orbital is 200 meV lower, the lowest energy band is still a mix of majority d_{xy} and a minority $d_{xz/yz}$. The higher bands are also mixtures of all three t_{2g} orbitals. Bulk SOC becomes an important perturbation at the crossing points Γ_{dp} as the energies of the bands, which are now equal mixes of all three t_{2g} orbitals, are degenerate, and the dominant perturbation is bulk SOC rather than confinement. The bands at Γ_{dp} are sensitive to any perturbation and SOC causes a spin-split off band to appear, *while leaving two bands still degenerate*. The two lower energy bands which are degenerate at Γ_{dp} bear a strong resemblance to tilted Dirac cones and

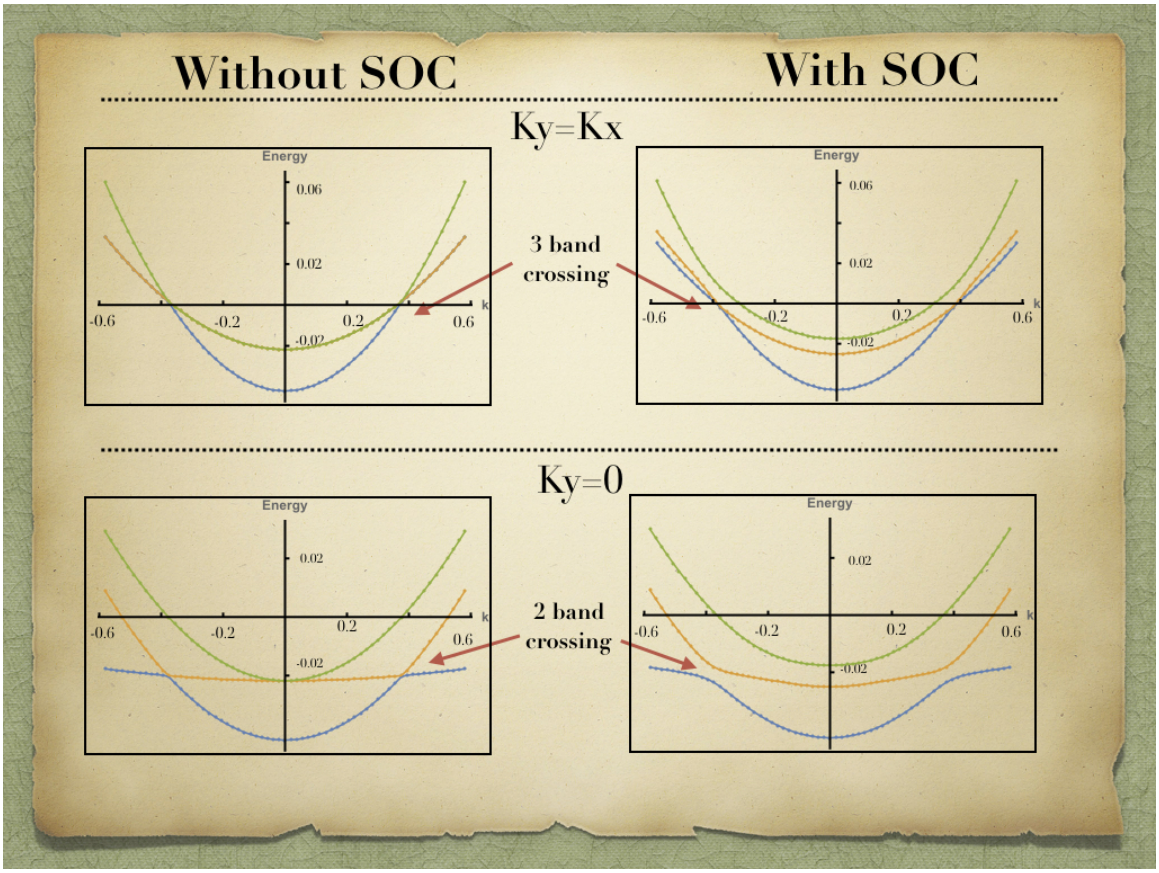

Figure 3.6: The surface tight-binding bands with and without bulk SOC are shown in two orientations in the BZ- $k_y = k_x$ and $k_y = 0$ to contrast the difference in the band structures. The crossing point between one and two orbitals is also shown.

if one moves around the Γ_{dp}, one sees that the tilt of these cones changes as a function of the direction or the orientation around Γ_{dp}. It is maximum in the ΓM direction and minimum in the direction perpendicular to ΓM and passing through Γ_{dp} such that one finds untilted Dirac cones in this direction denoted by Δ. The Dirac cones are four in total, each twice degenerate, one in each quadrant of the BZ and are related by C_{4v} and time reversal (TR) symmetries. If the magnitude of the bulk SOC is increased, the degenerate Dirac cones persist, signalling that they are protected against this perturbation. In fact, they are protected by TR and by space inversion symmetry in the plane. We note that, while the points Γ_{dp} are situated in directions of high symmetry, their crystal symmetry is lower than that of the special points Γ or M and $\bar{M}$. This feature allows for the existence of a tilt of the Dirac cones which would have been otherwise excluded [80, 81]. In fact the Hamiltonian $H^c_{TB} + H_{SO}$

has the following form in the basis of $|xy;\uparrow\rangle, |yz;\uparrow\rangle, |xz;\uparrow\rangle, |xy;\downarrow\rangle, |yz;\downarrow\rangle, |xz;\downarrow\rangle$

$$\begin{bmatrix} E^c_{d_{xy}} & i\lambda' & -\lambda' & 0 & 0 & 0 \\ -i\lambda' & E^c_{d_{yz}} & i\lambda' & 0 & 0 & 0 \\ -\lambda' & -i\lambda' & E^c_{d_{xz}} & 0 & 0 & 0 \\ 0 & 0 & 0 & E^c_{d_{xy}} & -i\lambda' & \lambda' \\ 0 & 0 & 0 & i\lambda' & E^c_{d_{yz}} & i\lambda' \\ 0 & 0 & 0 & \lambda' & -i\lambda' & E^c_{d_{xz}} \end{bmatrix} \tag{3.18}$$

with the energies being the same as those defined in Eq. 3.13 and the magnitude of the bulk SOC being the same as defined in Eq. 3.7.

If either of the blocks of the block diagonal Hamiltonian $H^c_{TB} + H_{SO}$ is now diagonalised either by using the Cardano formula to find roots of a cubic equation or numerically, the Hamiltonian now becomes:

$$\begin{bmatrix} E_a & 0 & 0 \\ 0 & E_b & 0 \\ 0 & 0 & E_c \end{bmatrix} \tag{3.19}$$

where E_b and E_c constitute the Dirac cones in the vicinity of the Γ_{dp} and the spin split off band is denoted by E_a, with eigenvectors as $|A\rangle, |B\rangle, |C\rangle$. Since the Dirac cones are of interest and the spin-split off band is separated in energy by 30 meV from them and the interesting physics will be around 3-5 meV, to the first order, we can project out this higher energy band. The projector used is of the form $\mathbb{P} = \mathbb{1} - |A\rangle\langle A|$. Once this is done, we will focus only on the sub-space spanned by the Dirac cones and the eigenvectors $|B\rangle$ and $|C\rangle$. Another trick which will be used is if the states spanned by $|B\rangle$ and $|C\rangle$ in the first quadrant are operated on by two symmetry operations, first C_2 and then TR, we shall find TR states of these eigenvectors at the same energy and at the same k points. These $|B\rangle$ and $|C\rangle$ along with their mirror and time reversed partners will be the basis of our Hamiltonian. Under the above stated conditions, we can construct the eigenvectors for our Hamiltonian devoid of orbital mixing and containing only the bulk SOC term. The choice of *lower* and *higher* energies refer to the lower (blue) and upper (yellow) block of the Dirac cone seen in Figure 3.7.

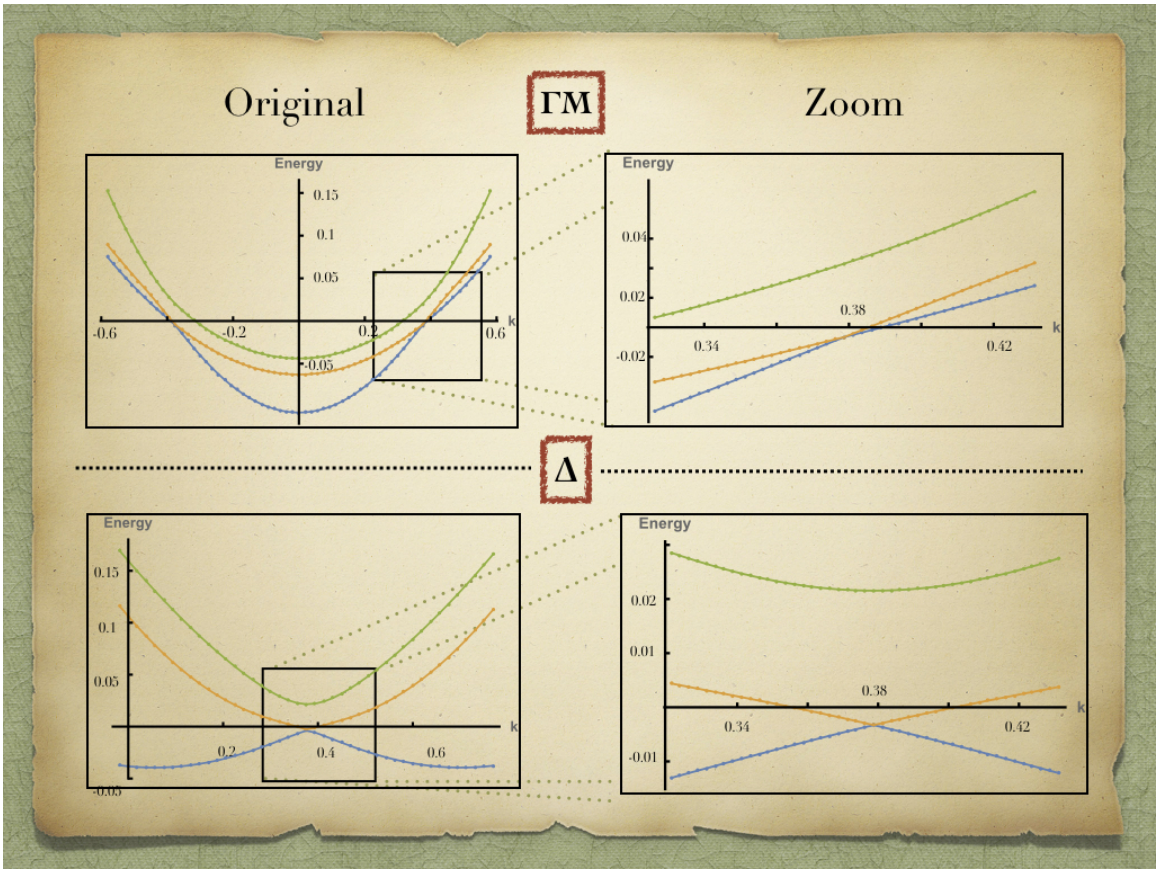

Figure 3.7: The surface tight-binding bands with bulk SOC are shown in two orientations in the BZ- $k_y = k_x$ or the ΓM and Δ orientation which is the direction perpendicular to ΓM passing thought the Dirac point. The tilt of the Dirac cones is maximal in the ΓM orientation as can be seen in the zoomed picture on the upper right corner and minimal in the Δ orientation seen in the zoomed picture at the bottom right corner.

The eigenvectors can be represented as B and C for the upper block of the block diagonal Hamiltonian and their time reversed partners B^* and C^* for the lower block of the Hamiltonian. The eigenvector corresponding to the lower eigenvalue e_1 in the upper block of the Hamiltonian is

$$|B\rangle = a_1 |xy;\downarrow\rangle + b_1 |yz;\uparrow\rangle - ic_1 |xz;\uparrow\rangle \tag{3.20}$$

The eigenvector corresponding to the upper eigenvalue e_2 in the upper block of the Hamiltonian is

$$|C\rangle = a_2 |xy;\downarrow\rangle + b_2 |yz;\uparrow\rangle - ic_2 |xz;\uparrow\rangle \tag{3.21}$$

The eigenvector corresponding to the lower eigenvalue e_1 in the lower block of the Hamiltonian is

$$|B^*\rangle = a_1 |xy;\uparrow\rangle - b_1 |yz;\downarrow\rangle - ic_1 |xz;\downarrow\rangle \tag{3.22}$$

The eigenvector corresponding to the upper eigenvalue e_2 in the lower block of the Hamiltonian is

$$|C^*\rangle = a_2 |xy;\uparrow\rangle - b_2 |yz;\downarrow\rangle - ic_2 |xz;\downarrow\rangle \tag{3.23}$$

with a_i, b_i, c_i being real coefficients for ($i \in (1,2)$). The form of the eigenvectors is non-trivial with branch cuts occurring at different directions in the BZ and a π shift of the branch cuts as one goes from the lower to the upper branch of the Dirac cones (See appendix A for more details). The Hamiltonian $H^c_{TB} + H_{SO}$, now simplified, takes the form

$$\begin{array}{c} \\ B \\ C \\ B^* \\ C^* \end{array} \begin{array}{c} \begin{array}{cccc} B & C & B^* & C^* \end{array} \\ \begin{pmatrix} e_1 & 0 & 0 & 0 \\ 0 & e_2 & 0 & 0 \\ 0 & 0 & e_1 & 0 \\ 0 & 0 & 0 & e_2 \end{pmatrix} \end{array} \tag{3.24}$$

Note that the bulk SOC is added between the second d_{xy} band and the first $d_{xz/yz}$ bands which form the basis for our model. The energy scale of the bulk SOC is so small that it acts as a minor perturbation everywhere in the BZ except at the Dirac points. Since the Dirac points are formed by the second d_{xy} and the first $d_{xz/yz}$ bands, it is a reasonable approximation to add the bulk SOC in this basis.

3.5.3 Impact of the Orbital Mixing term

Having discussed the contributions of bulk SOC and confinement, we now move on to the orbital mixing (OM) term which will mix the orbitals of similar spin but different

angular momentum, notably

$$\langle xy;\sigma \,|\, H_{om} \,|\, yz;\sigma\rangle = \quad 2ig\sin(k_x) \tag{3.25}$$

$$\langle xy;\sigma \,|\, H_{om} \,|\, xz;\sigma\rangle = \quad 2ig\sin(k_y) \tag{3.26}$$

where $\sigma = \uparrow, \downarrow$ and g is the magnitude of the OM. DFT and tight-binding calculations estimate this Rashba-like terms to be of the order of 5-10 meV which is also consistent with the experimentally determined value of around 10 meV [9]. These new coupling terms will have dramatic effects on the band structure. Firstly, as the inversion symmetry is broken, this will remove the degeneracy of the bands. And secondly, this results in a Rashba-like splitting of the bands as we saw in Eq. 3.4 and as we shall see later. The total Hamiltonian is now $H_{\text{surf/2DEG}} = H^c_{TB} + H_{SO} + H_{OM}$. In the basis $|d_\beta;\sigma\rangle$ ($\beta = (xy, yz, xz),\ \sigma = \uparrow, \downarrow$), $H_{\text{surf/2DEG}}$ reads

$$\begin{bmatrix}
\epsilon_{d_{xy}} & 2ig\sin k_x & 2ig\sin k_y & 0 & \lambda' & -i\lambda' \\
-2ig\sin k_x & \epsilon_{d_{yz}} & i\lambda' & -\lambda' & 0 & 0 \\
-2ig\sin k_y & -i\lambda' & \epsilon_{d_{xz}} & i\lambda' & 0 & 0 \\
0 & -\lambda' & -i\lambda' & \epsilon_{d_{xy}} & 2ig\sin k_x & 2ig\sin k_y \\
\lambda' & 0 & 0 & -2ig\sin k_x & \epsilon_{d_{yz}} & -i\lambda' \\
i\lambda' & 0 & 0 & -2ig\sin k_y & i\lambda' & \epsilon_{d_{xz}}
\end{bmatrix} \tag{3.27}$$

In fact, if solved numerically, the addition of this term to $H^c_{TB} + H_{SO}$ results in the splitting and the gapping of the cones. It is particularly important near E_F if the induced gaps lie close to E_F, i.e. the band crossings, where the OM becomes important, should lie close to E_F.

Excellent fitting of the ARPES energy dispersion curves is obtained with $a = 3.90$ Å, $t_1 = 0.388$ eV, $t_2 = 0.031$ eV, $\lambda = 0.025$ eV, $g = 0.02$ eV and $\epsilon_1 - V_0 = -0.205$ eV (1st d_{xy} band) and $g = 0.005$ eV and $\epsilon_1 - V_0 = -0.105$ eV (2nd d_{xy} band), $\epsilon_2 - V_0 = -0.0544$ eV for d_{yz}/d_{xz} bands as shown in Figure 3.5. With these parameters and no further adjustment, we overlay the tight-binding bands onto the momentum dispersion curves at E_F and obtain a very good agreement. DFT calculations on slabs with vacancies confirm the values of the bulk SOC and the Rashba SOC. Within the resolution of ARPES, one sees these crossing points [82, 83]. DFT calculations for slabs with vacancies also produce

dispersions suggestive of the 3 band crossing [84, 85]. A recent experimental report of the bands in LAO-STO [86] also shows two types of crossings but should remember that the resolution of the ARPES measurement in this heterostructure is less than that achieved at the STO (001) surface. Gating of the samples is also a simple way to tune the energies of the surface states in order to exhibit Γ_{dp} -type crossings. But this is only the Hamiltonian for $k > 0$; its time reversed partner is also present at $k < 0$ with the same energy and we shall use the same trick we did for the SOC and translate the time-reversed partner. Thus, if we revert back to the Hamiltonian given in Eq. 3.24, we shall begin to construct the OM terms in the SOC basis, and the matrix after the addition of the full OM is given by-

$$\begin{bmatrix} e_1 & 0 & 4ga_1(c_1\sin k_y - ib_1\sin k_x) & 2g(-i\alpha\sin k_x + \gamma\sin k_y) \\ 0 & e_2 & 2g(-i\alpha\sin k_x + \gamma\sin k_y) & 4ga_2(c_2\sin k_y - ib_2\sin k_x) \\ 4ga_1(c_1\sin k_y + ib_1\sin k_x) & 2g(i\alpha\sin k_x + \gamma\sin k_y) & e_1 & 0 \\ 2g(i\alpha\sin k_x + \gamma\sin k_y) & 4ga_2(c_2\sin k_y + ib_2\sin k_x) & 0 & e_2 \end{bmatrix} \tag{3.28}$$

where $\alpha = a_2b_1 + b_2a_1$, $\gamma = a_2c_1 + a_1c_2$. In fact, it can be shown that the OM term can be added adiabatically in two steps-

- one which removes the degeneracy of the cones (splits them) H_{om1} and
- another H_{om2} which gaps them at the crossing points created because of the splitting.

First step of OM

The first step can be written in the spin-orbit coupled basis as a coupling element between the degenerate energy bands. These coupling elements can be evaluated to give the terms $R_1 = 4ga_1(-i\sin(k_x)b_1 + \sin(k_y)c_1)$ in the first subspace comprising B and B* and $R_2 = 4ga_2(-i\sin(k_x)b_2 + \sin(k_y)c_2)$ in the second subspace C and C*. The matrix after the first step of OM takes the following form in the basis of $|B\rangle, |B^*\rangle, |C\rangle, |C^*\rangle$-

$$\begin{bmatrix} E_b & R_1 & 0 & 0 \\ R_1^* & E_b & 0 & 0 \\ 0 & 0 & E_c & R_2 \\ 0 & 0 & R_2^* & E_c \end{bmatrix} \tag{3.29}$$

Adding these terms brings about a Rashba-like split to the bands as will be shown later. The addition of these terms also comes with a phase being added as will be seen in the form of the eigenvectors. On applying degenerate perturbation theory on each of the block,

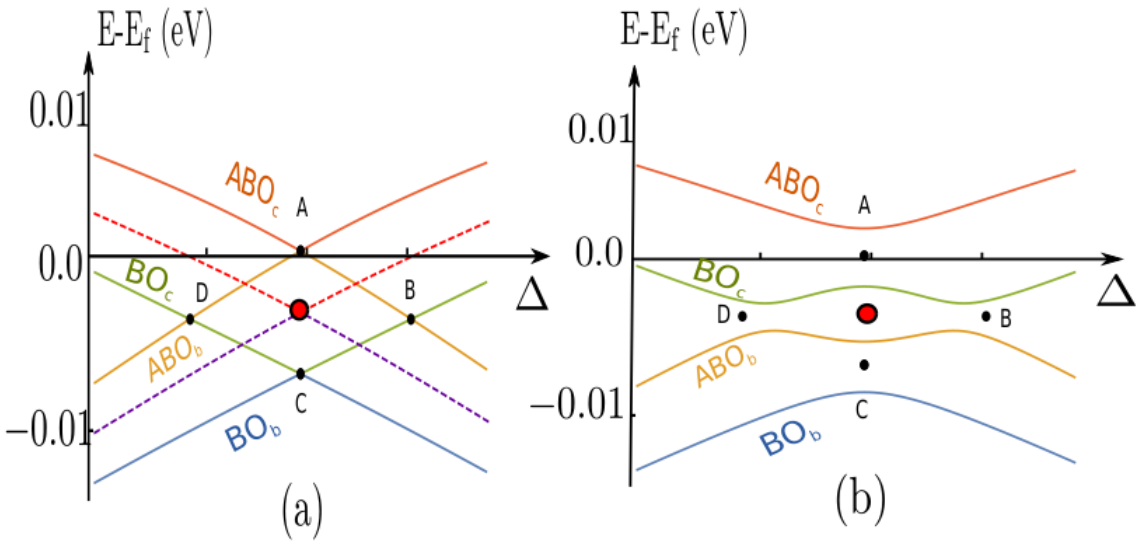

Figure 3.8: Evolution of the Dirac cones in the Δ direction after the addition of step 1 (a) and then step 2 (b) of OM. The original Dirac cone, seen as dotted lines splits and then is gapped at the crossing points A,B,C and D to have an inverted and gapped spectrum. Adapted from [79].

we shall get the eigenvalues for the first block spanned by the $|B\rangle$ and $|B^*\rangle$ as

$$E_{\pm} = E_b \pm |R_1| \tag{3.30}$$

for the second block spanned by the $|C\rangle$ and $|C^*\rangle$, it will be

$$E_{\pm} = E_c \pm |R_2| \tag{3.31}$$

This results in the bands splitting into bonding and anti-bonding orbitals, denoted by B.O. and A.B.O. for each of the blocks. For the first matrix spanned by subspace (B) consisting of $|B\rangle$, $|B^*\rangle$, the eigenvectors are given by -

$$|BO_B\rangle = \frac{ie^{-i\psi_1}}{\sqrt{2}}|B\rangle + \frac{1}{\sqrt{2}}|B^*\rangle \tag{3.32}$$

$$|ABO_B\rangle = \frac{-ie^{i\psi_1}}{\sqrt{2}}|B^*\rangle - \frac{1}{\sqrt{2}}|B\rangle \tag{3.33}$$

Similarly we shall have bonding and anti-bonding orbitals of the same character for the subspace spanned by $|C\rangle, |C^*\rangle$.

$$|BO_C\rangle = \frac{ie^{-i\psi_2}}{\sqrt{2}}|C\rangle + \frac{1}{\sqrt{2}}|C^*\rangle \tag{3.34}$$

$$|ABO_C\rangle = \frac{-ie^{i\psi_2}}{\sqrt{2}}|C^*\rangle - \frac{1}{\sqrt{2}}|C\rangle \tag{3.35}$$

In fact, the eigenvectors are a linear combination of the unperturbed basis orbitals with an additional phase, exactly as in the case of the Rashba Hamiltonian. The phase appearing in the eigenvectors of Eqs. 7.4-7.7 $\tan(\psi_1) = \frac{c_1 \sin(k_y)}{b_1 \sin(k_x)}$ and $\tan(\psi_2) = \frac{c_2 \sin(k_y)}{b_2 \sin(k_x)}$. This phase gives us the spin texture which can be represented by a vector having two components x and y for a given ψ_1-

$$x = -2g\frac{a_1 c_1 \sin(k_y)}{\sqrt{2}|R_1|} \tag{3.36}$$

$$y = 2g\frac{a_1 b_1 \sin(k_x)}{\sqrt{2}|R_1|} \tag{3.37}$$

Both the R_i terms depend on the coefficient of the a_i, i.e. the coefficients of d_{xy} orbital in each of the blocks. For the ΓM direction, as the d_{xy} coefficient is zero, no splitting of the cones is observed. It is to be noted that there are branch cuts which lie in the ΓM and the $\Gamma M^{'}$ directions for the eigenvectors before the addition of the OM term respectively, will also be reflected in the phase $\psi_{1,2}$, which depends on a_i, b_i, c_i (See Appendix A). We first, diagonalise the matrices that we have obtained in Eq. 7.3 and thus we end up with a Hamiltonian has the following form in the basis formed by the eigenvectors that we had

found earlier in Eqs. 7.4-7.7 :

$$\begin{bmatrix} E_b - \sqrt{R_1 R_1^*} & & 0 & 0 \\ 0 & E_b + \sqrt{R_1 R_1^*} & 0 & 0 \\ 0 & 0 & E_c - \sqrt{R_2 R_2^*} & \\ 0 & 0 & & E_c + \sqrt{R_2 R_2^*} \end{bmatrix} \tag{3.38}$$

Here, we see that the bands are going to cross as they have been shifted from their original energy values of E_b and E_c and there will be a band inversion for the anti-bonding branch of the lower cone and the bonding branch of the higher cone. This leads to bands crossing at two points B and D (seen in Figure 3.8) and the particularity of these points is that they will have parities which are the opposite of each other. This can be seen in the phase of the eigenvectors and in the nature of the eigenvectors which compose B and D. These matrices spanned by subspaces (B), formed by $|B\rangle, |B^*\rangle$ and (C), formed by $|C\rangle, |C^*\rangle$, will have the standard form of the Rashba matrix once we expand around any of the Dirac Points (DP) where $k = k_c$. The terms R_i which are sine functions and can be expanded up to the first order to give linear terms in k. And thus, $R_i \propto ik_x^{'} + k_y^{'}$ produce the standard form of the Rashba eigenvectors.

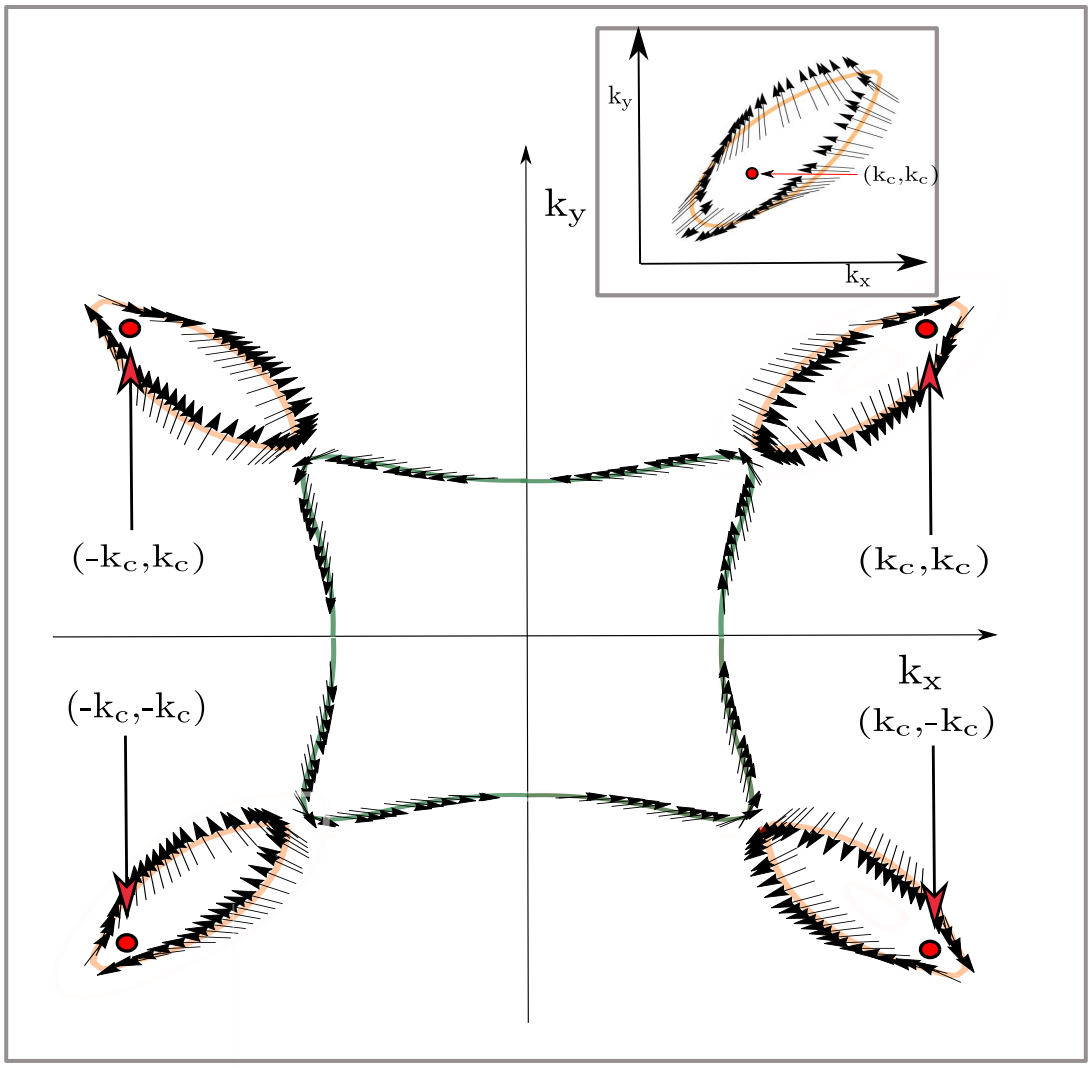

Figure 3.9: The phase winding ψ in the BZ for the four DPs for an energy contour above that of point A after the first step of the OM can be seen here. The central sheet is centred at Γ and ψ changes by 2π around the contour. Four oval shaped sheets enclose the Dirac points and ψ winds by $-\pi$ around each of the contours. Adapted from [79].

The phase winding ψ after the first step of OM can be seen on a constant energy contour for a cut above (below) the point A (at C) in Figure 3.9 where all four DP are represented. There are two sets of contours - one which is centred at Γ and four, oval shaped, contours which surround the DP. ψ is calculated around one DP in the first quadrant. For the contour above A, a branch cut extending from Γ_{dp} to M is observed. Below point C a branch cut extending from Γ_{dp} to Γ is obtained. It is to be noted that the branch cut is not along the

same direction for bands with energies above and below DP, the integral of the Berry phase along all the bands at a fixed value of k still remains zero due to the contribution from the rest of the bands. It is to be noted that both the cones and the singularities in ψ evolve as the symmetry operation C_4 rotation is applied. Two time reversed cones have an additional shift of π between them for the singularity. Below the DP, the energy contours have phase windings in the opposite direction to that above Γ_{dp}, which is expected. In between the points A and D, the phase also winds as expected along the energy cuts made in this region. Now we are ready to add the second step of the orbital mixing in this basis of ABO and BO orbitals.

Second step of OM

For the second step of OM, we shall do well to remember that the following coupling elements are zero by construction.

- $\langle B \,|\, H_{om2} \,|\, C \rangle = 0$
- $\langle B^* \,|\, H_{om2} \,|\, C^* \rangle = 0$

From the form of the eigenvectors, $\psi_1 = -\psi_2$. Thus, we obtain the following coupling elements between the bonding orbital of one branch and the anti-bonding orbital of another.

- Bonding orbital $\langle \mathrm{B}_B \,|\, H_{om2} \,|\, \mathrm{B}_C \rangle : 2g\alpha e^{i\psi_1} \sin(k_x)$
- Anti-Bonding orbital $\langle \mathrm{AB}_B \,|\, H_{om2} \,|\, \mathrm{AB}_C \rangle : 2ig\gamma e^{-i\psi_1} \sin(k_y)$

and the bonding and anti-bonding orbitals of the same energy branch ($|BO_i\rangle$ and $|ABO_i\rangle$) have no coupling element between them. This is also obvious from the Figure 3.8 where it is clearly seen that the bonding orbitals do not interact with its anti-bonding counterpart.

And we can write down the matrix in the basis of $\langle B_B\rangle, \langle AB_C\rangle, \langle B_C\rangle$ and $\langle AB_B\rangle$ as

$$\begin{array}{c} \\ B_B \\ AB_C \\ B_C \\ AB_B \end{array} \begin{array}{c} \begin{array}{cccc} B_B & AB_C & B_C & AB_B \end{array} \\ \begin{pmatrix} e_1 - |R_1| & 2g\gamma \sin k_y & 2ge^{i\psi_1}\alpha \sin k_x & 0 \\ 2g\gamma \sin k_y & e_2 + |R_2| & 0 & -2ge^{i\psi_1}\alpha \sin k_x \\ 2ge^{-i\psi_1}\alpha \sin k_x & 0 & e_2 - |R_2| & 2g\gamma \sin k_y \\ 0 & -2ge^{-i\psi_1}\alpha \sin k_x & 2g\gamma \sin k_y & e_1 + |R_1| \end{pmatrix} \end{array} \tag{3.39}$$

This creates gaps at the crossing points and renormalises the phase that we had gotten earlier which can be seen in the Appendix A as we apply perturbation theory to this four band model. As we can see in the figure, there are two bands which show signatures of band inversion which we shall be concerned with in the next section. We shall use these two bands and construct a simple variational model with two bands to be able to explore the edge states.

3.6 1D Topological surface states at the 2D surface of $SrTiO_3$

In order to be able to probe the existence of edge states, we need to map the four band Hamiltonian that we had obtained in the previous section, to a much simpler and better understood model. This will be the parabolic one with the breaking of the particle hole symmetry, giving inverted bands with gap openings. This model is justified because we investigate the spectrum close to the DP, which is the new effective Γ point and in its vicinity, the bands can be assumed to be parabolic. For all practical purposes, the k momentum that we shall write down will be the renormalised $k \equiv k - k_c$ as the expansion is made around the DP. In order to map the model to a simplified version, we shall try to make it of the form of the Bernevig, Hughes and Zhang (BHZ) model [42] with some modifications.

Our Dirac cones have a tilt which changes as we move around Γ_{dp}. This tilt term however, is just a diagonal term which does not impact the nature of the eigenvectors or the band inversion. The tilt, given by $(E^c_{d_{xy}} + E^c_{d_{yz}} + E^c_{d_{xz}})/3$, where the energies E^c

have been defined in Eqs. 3.13, can be expanded in the vicinity of Γ_{dp} to give $d_0(k)\mathbf{1} = (d_x k_x^2 + d_y k_y^2)\mathbf{1}$. It has been absorbed in the particle-hole-asymmetry term $\epsilon(k)$. α and γ represent the anisotropy of the Rashba interaction and are themselves functions of k, which incorporate the branch cuts of the eigenvectors and the associated singularity of the Berry phase. We take explicitly into account the particle-hole asymmetry, described by the parameters D_x and D_y into which we have also absorbed the tilt term $d_0(k)$. The Hamiltonian is

$$\begin{bmatrix} M - (D_x + B_x)k_x^2 - (D_y + B_y)k_y^2 & i\alpha k_x - \gamma k_y \\ -i\alpha k_x - \gamma k_y & -M + (-D_x + B_x)k_x^2 + (-D_y + B_y)k_y^2 \end{bmatrix} \tag{3.40}$$

In this section, we are interested only in the topological properties of the systems which give rise to the particular edge-state structure. Since these topological properties are not affected by the particle-hole asymmetry, which yields a term proportional to the unit matrix, we set $D_x = D_y = 0$ in the following discussion of the edge states. It can be shown that $D_x \neq D_y$ does not bring about a qualitative change in the nature of the edge states. The model is solved in a finite strip geometry of width L with periodic (open) boundary conditions in the *x* (*y*) direction. Here k_x is still a good quantum number while k_y is replaced by $k_y = -i\frac{\partial}{\partial y}$. The wave function is of a mixed real and k-space function of the form of $\phi(k_x, y) = \phi(k_x)e^{-\lambda y}$. With this form, we derive the secular equation to get four eigenvalues.

$$\lambda_{\pm}^2 = \frac{B_x}{B_y}k_x^2 + \frac{\gamma^2}{2B_y^2} - \frac{M}{B_y} \pm \sqrt{\left(\frac{\gamma^2}{2B_y^2} - \frac{M}{B_y}\right)^2 + \frac{E^2 - M^2}{B_y^2} + \frac{k_x^2}{B_y^2}\left(\frac{B_x}{B_y}\gamma^2 - \alpha^2\right)} \tag{3.41}$$

The boundary conditions at the limits impose that the solutions of this equation become zero at $y = 0$, i.e, in the middle of the slab, and go to zero as $y \to \pm\infty$. The solutions are

then of the form, for $y > 0$

$$|\phi_B\rangle = \begin{bmatrix} a \\ b \end{bmatrix} (e^{-\lambda_+ y} - e^{-\lambda_- y}), \tag{3.42}$$

and similarly for $y < 0$. The condition of existence of such states implies that the real parts $\mathbb{R}(\lambda_+)$ and $\mathbb{R}(\lambda_-)$ should be of the same sign (so as to avoid any solution which does not decay at $\pm\infty$). The symbol $\mathbb{R}$ denotes the real part. Under this condition, the equation $H|\phi_B\rangle = E|\phi_B\rangle$ gives us

$$\frac{a}{b} = \frac{M - E - (B_x k_x^2 - B_y \lambda_+^2)}{-i(\alpha k_x + \gamma \lambda_+)} = \frac{M - E - (B_x k_x^2 - B_y \lambda_-^2)}{-i(\alpha k_x + \gamma \lambda_-)}, \tag{3.43}$$

i.e.

$$E = M - B_x k_x^2 + \frac{\alpha}{\gamma} B_y k_x (\lambda_- + \lambda_+) - \lambda_+ \lambda_- B_y, \tag{3.44}$$

and we see immediately that if we are to get an edge state, we should have the energy $E = 0$ at $k_x = 0$, i.e., the gap is closed at $k_x = 0$. For the condition $k_x = 0$, we have

$$\sqrt{M - E} = \text{sign}(B_y)\sqrt{M + E}, \tag{3.45}$$

which has a solution $E = 0$ for $MB_y > 0$, i.e., M and B_y should have the same sign, which is the case if we have a band inversion. We also verify that in this case, we shall have $\mathbb{R}(\lambda_+)\mathbb{R}(\lambda_-) > 0$ and thus $\mathbb{R}(\lambda_+)$ and $\mathbb{R}(\lambda_-)$ have the same sign which entails $0 < M/B_y < 1/4$. This signifies that we have a linearly dispersing edge state (up to first order in Eq. 3.44) which will cross $k_x = 0$ which is the effective $k_x \equiv k_x - k_c$.

It is this linear edge state which will carry a spin polarised current on the edges (taken with a pinch of salt as we have mixed spin-orbital t_{2g} states). Now the experimental detection of this edge polarised current, which we shall see in future sections, might be slightly more involved as we also have a 2DEG state which might drown out all topological signatures.

3.7 Study of the $(0\,0\,1)$ oriented surface of $LaAlO_3/SrTiO_3$

3.7.1 Experimental results and theoretical modelling

Similar to the STO $(0\,0\,1)$ surface, the hetero-structure of $LaAlO_3$ deposited over a STO substrate in the $(0\,0\,1)$ orientation, also has a confined 2DEG at the interface on the STO side [7, 8]. In fact, it was the discovery of this metallic state at the $LaAlO_3/SrTiO_3$ (LAO/STO) interface of two wide band insulators, in 2004 by Ohtomo and Hwang, which spurred the research for unexpected metallic oxide interfaces/surfaces. The origin of the gas is a matter of great debate, with some ascribing it to an intrinsic polar catastrophe scenario, which causes band bending, while others to an extrinsic oxygen vacancy scenario, which causes n-type doping or a cation intermixing scenario among others.

The intrinsic scenario or the polar catastrophe invokes the polarity of LAO which has charged LaO and AlO_2 planes in the $(0\,0\,1)$ direction, carrying a charge of +1 and -1 respectively. In contrast, the STO substrate consists of neutral SrO and TiO_2 planes and this difference of polarity will play an important role. The charging of the LaO and AlO_2 planes is akin to a parallel plate capacitor in series and results in an electric field which causes band bending and ultimately causing a transfer of electrons from the valence band of the topmost surface of AlO_2 layer to the TiO_2 layer at the substrate, compensating for the difference in polarity of the two materials. For an infinitely thick LAO, this leads to the formation of the gas at the interface with a carrier density of half an electron per unit cell (roughly 3.3×10^{14}cm^{-2}). But in reality, we can only have finite numbers of planes of LAO and thus, only a carrier concentration density up to $10^{13} - 10^{14}$ cm^{-2} is observed in transport measurements and in ARPES for slabs up to 15 unit cells (u.c.). After that limit, a breakdown of the materials occurs and the conductance starts decreasing. According to the polar catastrophe scenario, the conductance of the gas should increase for increasing thickness of the LAO layers as the charge transfer increases. However, in practice, this is not observed. A clear Insulator to Metal transition is observed as the thickness of LAO is increased from 3 to 4 u.c. but as the LAO thickness is increased further, the conductance remains constant and then starts decreasing as the materials' breakdown limit is reached

as can be seen in Figure 3.10. Nonetheless, the polarity of LAO undoubtedly contributes to the formation of the 2DEG. In the extrinsic scenario, explored in ab-initio studies [87,

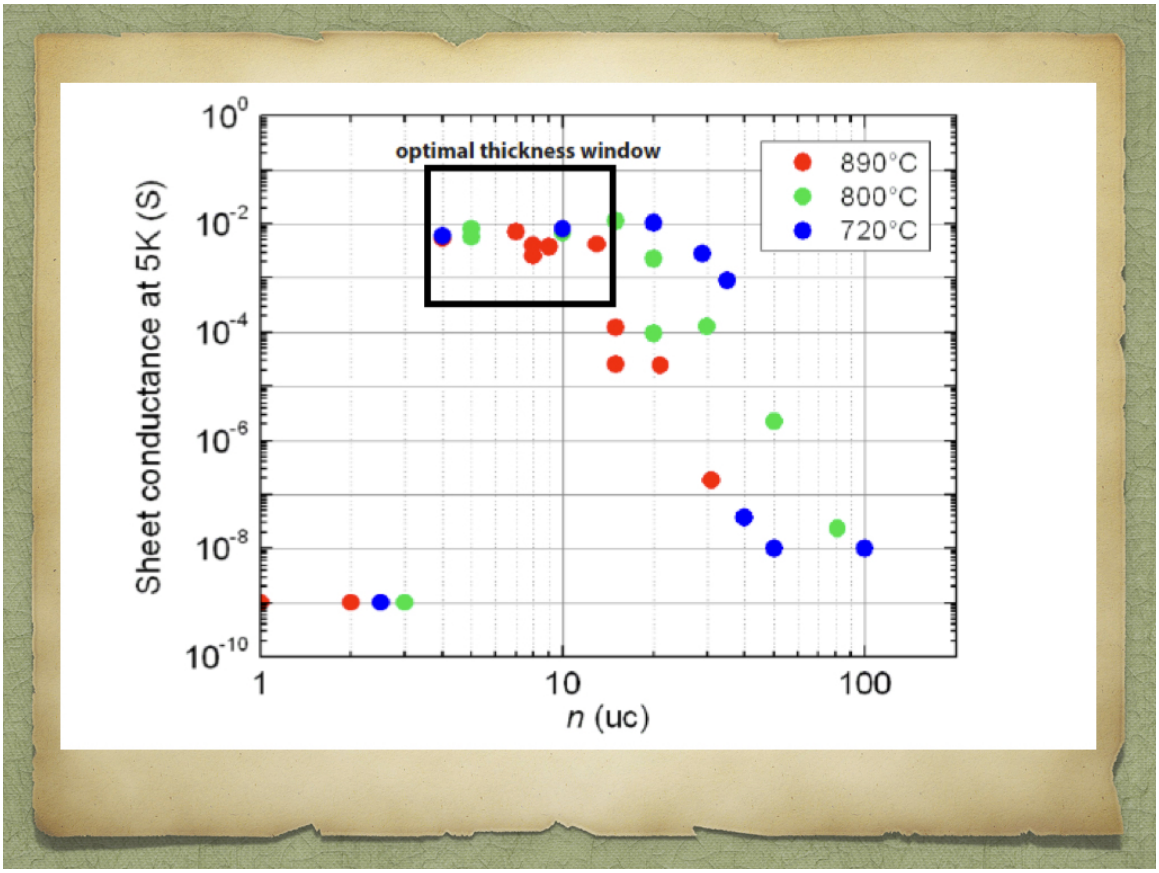

Figure 3.10: The optimal thickness of LAO/STO is shown in this figure. For layers above 10 u.c., there is a breakdown as the conductance keeps on decreasing. Adapted from [75].

88], the oxygen vacancies at the top surface of the LAO give rise to the extra electrons with each vacancy providing two electrons. These electrons might get localised close to the vacancies due to the attractive potential but can also delocalise to form the gas. Energetically speaking, when the energy cost of the creation of an oxygen vacancy is compensated by the reduction of the electric field generated by the polar LAO, then it becomes favourable to create a vacancy. This is achieved at 4 u.c. of LAO and the electrons, released by the vacancies created at the top surface, are swept down to the interface by the electric field present in LAO [89]. On increasing the number of the u.c of LAO, the conductance remains the same as the energy threshold has been crossed for the formation of vacancies. It could be argued that the vacancies could be present anywhere in the LAO layers, however,

it cannot be denied that is more favourable to do so at the topmost surface, where there are less bonds to break and the potential energy gain, for the electrons going towards the interface, is maximum. Reports like Ref. [90] seem to suggest that it is a mixture of both scenarios which explains the formation of the 2DEG. In fact, no matter what the origin of the compensation of the formation energy of a vacancy is, once it becomes favourable to create a vacancy, it will be formed. In LAO, the polar field compensating for the formation energy of vacancies could just be a happy coincidence. For a detailed discussion, the reader is advised to refer to [16, 91]. It is to be noted that this debate arises mostly in LAO/STO because there is a possibility for the two mechanisms to co-exist. This does not even arise on the bare surface of STO where only the oxygen vacancies can play a significant role.

If experiments are now discussed with respect to ARPES and transport, the overall electronic structure near E_F of both LAO/STO and STO is remarkably similar. In ARPES, LAO/STO has filled conduction bands with a large intensity for the d_{yz} bands and traces of two sub-bands of dominant d_{xy} are seen [92]. Using the ARPES data, the effective masses can be estimated - for LAO/STO (STO) they are 0.7 m_e(0.7 m_e) for the light and 14 m_e (10-20 m_e) for the heavy bands. [8, 70, 93]. The Fermi surface (FS) consists of two concentric circles of dominant d_{xy} bands and two lobes of the dominant $d_{xz/yz}$ orbitals, seen in Figure 3.11, similar to what is observed for the STO surface. Although in the two compounds, the FS, the type of conduction bands seen and the effective masses have remarkably similar features, the resolution of both the band dispersion and the FS in LAO/STO $(0\,0\,1)$, is much lower than in the case of STO $(0\,0\,1)$. This is due to the 2DEG being buried under multiple LAO layers which makes measurements by ARPES difficult. If the RIXS spectra of LAO/STO and STO are compared, by tuning it to resonate with the Ti^{3+} transitions, similar features are found. There are similar inter and intra t_{2g} transitions as well as a peak corresponding to delocalised electrons and even an in-gap state. The enhancement of such a metallic state is also seen under irradiation which is exactly the case for STO. Even at 2 u.c. of LAO deposited on LAO, there is a precursor for metallicity in the system; as the sample is illuminated in ultrahigh vacuum, a Fermi surface and some band dispersion appear [94].

Despite these striking similarities, there are also a few differences among the two com-

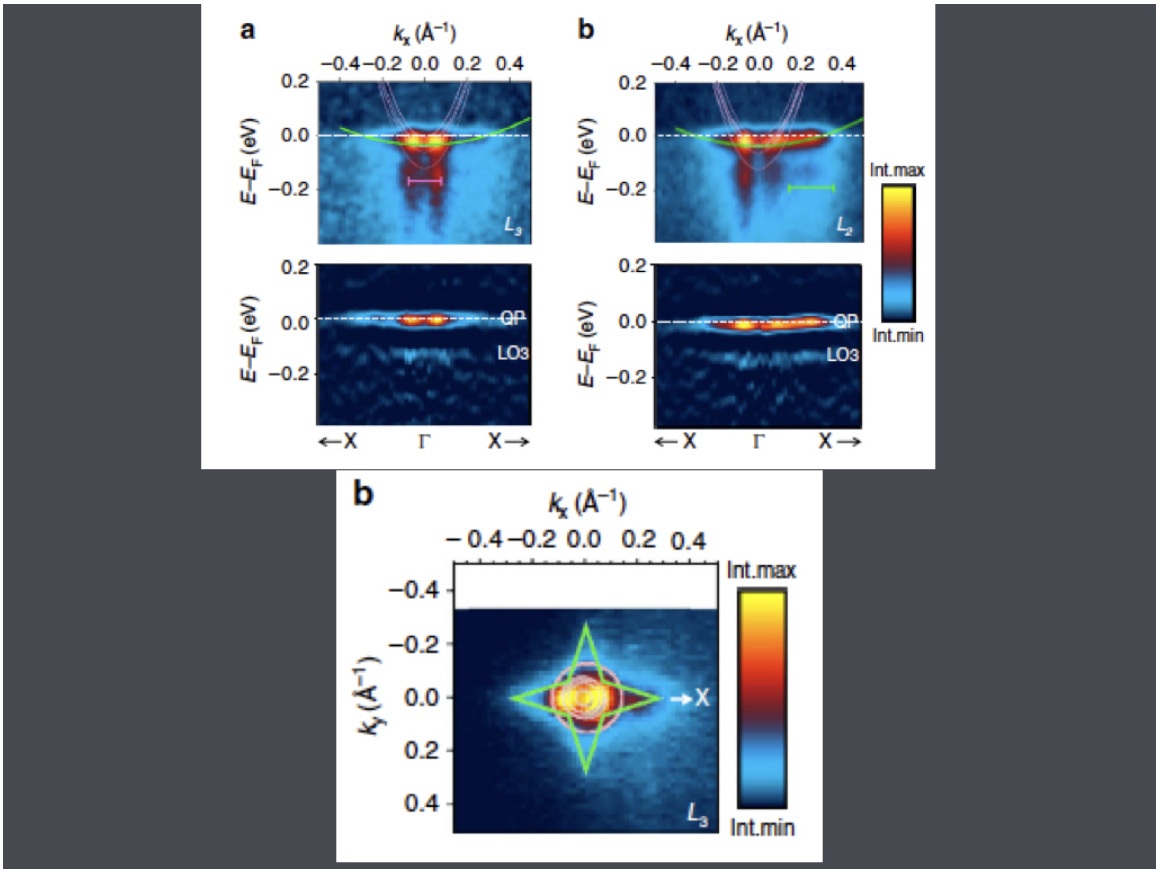

Figure 3.11: The band dispersions for $k_y = 0$ and FS maps for LAO/STO $(0\,0\,1)$ are shown here. Two light dispersive bands are seen for the FS maps and a heavy band is seen for the band dispersion plots. They are remarkably similar to STO $(0\,0\,1)$ despite the poor experimental resolution due to the buried gas. Adapted from [92].

pounds, notably that of confinement of the gas. In the case of LAO/STO, the extensions of the gas at the STO side of the interface, is up to 1-3 u.c. [90] while for STO (001), the gas spans up to at least 4 u.c [8, 70]. Thus, there is a clear indication that the gas is more confined in the case of LAO/STO as compared to STO (a factor that could be as large as 3). This could in part be explained by the polarity of LAO which increases the confining potential and keeps the gas close to the surface but could also depend on the locations of oxygen vacancies formed from those formed at the top surface of LAO as compared to those at the surface of STO.

What LAO/STO lacks in direct band measurements like ARPES, it makes up in transport data as a plethora of results detail the Hall conductivity, the superconducting transition

and even ferromagnetism [95, 96]. The transport is not as easy to perform in STO except when the surface is capped by Al or AlO_2 in liquid gating or in tunnelling experiments [97]. The available data for ARPES and transport, suggests that the two systems have a lot of features in common. Based on the ARPES data, the tight-binding modelling for STO $(0\,0\,1)$ and LAO/STO $(0\,0\,1)$, is essentially the same with a slight modification of the hopping parameters. If a similar analysis like that for STO $(0\,0\,1)$ is done, then similar tight-binding modelling will emerge. What is even more interesting is that similar spin-textures and topological edge states will also emerge, making LAO/STO $(0\,0\,1)$ topological. The band structures along with the spin textures can be seen in Appendix B. For the experimental detection of the edge states generated in either STO or LAO/STO might be more involved as we also have a 2DEG state which might drown out all topological signatures.

3.8 Experimental detection of the 1D topological edge states

The topological edge states that we are predicting at the 1D boundary of the sample might not be easy to detect experimentally as they could be masked by the conducting sheet which is the case both in ARPES and in transport. In ARPES, the energy resolution is not enough to evidence the edge states which are in a 4meV gap below the E_F. Even if the E_F is tuned by a gate voltage, for the signature to be measured in transport, the conducting background in the form of other filled sub-bands in the conduction band manifold could drown the edge states out.

One way around this difficulty is to couple the 2DEG to conventional s-wave superconductors. This induces superconductivity by proximity in the 2DEG and opens up a gap and the edge states might be easily decoupled from the conducting background. Josephson junctions formed between the s-wave sc and the topological materials could then show signs of a doubling of phase in the Andreev bound states as now the edge states are involved rather than the Cooper pairs tunnelling between the two superconducting contacts. This also leads to a doubling of the Shapiro steps and an emission at half the Josephson frequency instead of the full Josephson frequency.

This stategy has been successfully implemented for HgTe/CdTe heterostructures which

are known to possess 1D topological edge states. Experiments carried out on HgTe/CdTe quantum wells measured the Josephson radiation from gapless Andreev Bound states [98]. In out-of-equilibrium situations, missing Shapiro steps and emission at half of the Josephson frequency are predicted [99] and they were experimentally measured [100] as the quantum well is driven to the topological regime with gapless edge states. These are consequences of p-wave superconductivity being induced in the 2D topological insulator's edge channels when it's Josephson coupled to nearby conventional s-wave superconductors. A doublet of p-wave Andreev bound states arises and has an energy dispersion which is 4π periodic in the Josephson phase. We suggest a similar Josephson junction setup for STO where the latter is sandwiched between two superconductors. The topological regime can be observed by gating the sample and tuning the Fermi energy to that of the edge states. A similar change in the frequency emitted should be observed. Optimizing the carrier concentration and the width of the STO junction to reduce the number of parallel channels would allow one to evidence the topological states.

Topological superconductivity, thus induced, can be detected experimentally as it will form a Majorana fermion at the boundary between the s-wave superconductor and the topological material. Majorana detection could be done in tunnelling spectroscopy if a 1D wire with Majorana edge states can be formed, as is the case of Bi nanowires [101] where a zero bias conductance peak is observed in tunnelling. If the width of STO can also be constrained to that of a nanowire, then possible Majorana states can also show this zero bias peak. Topological superconductivity in its theory and detection is not the object of this dissertion and the interested reader can consult two excellent PhD thesis among many on this subject [101, 102].

There is another very significant challenge when it comes to the topology-that of magnetism. The report of magnetism at the surface of STO raises the issue of the stability of the topological state to time reversal symmetry breaking but from an experimental standpoint, the claim of magnetism is still debatable [103, 72, 104, 105]. If a purported ferromagnetic exchange splitting affected the t_{2g} carriers, that would be detrimental to the edge states. The DFT study of M. Altmeyer [106] reveals a dichotomy between localized magnetic moments of e_g orbitals and spin textures for the t_{2g} conduction states. This orbital dichotomy

might be a way out - even if spin-polarized domains were present, one might nevertheless retain some of the topological character if the state of the 2DEG at the surface were spatially inhomogeneous. According to experimental reports in STO [105] and in LAO/STO [107, 108, 109], polarized domains coexist with patches of metallic regions. If the latter percolated across the entire surface of STO, the electronic bands of the 2DEG could still present a parity inversion leading to topological 1D edge states at the boundary. Thus, spatial inhomogenity and spatial dichotomy might still save topology. This issue of magnetism will be delved into even deeper as we will perform an in-depth DFT study of $CaTiO_3$ which also has a 2DEG and could possibly host magnetic states.

Chapter 4

$SrTiO_3$ and $LaAlO_3$/$SrTiO_3$ at their $(1\,1\,1)$ oriented surfaces

4.1 Introduction

Not everything that can be counted counts, and not everything that counts can be counted.

Albert Einstein

A lot has been said about the $(0\,0\,1)$ orientation in the previous chapter, be it regarding band structure or topology. We will now turn our attention to the $(1\,1\,1)$ orientation to see if interesting physics can also emerge in these systems. We shall principally be studying the LAO/STO and the STO system, both of which, contain a metallic surface state. Firstly, ARPES measurements for the STO shall be discussed from which a tight binding modelling will be inferred. This modelling will be the same as that for LAO/STO as little direct band measurements have been done for it. But what LAO/STO lacks in ARPES data, it more than makes up for in transport. We will see the unique features present in LAO/STO as the electrostatic doping is increased - multi band non linear Hall transport and superconductivity will emerge. This non linearity shall be explained in terms of correlations which will result in band inversions and in band crossings. It is the latter which will then be scrutinised for possible topological features, one of them arising because of the particular choice of the surface and another arising from the band crossings.

4.2 Experimental data for $(1\,1\,1)$ surface of $LaAlO_3/SrTiO_3$

For the $(1\,1\,1)$ case, there is very little data for a direct band measurement for LAO/STO but there exists a variety of results for its cousin STO, which also has a 2DEG at the $(1\,1\,1)$ surface. In STO, there is very little confinement for the $(1\,1\,1)$ case as compared to the $(0\,0\,1)$ case as the gas spreads over 15-25 Ti layers [110] (or 9 Ti layers as reported by Santander et al [103]). This can also be seen in the band dispersion where, within experimental resolution, the bands are degenerate at Γ and there is no hierarchy of the bands due to confinement as is the case in the $(0\,0\,1)$ orientation. From the band dispersion observed in ARPES two effective masses with the values 0.33 m_e and 8 m_e respectively

can be derived [103]. In the $(1\,1\,1)$ orientation, the Fermi Surface (FS) consists of three ellipses consistent with the hexagonal symmetry and the fact that the t_{2g} orbitals all have equal contribution to the FS again showing very little impact of confinement on the orbital order. It is to be noted that the $(1\,1\,1)$ interface in STO is polar and hence the confinement of the gas should theoretically, be even greater. But as observations point out, it is the other way around. This is due to the lack of stability for a polar interface and in order to account for this instability, the surface might try to adjust to neutralize itself. There could be octahedral rotations and tiltings at the surface, which would move the oxygen atoms and try to cancel out the dipole moments created because of the polarity. There could also exist a mixed termination scenario where an intermixing of both SrO and TiO_2 termination could exist. It is even possible that oxygen vacancies might occur similar to the case of $(0\,0\,1)$, which would again cause the polarity to be reduced. Regardless of the origin, the surface compensates for the polarity and becomes neutral.

Since very little data exists for LAO/STO $(1\,1\,1)$ in ARPES, we shall use the insights we get from STO $(1\,1\,1)$, including the weak confinement as seen by the orbital dispersion and the effective masses obtained from fitting the bands seen. However, LAO/STO $(1\,1\,1)$ has transport data to make up for the missing direct band dispersion. Monteiro et al [1] on analysing the Hall data for LAO/STO $(1\,1\,1)$ found that on increasing the carrier concentration via gating, superconductivity and multiple band transport was observed. Field effect measurements in a back-gate configuration reveal a transition from linear to non-linear Hall curves with increasing electrostatic doping, which is a well established experimental signature of a transition from single-carrier to two-carrier transport as seen in Figure 4.1.

This single to two carrier transport is not a surprising result in itself as it has been reported also for the $(0\,0\,1)$ termination [111, 112, 113]. Smink et al [93] report that for increasing carrier concentration, in a top gate Hall measurement, the carrier density of one of the conducting bands decreases at the expense of another. This can be understood in terms of the band structure consisting of t_{2g} orbitals affected by confinement. This results in an orbital re-ordering with the d_{xy} orbital being much lower than the $d_{xz/yz}$, which was

[1] A.M. Monteiro, M. Vivek et al., Band inversion driven by electronic correlations at the (1 1 1) LaAlO3/SrTiO3 interface, submitted to Phys. Rev. Lett., currently under review.

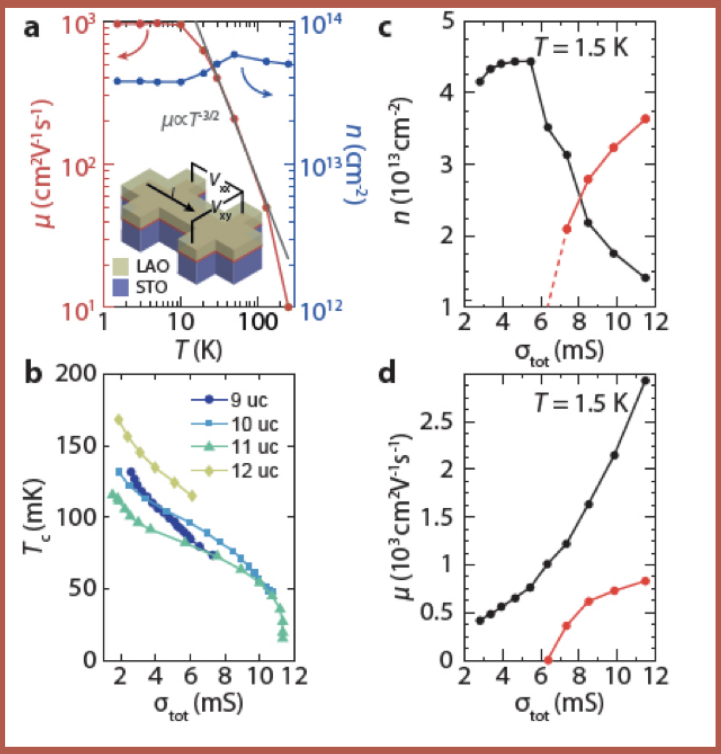

Figure 4.1: Experimental curves as reported by M. Monteiro et al show that the carriers of one band increase at the expense of the other (c) and that the mobilities of both bands increase (d). Adapted from Ref [2].

also explicited in the case of STO $(0\,0\,1)$ in Chapter 3. The d_{xy} dominant bands are the first to get populated and have lower mobilities as they are closer to the interface and hence more affected by disorder. Assuming a rigid band model, the next bands to get populated should be the heavy and more mobile $d_{xz/yz}$ bands as the population of d_{xy} continues to increase. However, as the gating is tuned and more and more carriers introduced in the system, the $d_{xz/yz}$ bands increase in population while a *decrease* in the carrier concentration of the d_{xy} bands is seen. An explanation of this multi-band transport, based on Hubbard type correlations and a non rigid band model based on Poisson-Schrödinger(PS) calculations, has been proposed [93]. This behaviour is also seen in back gate transport experiments wherein as bands with increasing mobility get populated as the gating increases and the Lifshitz point is crossed (A Lifshitz point is the anti-crossing between the light d_{xy} and the

heavy $d_{xz/yz}$). For a discussion between the similarities and the differences between a back and a top gate, the reader is advised to refer to [114].

In the $(1\,1\,1)$ orientation, no Lifshitz point should exist as the orbitals are degenerate at Γ and all bands should be occupied equally. However, in a back gate Hall measurement, the population of a second band increases at the *expense of the other* even as the mobility of the second band is much lower. Firstly, this preferential filling of the bands even as the all orbitals are degenerate is surprising and secondly, this order of mobilities is also the inverse of what is seen in the $(0\,0\,1)$ orientation. A possible explanation could be two electron-like bands which are affected by correlations as more and more carriers are added. This correlation theory shall be explored in great detail in the theoretical modelling. While the signature of a one to multi-band transport is clear, there is still a debate over the nature of the carriers in the $(1\,1\,1)$ terminated LAO/STO. M. Monteiro et al seem to suggest that the two bands are electron like, reasoning on the basis of the negative slope of the Hall curves at low fields, while Rout et al [115] seem to suggest one hole and one electron like band. The Hall data, nevertheless, gives us strong hints that the nature of the carriers will be only electron-like as seen in Ref. [2].

Apart from multiple band transport, a superconducting dome is also observed with a non monotonic decrease in T_c with the increase in electrostatic doping in Ref. 2 [115].

The chapter shall be organised in the following way - to understand the role of electronic correlations, we shall make a tight-binding analysis using PS calculations. We shall begin with the bulk modelling and move on to the surface and finally add the correlations in the form of the Hubbard *U*. We shall see some interesting band inversions coming into play as the correlations are added. Next, we shall try to correlate the increasing carrier concentration as a function of the fermi energy to a function of gate voltage. In the end, we shall look carefully at the band inversions to see if some topological features will emerge like those which are present in KTO $(1\,1\,1)$, where parity inversion and bulk-spin orbit coupling act together to give topological edge states.

4.3 Theoretical modelling : kinetic, spin-orbit, trigonal field, confinement and correlations

4.3.1 Kinetic terms - Inter and intra-layer hopping

The conduction bands of LAO/STO $(1\,1\,1)$ are still of majority Ti t_{2g} character and the valence bands of dominant O p character. However, as the orientation has changed from $(0\,0\,1)$ to $(1\,1\,1)$, the Hamiltonian features very different terms. As it will be shown, the different terms - kinetic, bulk spin-orbit, inter-layer potential, trigonal crystal field and finally interactions will be added step by step. The impact of each term shall then be shown in terms of the band structure where the effects are most visible. The $(1\,1\,1)$-oriented interface features a very different geometry than that of its $(0\,0\,1)$-oriented counterpart. When the cubic structure with Titanium (Ti) atoms is projected on one $(1\,1\,1)$ plane, three interspersing Ti lattices are found (Ti 1, 2 and 3), as shown in Fig. 1, which forms a triangular structure. In our modelling, only two layers are considered, assuming the coupling of the third layer to be weak as it is further away from the surface. Accordingly, the relevant hopping paths between Ti sites are along the edges of a hexagonal lattice.

In a tight-binding formalism, there exists two kinds of hopping for the two layers that we have considered-inter-layer and intra-layer, the amplitude of which depends on the distance between the concerned atoms. If only intra-layer coupling, given in Eqs. 4.1-3 is added, three bands, one of each t_{2g} orbitals, is observed, 4 times degenerate, twice in spin and twice for each layer, as for the moment there is no distinction between the two layers or the two spins.

$$a_{d_{xy}} = -2t_1\cos(\sqrt{3}k_x) \tag{4.1}$$

$$a_{d_{yz}} = -2t_1\cos(-\tfrac{\sqrt{3}}{2}k_x + \tfrac{3}{2}k_y) \tag{4.2}$$

$$a_{d_{xz}} = -2t_1\cos(\tfrac{\sqrt{3}}{2}k_x + \tfrac{3}{2}k_y) \tag{4.3}$$

where $t_1 = 0.05eV$ is the intra-layer hopping amplitude. The inter-layer coupling, given in

Eqs. 4.4-6 is then added.

$$a^{'}_{d_{xy}} = -t_2 - 2t_3\cos(\tfrac{\sqrt{3}}{2}k_x)e^{-\mathrm{I}\frac{3}{2}k_y} \tag{4.4}$$

$$a^{'}_{d_{yz}} = -t_3(1+e^{\mathrm{I}(\frac{\sqrt{3}}{2}k_x-\frac{3}{2}k_y)}) - t_2e^{-\mathrm{I}(\frac{\sqrt{3}}{2}k_x+\frac{3}{2}k_y)} \tag{4.5}$$

$$a^{'}_{d_{xz}} = -t_3(1+e^{-\mathrm{I}(\frac{\sqrt{3}}{2}k_x-\frac{3}{2}k_y)}) - t_2e^{\mathrm{I}(\frac{\sqrt{3}}{2}k_x-\frac{3}{2}k_y)} \tag{4.6}$$

where $t_3 = 1.6eV$ and $t_2 = 0.07eV$ are first and third nearest neighbour hoppings between layers. These hopping parameters have been taken from a tight binding fit to the ARPES data of Ref. [103]. This will cause a splitting of this manifold into three bonding and three anti-bonding bands, twice degenerate in spin, each. Only the lower energy bonding states are then required, which lie close to the Fermi level as the anti-bonding levels are $\simeq$ 3eV higher in energy and thus, play no active role. An inter-layer electrostatic potential is added to distinguish between the two layers in terms of their distance from the surface, which has the effect of increasing the distance between the bonding and the anti-bonding orbitals, formed at the previous step, without changing their character or curvature.

Using Dirac's notation, the Hamiltonian H_o in basis of $\{d_{xy_{1,\sigma}}, d_{yz_{1,\sigma}}, d_{xz_{1,\sigma}}, d_{xy_{2,\sigma}}, d_{yz_{2,\sigma}}, d_{xz_{2,\sigma}}\}$ for the two layers and where $1, 2$ is the layer index and σ for spin $\uparrow, \downarrow$, is given by

$$H_{o;\sigma} = \sum_{P=(d_{xy},d_{yz},d_{xz})} |d_{P,1,\sigma}, d_{P,2,\sigma}\rangle \, \mathbf{M} \, \langle d_{P,2,\sigma}, d_{P,1,\sigma}| \tag{4.7}$$

where

$$M = \begin{bmatrix} a_P & a^{'}_P \\ a^{'*}_P & b_P \end{bmatrix} \tag{4.8}$$

Here $b_P = a_p + \Delta V$, ΔV being the difference of potential between the two layers owing to the distance from the surface.

4.3.2 Trigonal Field, bulk spin-orbit coupling and confinement potential

The next term in the modelling is the trigonal crystal field which arises as a result of the changed $(1\,1\,1)$ symmetry at the surface. The ligands at the surface now begin approaching

in a planar trigonal way, perturbing the orbitals as they have a stronger effect on the d_{xy} which lies in the plane. This lifts of the degeneracy at Γ point of the bands. The magnitude of the trigonal field is given by $tf = 10$ meV and it is represented in the $\{d_{xy}, d_{yz}, d_{xz}\}$ basis by

$$H_{trf} = \begin{bmatrix} 0 & tf & tf \\ tf & 0 & tf \\ tf & tf & 0 \end{bmatrix} \tag{4.9}$$

This needs to be added to each layer and each spin separately. The next term to be added will be the bulk spin-orbit interaction.

Bulk spin-orbit interaction, $H_{so} = \lambda \vec{L}.\vec{S}$ where $\lambda = 0.025$ eV, couples the orbital and spin degrees of freedom within each layer and changes the character of a band from pure t_{2g} to a mixture of all three t_{2g} orbitals. It also creates a spin-split off band at Γ. It is to be noted that away from the Γ point, the bands retain their pure t_{2g} character.

The final term before the addition of correlations is the modelling of the quantum confinement at the surface of the $(1\,1\,1)$-oriented interface. Even though the estimation from ARPES data seems to suggest very little confinement of the gas, PS calculations show that the bands introduced above give rise to sub-bands in the quantum well created by the surface potential, and lie very close to each other. At least, two of these sets of sub-bands are close in energy to E_F and must be considered in the effective tight-binding modelling. The Hamiltonian of one set of sub-bands can be constructed with $H_{0,\uparrow}, H_{0,\uparrow}, H_{1,so}, H_{2,so}$ and H_{trf} in the basis of $|d_{P,1,\uparrow}, d_{P,2,\uparrow}, d_{P,1,\downarrow}, d_{P,2,\downarrow}\rangle$. A similar matrix exists for the sub-band set two with a shift of the bands by 20 meV as given by P-S calculations.

4.3.3 The addition of correlations

Correlations become important in this modelling as the experimental data shows that the back-gate voltage tunes the number of carriers in the system and they increase with increasing back-gate voltage and we operate under the premise that the carriers added are electron-like.

A Hartree-Fock interaction is then added which acts on individual orbitals. From

therein stem two contributions to the correlation term, those between like (U) and unlike (U$^{'}$) orbitals, whose product with the band populations of like and unlike orbitals respectively, gives rise to the Hartree-Fock contribution for each orbital as given in Eq. 4.10.

$$U_i < N_i >= U < n_i > + U^{'} \sum_{j \neq i} < n_j > \tag{4.10}$$

where $< N_i >$ is the total population of the ith band and $< n_i >$ is the population of the individual orbitals for i $\in \{xy, yz, xz\}$. The total Hartree-Fock contribution for a band is given by summing over the individual contribution over each orbital and then over the spin and layer degree of freedom. As U and $U^{'}$ are added, all orbitals would not be equally punished and would result in bands being shifted unequally resulting in band crossings. Before the addition of U and $U^{'}$, the total population,N_0 , is calculated and this should remain constant even after the addition U and $U^{'}$. At each iteration of the code, adding U and $U^{'}$ causes a shift of the bands while the Fermi level remains unchanged. The total band population, N_i, is then calculated by summing up individual populations and compared to the N_0. The fermi level is re-adjusted to regain the original total population which again changes the band populations and causes the U and $U^{'}$ to shift the bands at the next iteration. This process is made self consistent until $N_i = N_0$, without any adjustment of E_F required. A few results for various values of U is shown in the next section. As E_F is tuned and the carrier concentration increased, a band inversion between sub-band 1 and sub-band 2 takes place and the crossing points between the sub-bands also move closer to E_F. It is important to note, however, that even without the addition of correlations, there exist band crossings between one band of sub-band 1 and another of sub-band 2. However, the location of these crossing points is above the Fermi level as can be seen in Figure 4.3 for low correlations, an increase in the value of U, causes those to move closer to E_F such that they become experimentally accessible.

4.4 Numerical solution of the modelling

For the numerical application, we shall follow the same step by step procedure we had followed in the theoretical modelling. First we begin analysing the band structure for one set of sub-bands with just the intra and inter layer couplings, only zooming in on the low energy spectrum consisting of the bonding states. We will only show two crystallographic directions $k_x = 0$ and $k_y = 0$ where k_x corresponds to ΓM and k_y to ΓK of the hexagonal BZ. Only two bands, degenerate at Γ, are seen with two different effective masses similar to what is observed in ARPES. As the bulk SOC is added, a spin-split off band appears at $\equiv 25meV$ above the other two bands which remain degenerate at Γ. With the addition of trigonal crystal field, the degeneracy at Γ is completely removed and three distinct bands appear. They mix all three t_{2g} orbitals near Γ but regain their pure orbital character as one moves away from Γ. The band structure with the addition of bulk SOC and trigonal field is shown in Figure 4.2 (with a sorting according to the energies of the bands) and one sees firstly a SOC splitting near Γ which becomes enhanced as the trigonal field is added.

With the addition of a second set of sub-bands, the band picture gets slightly more involved and Lifshitz points, which are the crossings of bands belonging to one set of sub-bands with bands belonging to another set, start appearing. These crossings between bands of two different sub-band manifolds will be denoted by LP. The change in the band population is achieved by tuning the Fermi level E_F which is in turn renormalised by the correlations.

Once the correlations are added, the bands start shifting to accommodate the extra electrons which will also shift the band crossings. It is to be noted that the range of values of U used will be between 2-4 eV because below 2 eV there is very little band inversion and above, there are unstable oscillations between the band occupations. These oscillations might be stabilised if a smearing of the energies near E_F is added or if the number of k-points is increased. The number of k-points used are 40×40 for each quadrant, taking the total to 80×80 in the whole BZ. The value of U used for the first sub-band is $U = 4$ eV and $U' = 0.7 \times U$ and the values are 10% of their values for the second sub-band. Up to a first order approximation, it is reasonable to suppose that the second sub-band

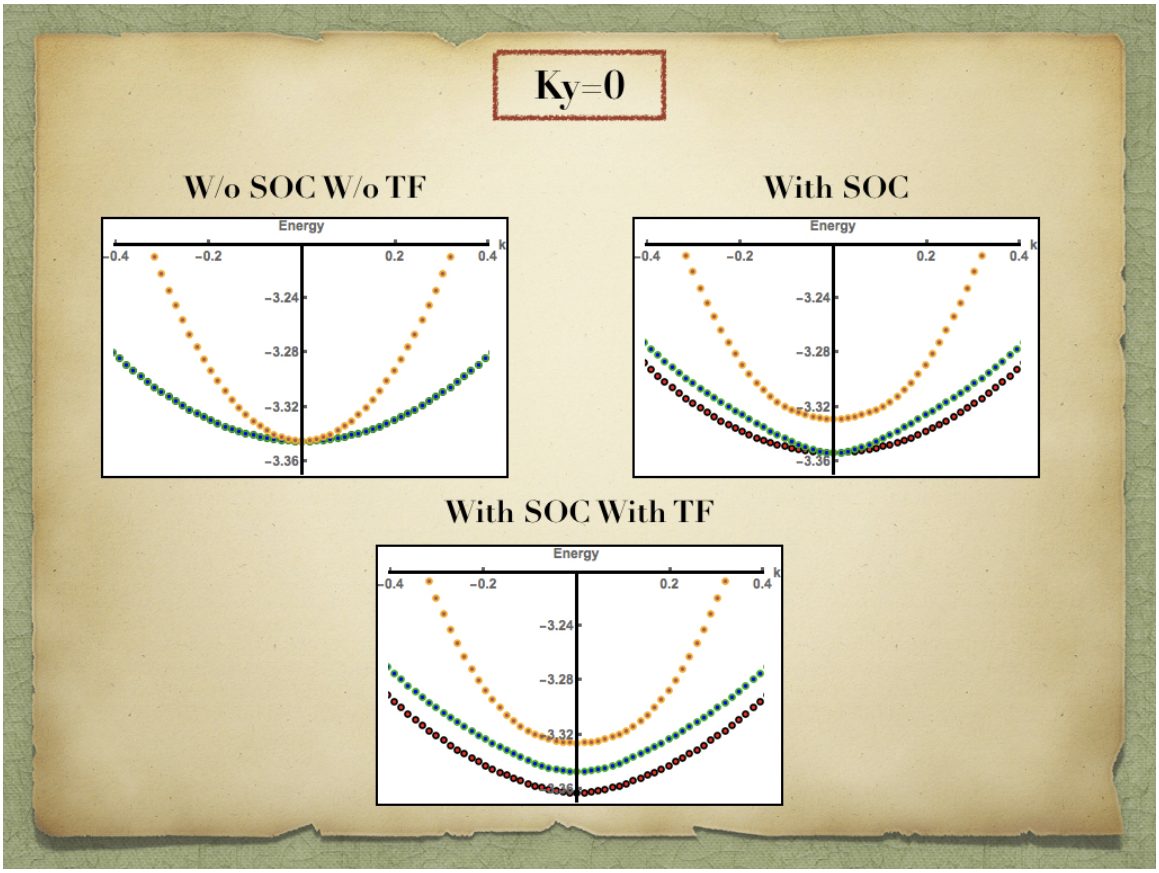

Figure 4.2: The effect of adding the bulk SOC and the trigonal Field (denoted by TF) on the band structure is seen in this figure. Note that the bands are just sorted according to their energies.

is less confined, higher in energy and will have a lesser correlations. The shift between the two-sub-bands is taken to be 20meV which is a reasonable approximation from PS calculations without U. As the correlations are tuned from U=4 ev to U=2 eV, the LP shifts and comes closer to E_F and closer to Γ. The most flagrant motion of the LP occurs in the $k_x = 0$ direction which is shown in Figure 4.3. Now the bands are sorted according to their dominant orbital character to show the LPs.

The band occupation is calculated as the number of states below E_F divided by the total number of states over the whole BZ. If the band occupation is averaged over the whole BZ over one set of sub-bands, then the band inversion takes place (for U=4 eV) for a critical value of the filling as can be seen from the Figure 4.4 which is a plot of the averaged band population over one sub-band manifold versus the variation in the filling of the bands.

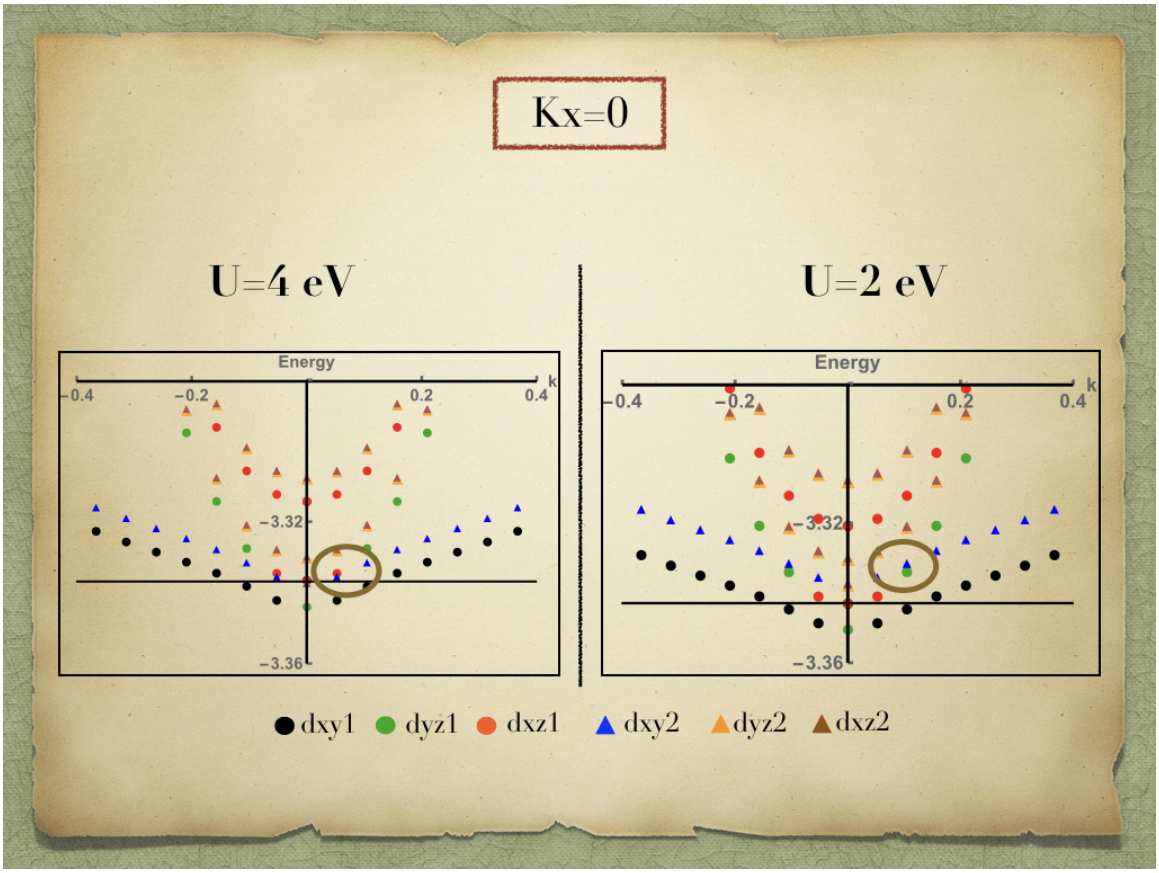

Figure 4.3: The band structure along the $k_x = 0$ orientation for two different values of U, U=2 and 4 eV is shown here. Encircled is the crossing point (LP) which moves closer to Γ and E_F as U is increased. The horizontal line indicates the renormalised E_F after the addition of correlations. Note that the bands are sorted according to their dominant orbital character.

The variation of the sub-band populations as a function of the gate voltage can be seen in Appendix C.

4.5 Kinds of topological surface states at the $(1\,1\,1)$ surface

4.5.1 Parity inversion driven surface states

LAO/STO $(1\,1\,1)$ is an extremely interesting compound when it comes to its topological nature. It can be compared to another similar system KTO $(1\,1\,1)$ where a topological metal exists; topological states co-exist with the 2DEG around 1 eV below the E_F. The value of

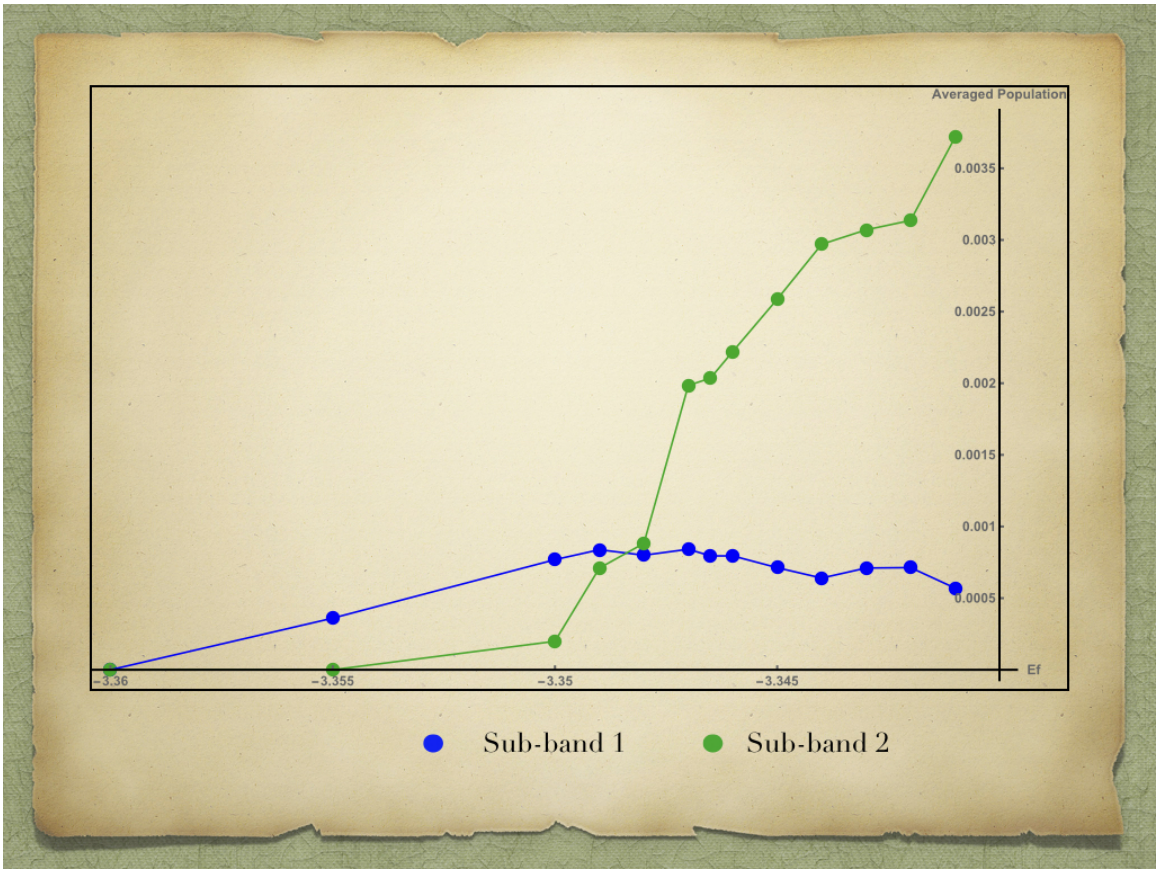

Figure 4.4: The averaged populations of sub-band 1(blue) and sub-band 2 (green) are shown as the Fermi level is tuned. At first, only the sub-band 1 is filled but there appears a point where the population of sub-band 2 picks up and increases at the expense of sub-band 1.

the bulk spin-orbit coupling is very large in the case of KTO due to the heavy Ta atom. It is also shown that a parity inversion in the ground state wavefunction takes place at one of the M ($\bar{M}$ in ARPES) points, resulting in a non trivial topological $Z_2 = 1$ invariant following the Kane and Mele. This choice of getting parity inversion at 1 or 3 points depends on the choice of basis and the authors in this paper [35] find 1. This result, a priori, does not depend on the bulk SOC. However, the stability of the edge states does depend on the spin-orbit coupling because it makes the energy gap finite everywhere in the BZ ([44]). The filling is also much greater as compared to STO and the K, $\bar{M}$ points are easily accessible. A similar calculation can then be done in the case of STO $(1\,1\,1)$ as the tight binding model is very similar, albeit a few differences in the magnitude of the tight-binding parameters.

However, due to the low filling of STO, the $\bar{M}$ point where the edge states occur, will never be reached and it might be experimentally difficult to tune k_F to reach $\bar{M}$. However, in LAO/STO$(1\,1\,1)$, since the confinement is larger, the filling might be sufficient to observe the $\bar{M}$ points as a function of gating. The interested reader is advised to peruse Ref. [116] for more details.

However, parity inversion driven topological states areu not be the only ones that can exist.

4.5.2 Correlation driven surface states

Due to the correlations added, we have shown that there is a band inversion between bands of different parities belonging to different sub-bands as well as band crossings at the LPs between bands of sub-band 1 and 2. In particular, there are six points in the BZ where three bands (2 of sub-band 1 and 1 of sub-band 2) become degenerate. If we focus on one of these points, (the one at $k_y = 0$ for example), a simplified tight-binding modelling can then be constructed involving the bands in question, namely 2 bands of sub-band 2 of dominant $d_{xz/yz}$ and 1 band of sub-band 1 of dominant d_{xy} character. A simple symmetry operation is required to switch between the LPs and it involves rotation by $2\pi/3$. The change in the orbital character of the bands around the BZ is such that the bands for sub-band 1 and 2 change their dominant character from one point to another. For simplicity, the trigonal crystal field and the inter-layer potential have been set to zero. Including them does not restrict the generality of our derivation. With only the inter and intra-layer terms in sub-band 1, a simplified Hamiltonian for each of the t_{2g} orbitals in layer 1 and layer 2 then exists. For the d_{xy} orbitals, in the basis of d_{xy1} and d_{xy2}, the matrix is just composed of intra-site energy and inter-layer hopping.

$$\begin{bmatrix} a_{d_{xy1}} & a^{'}_{d_{xy1}} \\ a^{'*}_{d_{xy1}} & a_{d_{xy1}} \end{bmatrix} \tag{4.11}$$

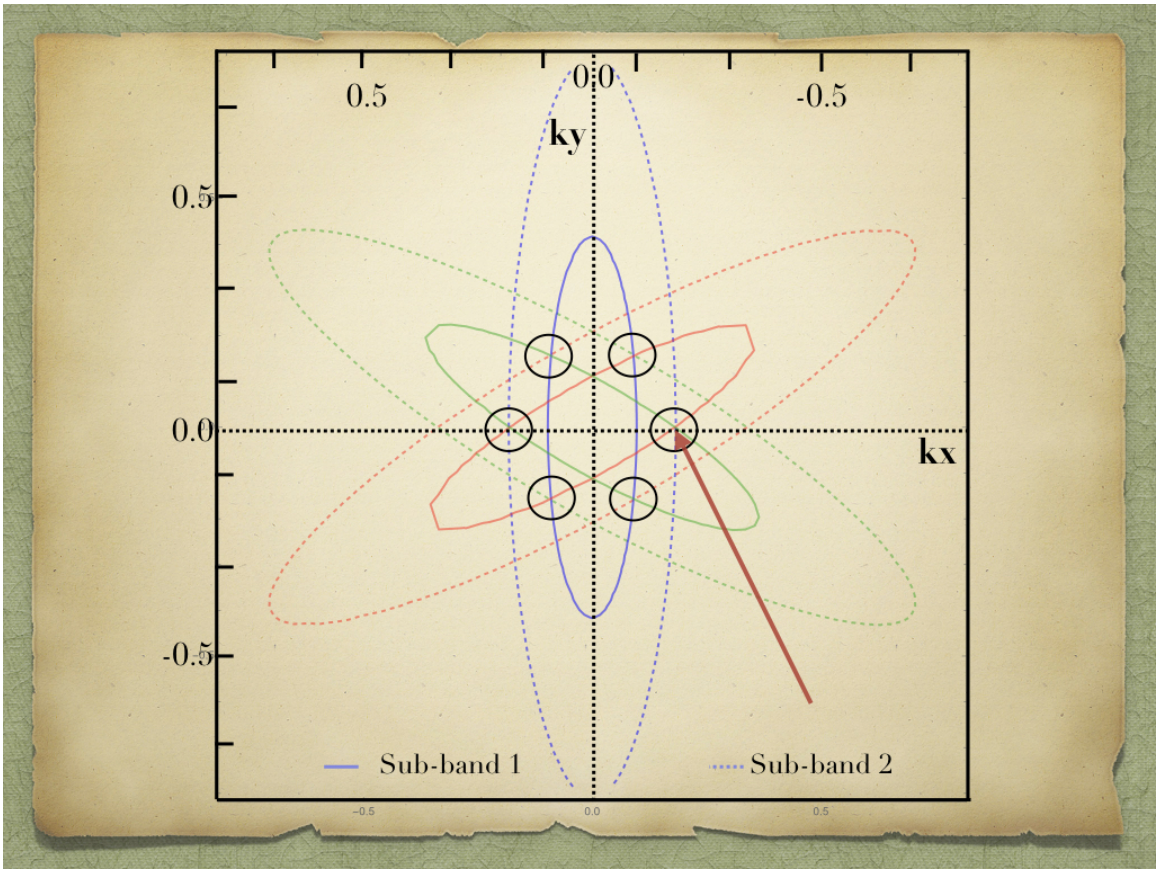

Figure 4.5: The crossing points or the LPs for bands belonging to sub-band 1 (dotted lines) and sub-band 2 (solid lines) are shown. They are six as expected from the hexagonal symmetry and we shall focus on the one lying along the $k_x = 0$ line in the first quadrant as indicated by the arrow.

where $1, 2$ are the sub-band index and the energies have been taken from Eqs. 4.1 and Eqs. 4.4. On diagonalising the matrix, one gets bonding and anti-bonding energies and orbitals.

$$a^{b}_{d_{xy1}} = a_{d_{xy1}} - \left| a^{'}_{d_{xy1}} \right| \tag{4.12}$$

$$a^{ab}_{d_{xy1}} = a_{d_{xy1}} + \left| a^{'}_{d_{xy1}} \right| \tag{4.13}$$

where the superscripts b and ab are for distinguishing between bonding and anti-bonding states. Owing to the large energy gap between the two states $(3eV)$, we shall only consider the low energy bonding states. Similar matrices exist then for the rest of the t_{2g} orbitals. The Hamiltonians for the orbitals of sub-band 2 can also be constructed in a similar fashion

with just a rigid energy difference of $e_s = 30meV$ between the two sets of sub-bands which has been increased from the previous calculations just to enhance the effects of the band crossings. The minimum model around the crossing point at $k_y = 0$, in the basis of the bonding orbitals of sub-band 1 and sub-band 2, i.e. d_{xy1}, d_{yz2} and d_{xz2}, is the following-

$$H_0 \otimes \mathbb{1}_2 = \begin{bmatrix} a^b_{d_{xy1}} & 0 & 0 \\ 0 & a^b_{d_{yz2}} + e_s & 0 \\ 0 & 0 & a^b_{d_{xz2}} + e_s \end{bmatrix} \tag{4.14}$$

This will result in a band crossing of all three bands at a point,k_c, denoted by (k_{cx}, k_{cy}) where $k_{cy} = 0$. From Chapter 3, we know that bulk SOC plays an essential role at the crossing point of the three orbitals. Here we shall add the SOC in the mixed basis of sub-band 1 and 2 as a first order low-energy perturbation. In reality, this should have been added to each of the sub-band basis and then the SOC split bands should have been taken into account but as we shall see, this does not qualitatively change the picture. Upon adding bulk SOC in the basis of $d_{xy1,\uparrow}, d_{yz2,\uparrow}, d_{xz2,\uparrow}, d_{xy1,\downarrow}, d_{yz2,\downarrow}, d_{xz2,\downarrow}$ the Hamiltonian given in Eq. 4.15 becomes-

$$H_0 \times \mathbf{1} + H_{so} = \begin{bmatrix} a^b_{d_{xy1}} & 0 & 0 & 0 & \lambda^{'} & -i\lambda^{'} \\ 0 & a^b_{d_{yz2}} & i\lambda^{'} & -\lambda^{'} & 0 & 0 \\ 0 & -i\lambda^{'} & a^b_{d_{xz2}} & i\lambda^{'} & 0 & 0 \\ 0 & -\lambda^{'} & -i\lambda^{'} & a^b_{d_{xy1}} & 0 & 0 \\ \lambda^{'} & 0 & 0 & 0 & a^b_{d_{yz2}} & -i\lambda^{'} \\ i\lambda^{'} & 0 & 0 & 0 & i\lambda^{'} & a^b_{d_{xz2}} \end{bmatrix} \tag{4.15}$$

where $\lambda^{'} = \lambda/3$ is the bulk SOC constant of Ti as seen in Chapter 3 and $\mathbf{1}$ is the unit matrix. This results in the tilted Dirac cones and a spin-split off band as we had seen earlier at k_c. The Dirac cones are tilted maximally in the $k_y = 0$ direction and minimally in the $k_x = k_{cx}$ direction which will be two directions of interest similar to the ΓM and the Δ direction of Chapter 3. The degeneracy of the bands is two-fold as the space-inversion symmetry in not broken. It is to be remembered that k_x corresponds to ΓM and k_y to ΓK of the hexagonal

BZ.

An interesting observation is the surface rumpling which is present due to the polarity of the interface. In the $(1\,1\,1)$ direction, LAO has alternating charged planes of Al^{3+} and $[LaO_3]^{3-}$ while STO has alternating charged planes of Ti^{4+} and $[SrO_3]^{4-}$. This difference in polarity should cause distortions at the surface in the form of octahedral tiltings and rotations and will result in an orbital mixing (OM) term, similar to the one seen in Chapter 3. The OM between d_{xy} and the other two t_{2g} orbitals is denoted by r_i where $i \in (d_{yz}, d_{xz})$ and r is the strength of the OM term which will be tuned. The OM mixing term, around the crossing point at $k_y = 0$ in the hexagonal lattice is the following-

$$r_1 = -2ir\sin(\tfrac{\sqrt{3}}{2}k_x + \tfrac{3}{2}k_y) \tag{4.16}$$

$$r_2 = -2ir\sin(\tfrac{\sqrt{3}}{2}k_x - \tfrac{3}{2}k_y) \tag{4.17}$$

The addition of this term will break the space inversion symmetry and the bands will become split and gapped. The Hamiltonian in the basis of $d_{xy1,\uparrow}, d_{yz2,\uparrow}, d_{xz2,\uparrow}, d_{xy1,\downarrow}, d_{yz2,\downarrow}, d_{xz2,\downarrow}$, now becomes-

$$\begin{bmatrix} a^b_{d_{xy1}} & r_1 & r_2 & 0 & \lambda^{'} & -i\lambda^{'} \\ r_1^* & a^b_{d_{yz2}} & i\lambda^{'} & -\lambda^{'} & 0 & 0 \\ r_2^* & -i\lambda^{'} & a^b_{d_{xz2}} & i\lambda^{'} & 0 & 0 \\ 0 & -\lambda^{'} & -i\lambda^{'} & a^b_{d_{xy1}} & r_1 & r_2 \\ \lambda^{'} & 0 & 0 & r_1^* & a^b_{d_{yz2}} & -i\lambda^{'} \\ i\lambda^{'} & 0 & 0 & r_2^* & i\lambda^{'} & a^b_{d_{xz2}} \end{bmatrix} \tag{4.18}$$

This results in an inverted and gapped band picture as seen in Figure 4.6 and in similar spin-textures seen in Chapter 3 which can be seen in Appendix B. A similar variational mapping can then be done as in Chapter 3 and with reasonable approximations, one expects it to also give rise to edge states.

In conclusion, LAO/STO $(1\,1\,1)$ is doubly topological and should give rise to two kinds of edge states. The first kind owing to the parity inversion present because of the two layers of Ti atoms in each sub-band and the second kind because of the presence of the OM term.

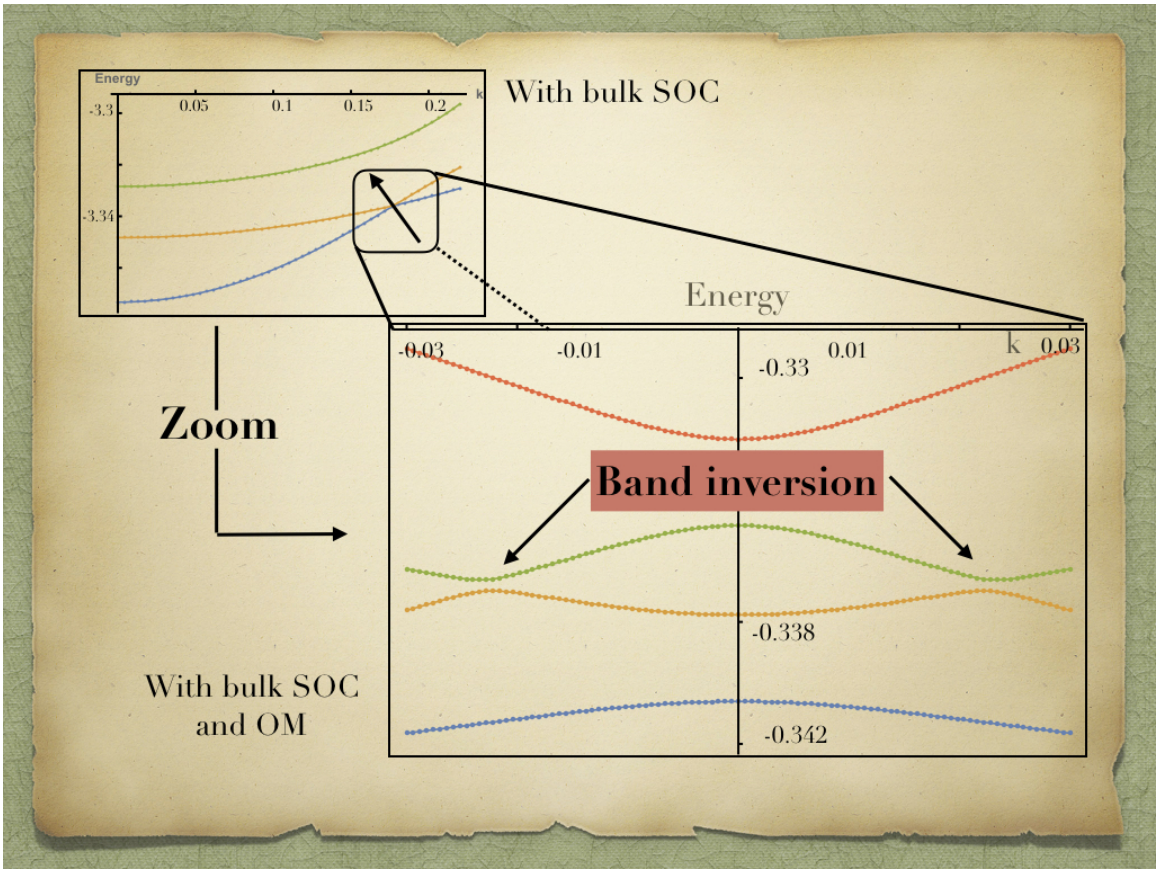

Figure 4.6: The band structure with SOC added shows a three band crossing at $k_x = 0$ similar to those seen in Chapter 3. If the OM term is added and the bands analysed in a direction parallel to $k_y = 0$ and passing through the crossing point, as indicated by the arrow, the band inversion is clearly seen.

Both are protected by the bulk SOC coupling naturally present in the system. But there remain questions that need to be addressed- what is the impact of having the two kinds of edge states, are they of similar or different natures? Will they be independent of each other or interfere positively or destructively? And what will be the consequences for the Spin Hall number - will we get twice the number of edge channels or not? Such open questions will be one of the perspectives for this work.

Chapter 5

$CaTiO_3$ at its $(0\,0\,1)$ oriented surface

5.1 Introduction

Most advances in science come when a person for one reason or another is forced to change fields.

Peter Borden

$CaTiO_3$ (CTO) is part of the perovskite family of ABO_3 oxides which have multi-functional properties. In the $(0\,0\,1)$ orientation, CTO has a strong resemblance to STO $(0\,0\,1)$, being insulating in the bulk and possessing a 2DEG at its $(0\,0\,1)$ surface. However, this perovksite compound presents a different structure than that of its cubic counterparts - there is non-negligible tilting and rotation of the oxygen octahedra which surround the Ti, even in the bulk of the system. If we now compare the experimental lattice parameters, that of CTO is 3.81 Å as compared to 3.905 Å for STO [117]. In order to ensure a close packing of the CTO crystal with a smaller A atom (the atomic radius of Ca is smaller than that of Sr), the oxygens need to move away from their cubic positions to minimise the energy of the crystal. At first, these distortions from the cubic structure should make the system less prone to metallicity as the ease of the electron-electron hopping becomes lesser. However, the gap in the bulk of CTO is the same as the band gap in STO and thus, it is not clear how distortions, even those at the surface, impact the system. In both systems, a 2DEG is seen and particularly, ARPES experiments done on CTO show occupied conduction bands [25]. There are, however, quantitative differences in the nature of the gas found at the surface of CTO as compared to that at STO which we will discuss in detail in the first section - where the bulk of the experiments will be detailed. Once the characteristics of the experimental electronic structure have been discussed, we will investigate the extent of the structural differences and their impact on the electronic properties, in an ab-initio approach,which will be the second section of the chapter. It is to be noted that a comprehensive Density Fucntional Theory (DFT) study of CTO, with the tilt and the rotation of the octahedra being considered, at the surface with and without defects had not been carried out yet [118, 119]. Next, this ab-initio study will reveal if there exist significant impacts of the structure of the material on the electronic properties and if there is a possibility of magnetism in the

system. The interplay of the confined gas with magnetism, if any, will also be discussed. And to conclude, perspectives like topology will be addressed which could have been an interesting ingredient to be added as both confinement and orbital mixing could be present in the system and we could get some band inversion in the system. Since there are 4 kinds of atoms due to the tilts and the rotations, multiple bands and gaps could be produced and the system resembles $SrIrO_3$, which is known to be a topological crystalline nodal metal. However, the third ingredient for any kind of topology, bulk spin orbit coupling (SOC), does not appear to be prominent in CTO. The lack of a prominent bulk SOC means that there will be little or no lifting of the degeneracy in the Brillouin Zone (BZ) for either band inverted structures or crystalline topological phases, further complicating the search for topological states. Nonetheless, future studies to study the topological states in CTO would offer a worthwhile challenge.

5.2 Experimental Data for the bulk and $(0\,0\,1)$ surface of $CaTiO_3$

In this section, we will discuss the bulk and surface properties of CTO which will be the basis of the ab-initio study to be carried out later.

5.2.1 Results for bulk $CaTiO_3$

Bulk CTO has a perovskite structure and is an insulator with a band gap of 3.5 eV [120]. It also exhibits moderate dielectric properties with a relative permittivity of up to 186 [121, 122]. CTO is used in various microwave applications as a low loss dielectric together with Mg_2O_3 [123] or as a transparent semiconductor with dopants like niobium [124]. $CaTiO_3$ has an orthorhombic unit cell and belongs to the $Pnma$ group with the $a^-a^-c^+$ tilt pattern, which is stable up to 1300 K [125]. Here the a^- is the out of phase tilt of the TiO_6 octahedron with respect to the x and y axes and c^+ is the in-phase octahedral tilt angle with respect to the z axis. From [117], the in-phase tilt angle with respect to the z-axis is determined to be around 9° and the out-of-phase tilt angle with respect to

the x-axis is around 12° for around 200K and the metal-oxygen bond (O5-Ti-O3 in Figure 5.1) angle is 156° [126] . Crystal structure of the calcium titanate perovskite CaTiO3 was studied by neutron diffraction data collected over the temperature range of 296 to 1720 K by Yashima et al[127]. Below 1512$\pm$13 K, the structure is $Pnma$ and above it changes to a tetragonal $I4/mcm$ and then above 1635$\pm$12 K to a cubic $Pn\bar{3}m$ structure. The lattice parameters as determined from this study for the orthorhombic unit cell (in Å) are $a = 5.37, b = 5.42, c = 7.63$ which is in accordance with previous studies [128, 126, 120]

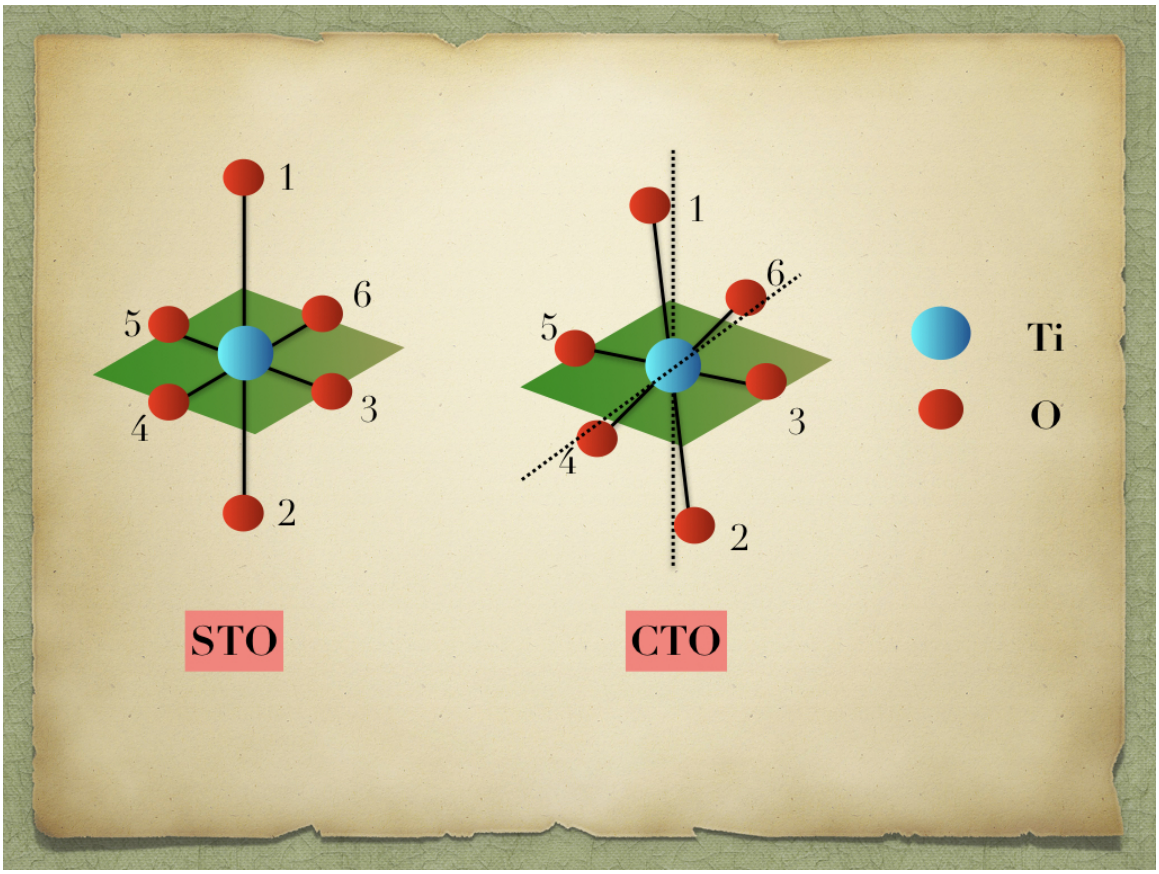

Figure 5.1: A sketch of the cubic TiO_6 octahedra found in STO with the Ti atoms in blue, the oxygen in red on the left. The labelling of the oxygen atoms has been done to specify angles between the bonds and in green is the TiO_4 plane. The right hand side figure shows the rotation and tilting of the octahedron in CTO.

5.2.2 Experimental results on the $(0\,0\,1)$ surface of $CaTiO_3$

The surface spectroscopy for CTO was performed by the Tobias Rodel et al [25] and by S Muff et al [129]. To obtain the $(0\,0\,1)$ surface, single crystals of CTO were polished or

alternatively single crystals were fractured giving access to the surface. Under the irradiation of the synchrotron beam, oxygen vacancies were created and estimated to be around 6% assuming all the released electrons formed give rise to the confined gas. Alternatively, a deposition of 2 Å of Aluminium (Al) done on the surface gives a uniform concentration of oxygen vacancies, similar to the procedure followed for STO. ARPES measurements then revealed a metallic surface or a 2DEG confined to the surface, with a Fermi Surface (FS) consisting of a four-pointed star and two concentric circles. The concentric circles were reminiscent of STO where they were assumed to be dominant d_{xy} bands. But the cigar-shaped FS in STO gave way to the star shape in CTO, which was indicative of hybridization between the t_{2g} orbitals. Next, the energy dispersion was analysed and was found to consist of three bands - two highly dispersive bands and one band of a less dispersive nature. Owing to their effective masses determined by parabolic fits, these three bands could not be attributed to the light d_{xy} orbitals and the heavy $d_{xz}(d_{yz})$ in the $k_y(k_x)$ orientation as was the case for STO. The effective masses of the two dispersive bands was found in CTO (STO) to be 1.1 m_e (0.7 m_e) while the less dispersive band, fitted at Γ, was found to be 2.7 m_e (8 m_e). This difference of mass in the less dispersive band was proof enough that the two materials had bands of different natures. In addition to the effective mass, when the orbital character of the less dispersive band was observed in the k_y direction, there seemed to be a mixing of d_{xz} and the d_{yz} orbitals. This could arise from the tilting of the octahedras which were already observed in bulk CTO.

If the confinement of the bands was then analysed, it was found that in CTO (STO), the first dominant d_{xy} band lay 158 meV (223 meV) below the E_F which meant that this band was less confined in CTO as compared to STO. The second d_{xy} band was confined even less, lying 27 meV below the E_F as compared to 110 meV in the case of STO. The first dominant $d_{xz/yz}$ band is almost at the same location as in STO, i.e. around 60 meV below E_F [25]. If now the role of oxygen vacancies was investigated for CTO, angle integrated spectra of the surface before and after irradiation showed the presence of an in-gap state around -1.3 eV and a 2DEG.

In order to understand the experimental data of a confined 2DEG and a localised state in the presence of vacancies, we will carry out a detailed DFT analysis, beginning from

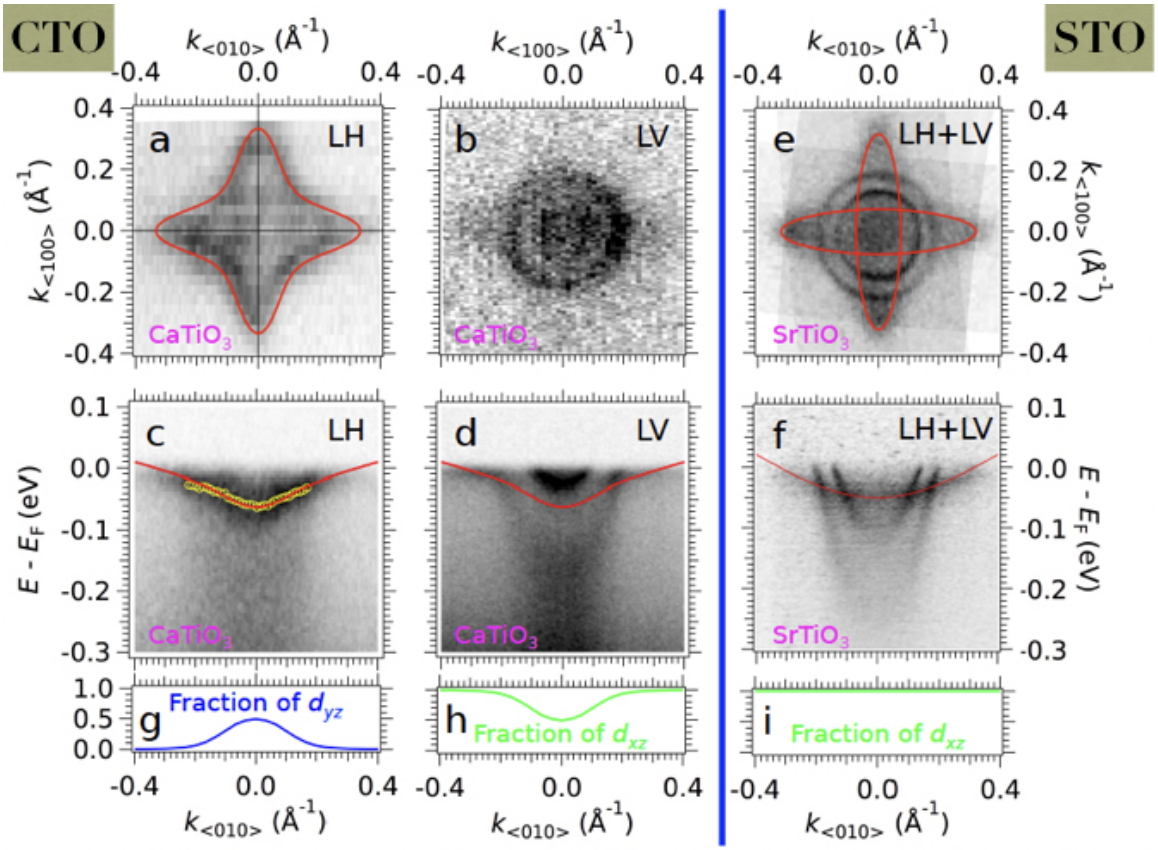

Figure 5.2: A comparison of the ARPES results for CTO and STO are detailed here- (a) and (b) are the FS maps while (c) and (d) are the energy dispersion curves. (e) and (f) are the FS and energy dispersion for STO. A clear difference in the shape of the FS, star shaped in CTO as compared to cigars in STO is seen. In the energy dispersion, the difference in the effective masses of the bands observed and the difference in confinement is also seen. As adapted from [25].

the bulk of the system and then moving up to a surface without and with vacancies. These oxygen vacancies, which will create both a 2DEG and an in-gap state, will be one of the main focus areas of the DFT analysis to follow. The interplay between localisation and delocalisation will also be investigated as a function of the correlations and an insulator to metal transition will be seen as one decreases the value of U below a critical value which is significantly smaller than that used for STO. Another area to investigate will be the hybridization of the t_{2g} orbitals; it is a natural consequence of the tilting of the octahedra in the bulk and should occur at the surface as well, which will also be explored in the DFT analysis to follow.

5.3 Ab-initio calculations

5.3.1 Brief Introduction to the Density Functional Theory

In this section, we will talk about the computational settings used for the calculations and the results that follow. Within the DFT framework, the properties of the ground state of a material is calculated using the electronic density which uniquely defines the energy of the system :

$$E[\rho(\vec{r})] = F[\rho(\vec{r})] + \int d\vec{r} V_{ext}(\vec{r})\rho(\vec{r}) \tag{5.1}$$

The universal functional F represents the electronic kinetic energy and the electron-electron interactions and V_{ext} is the external potential of the system. The electronic ground state is found by minimising Eq. 5.1 which is equivalent to solving the many-body Schrödinger equation. However, an exact analytical form for F is difficult to compute and in practice, different approximations will be used. The one used in this chapter will be the Generalised Gradient Approximation with the Hubbard correlations (GGA+U). The correlations are added to better capture the electronic properties of the seemingly localised d electrons. In DFT, it is important to choose the right unit cell which captures the symmetries and the distortions in the system. For correctly representing the anti-ferrodistortive tilts and the rotations, we have chosen a $2 \times 2 \times 2$ unit cell. After the choice of a functional and the unit cell, the position of the atoms is optimised so as to minimise the forces and the stresses in the system and give a ground state. All the electrical and magnetic properties of a system can be determined in that ground state. For a general introduction to DFT, the interested reader is advised to refer to Appendix D and the book by [130] and a well written thesis [131].

5.3.2 Computational settings for the VASP code

All calculations were performed within the Density Functional Theory (DFT), implemented in VASP (Vienna ab initio simulation package) [132, 133]. Gradient-corrected GGA (PW91),[134], GGA+U,[135] (U=3.5-5.0 eV, J= 0.64 eV), and hybrid (HSE06) [136,

137] exchange-correlation functionals were used to give robust grounds for the description of the bulk electronic structures. The interaction of valence electrons with ionic cores was described within the projector augmented wave (PAW) method,[138, 139] and the Kohn-Sham orbitals were developed on a plane-wave basis set. Standard calcium and titanium (including $3p$ electrons in the valence band), and soft oxygen (energy cutoff of 270 eV) pseudopotentials provided with VASP were used,[138, 139] enabling a full structural relaxation of all considered systems at the GGA+U level. The applicability of soft oxygen pseudopotential was validated, with results obtained with both the soft and full (energy cutoff of 400 eV) oxygen pseudopotentials in the orthorhombic unit cell.

5.3.3 Bulk results obtained for $CaTiO_3$ using VASP

For characterising the bulk, the orthorhombic $Pnma$ $CaTiO_3$ was used, with the $a^-a^-c^+$ tilt pattern and its shape and volume optimized until all elements of the stress tensor were smaller than 0.01 eV/Å^3. Simultaneously, positions of all atoms were optimized as to make all forces less than 0.01 eV/ Å. With these settings a (6×6×4) Γ-centred Monkhorst Pack sampling of the bulk Brillouin zone assures a convergence of calculated energy differences to 0.02 eV/$CaTiO_3$, and of lattice parameters to less than 0.01 Å.

The orthorhombic unit cell (u.c.), while smaller and more efficient for calculations, proved to be too small to investigate the role of defects as the concentration of defects was too high (1/12 in the orthorhombic cell as compared to 1/24 in 2×2 for 6 atomic layers in the $\hat{z}$ direction). A choice was made to then switch to the 2×2 unit cell which was first optimised in the bulk and then used to construct stoichiometric surface slabs. The lattice parameters, tilt angles and the gap are reported for GGA+U calculations for U=5 eV and U=3.5 eV and contrasted with the experimental data. GGA functionals normally underestimate the gap and overestimate the lattice parameters with both increasing with increasing U.[1]

[1]The justification of the values of U used will follow later.

	GGA+U (U=5)	GGA+U (U=3.5)	Expt
a (Å)	7.76	7.75	7.58
b (Å)	7.76	7.75	7.68
c (Å)	7.74	7.72	7.62
Gap (eV)	2.78	2.70	3.5
$\theta(^\circ)$	13.6	13.3	13
$\phi(^\circ)$	10.0	9.8	9

Table 5.1: Calculated GGA+U lattice parameters and gaps for U=5 eV and U=3.5 eV and their respective experimental values. Note that the experimental values are measured for the orthorhombic cell and are those in paper [126] multiplied by $\sqrt{2}$ to give equivalent lattice parameters for the 2×2 u.c.

Projected densities of states (PDOS) are reported in Fig. 5.3 for U=5 eV. The compositions the top of the valence band have mostly an oxygen character, while Ti states contribute principally to the bottom of the conduction band (CB). Decomposition into Ti e_g ($d_{z^2} + d_{x^2-y^2}$) and t_{2g} ($d_{xy} + d_{yz} + d_{xz}$) components shows that the states near the CB minimum display principally a t_{2g} character, consistent with the octahedral environment of Ti cations. Due to the non-negligible tilt of the TiO_6 octahedra in the bulk $CaTiO_3$ structure, the contribution of the e_g component to the bottom of conduction band is almost 10% as can be derived from the PDOS. The rotations and tilting also impact gap between the t_{2g} and the e_g, which is only 0.5 eV compared to more than 2 eV in STO. It is to be noted that the Fermi level is set to the top of the valence band, both for bulk and surface calculations. The PDOS for U=3.5 eV shows essentially the same features with a slight modification of the gap and the lattice parameters as can be seen in Table 5.1, showing that U has little impact on the structural parameters.

5.3.4 Surface characterization without defects

Surface calculations were performed on stoichiometric (2×2)-$CaTiO_3$(001) slabs, composed of eleven atomic layers (of either TiO_2 and CaO) and exposing two inequivalent terminations (TiO_2 and CaO), to better emulate experiments which show steps of mixed

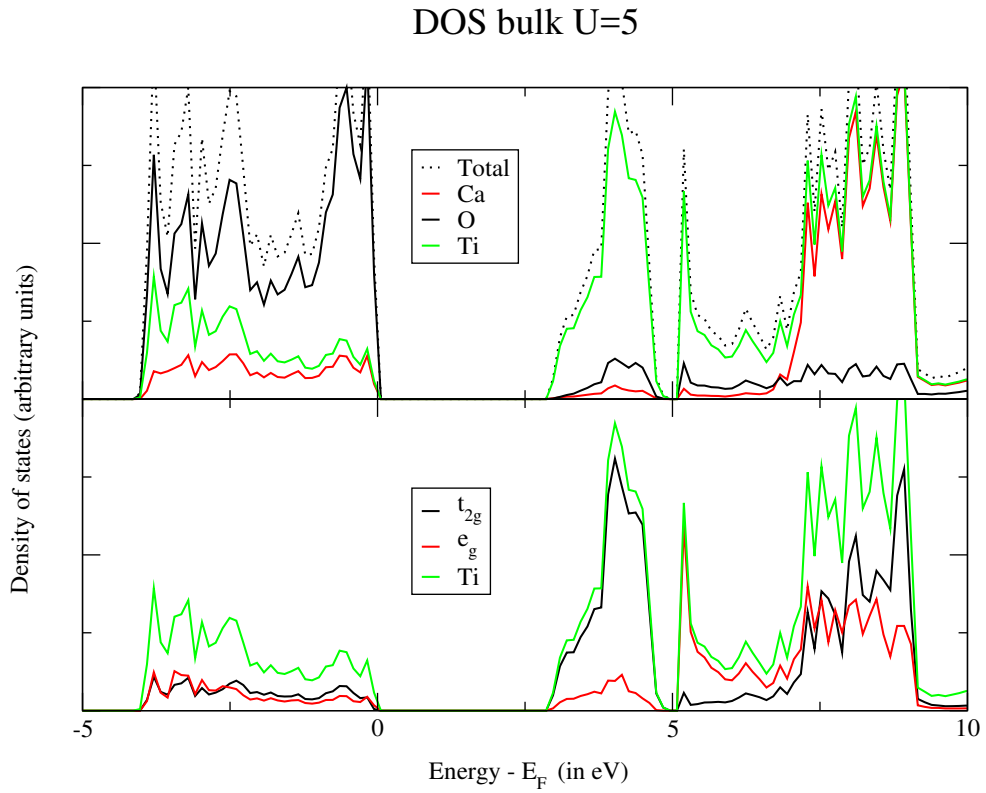

Figure 5.3: Total, Ti-, Ca- and O-projected densities of states of bulk $CaTiO_3$ obtained from GGA+U (U=5 eV) with soft oxygen pseudopotential. Decompositions into Ti e_g ($d_{z^2} + d_{x^2-y^2}$) and Ti t_{2g} ($d_{xy} + d_{yz} + d_{xz}$) components are plotted in the bottom panels.

terminations [25]. To commence with, a value of U for the d electrons in Ti atoms was chosen (U=5.0 eV, J=0.64 eV) which was similar to that used in DFT calculations performed on STO [140, 106]. The value of U was then tuned in the range of 5 to 3.5 eV to probe its impact on the electronic properties. This will be justified in a later section when we discuss defects or vacancies at the surfaces. A vacuum layer of more than 10 Å and dipole corrections were used to reduce the spurious interaction between periodic images and cancel out any electric field arising from nonsymmetric slabs. With the in-plane lattice parameters fixed to the corresponding bulk values, positions of all atoms were optimized until forces became smaller than 0.01 eV/Å. Comparison with results obtained with slabs of either 6 atomic layers of TiO_2 separated by 10 Å of vacuum or 6 layers separated by 15

Å of vacuum was done. The slab with 6 layers and 10 Å of vacuum was seen to be sufficient to carry out calculations with a (8×8×1) Γ-centred Monkhorst Pack grid assuring the convergence of the calculated surface energy to 0.02 J/m^2.

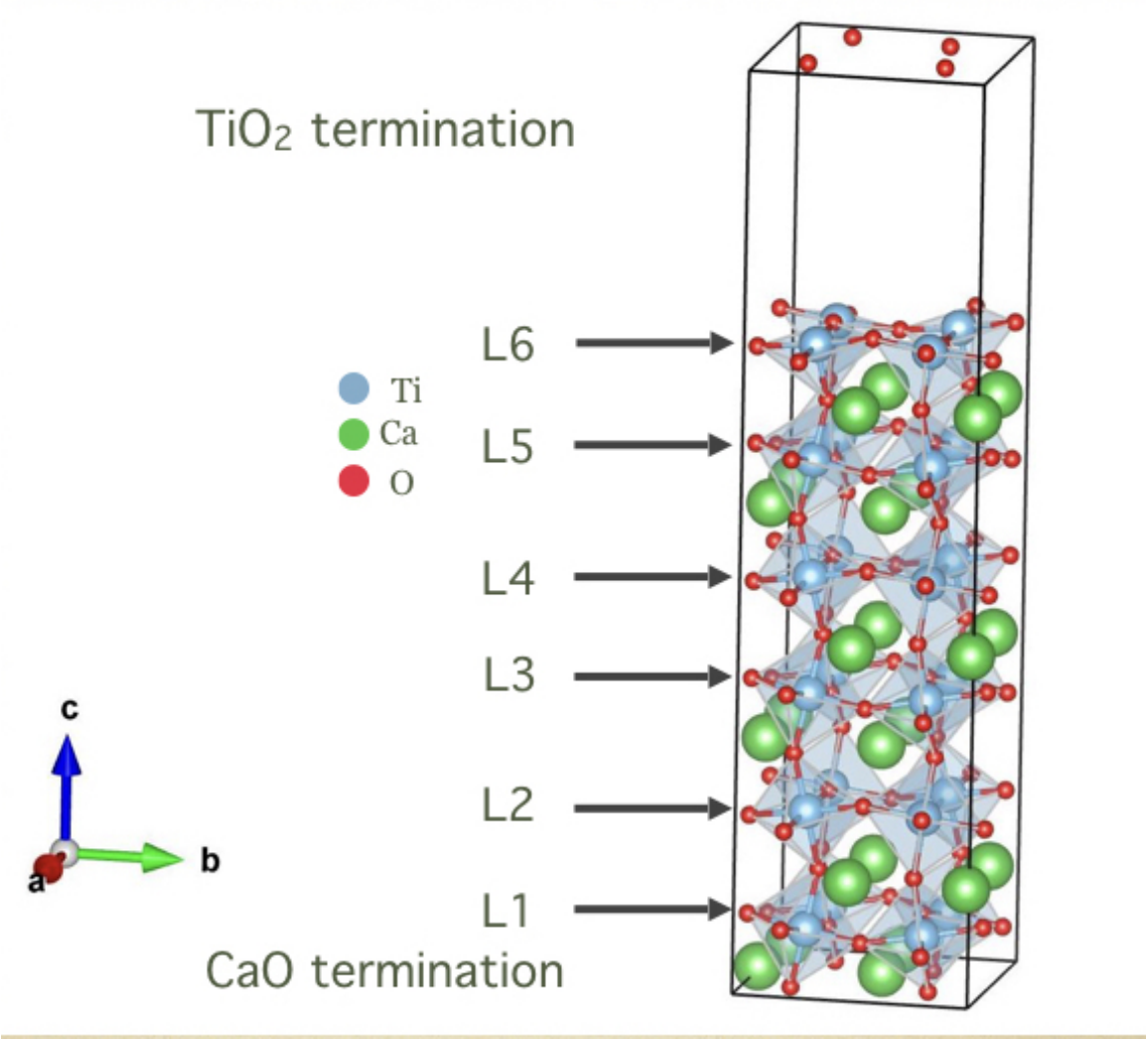

Figure 5.4: The stoichiometric slab of 11 atomic layers consisting of 6 TiO_2 planes with more than 10 Å of vacuum. The layers are labelled from the CaO termination to the TiO_2 termination.

From Table 5.2, for both values of U considered, the angles in the layers L3 and L4 are almost bulk like with very slight deviation and the layers at the surface, L1 and L6, show a strong change from the bulk values. The TiO_2 termination, L6, has the maximum deviation from the bulk values with ϕ being almost 5 ° less and thus, elastic energy is stored in the atoms. For the TiO_2 closest to the CaO termination, L1, the change in the angles is only

	U=5 eV	U=3.5 eV
E_{surf} (J/m^2)	1.12	1.16
	θ, ϕ (°)	θ, ϕ (°)
L1	12.7, 11.6	12.6, 11.3
L2	12.7, 10.1	13.4, 9.8
L3	13.4, 10.0	12.9, 9.6
L4	13.5, 9.7	13.5, 9.3
L5	13.8, 8.9	13.8, 8.6
L6	12.3, 5.1	12.1, 4.6
bulk	13.6, 10.0	13.3, 9.8
Gap (eV)	1.94	1.69

Table 5.2: Surface energies E_{surf} (J/m^2), surface work functions WF (eV), and surface tilt angles θ, ϕ (°) obtained in GGA+U calculations with slabs of different values of U, 3.5 and 5 eV. Ca and Ti refer to CaO and TiO_2 terminations, respectively and Li refers to the layer number.

slight. The apical bond lengths also change drastically at L1, becoming 1.88Å as compared to 1.99 Å in the bulk. The angles between the metal-oxygen bond no longer correspond to 90 ° (180 °) for the O1-Ti-O3 (O1-Ti-O2) in Fig. 5.1. These two factors, the change in the bond length and in the angle make it difficult to measure the angles. An approximate calculation gives the values tabulated in Tab. 5.2. It is to be noted that there is a very slight increase of the angles as we go from U=5 eV to U=3.5 eV, however, there is a reduction of the gap by around 0.25 eV which will be significant. Generally, at the surface in comparison with the bulk, the gap decreases from 2.78 eV to 1.94 eV. This decrease is due to the relative motion of the conduction and the valence band towards each other. A variety of factors can contribute to this - firstly, at the surface, half the apical bonds are broken which impacts distortions in both the bond length and the bond angles. Secondly, this distortion in the bond length would mean elastic strain which could impact the dielectric constant which cannot be effectively screened at the surface. There could also be come crystal field effects but there is very little evidence of that being present in CTO. Lastly, there are also dipole moments at the surface due to the breakage of the bonds which can also result in the bands being pulled down and the gap being reduced. This trend is not specific to CTO and indeed happens in most other surfaces.

The layer by layer density of states for a GGA+U calculation with U=3.5 is shown in

the following Figure 5.5.

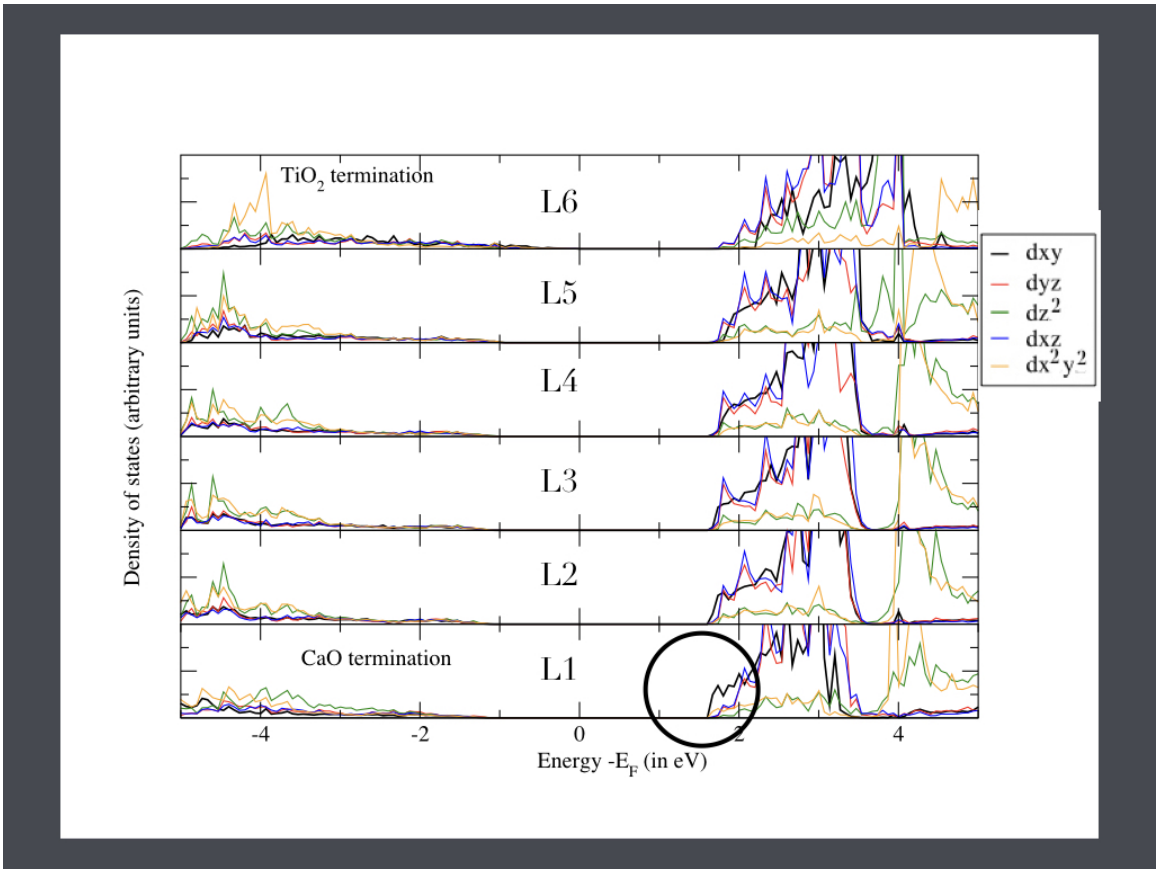

Figure 5.5: The orbitally decomposed PDOS for the slab is shown for U=3.5 eV and the CB band minimum can be seen at the CaO termination with an orbital character of majority d_{xy}. The layers L3 and L2 are bulk like in nature, retaining the bulk gap of 3.5 eV while the surface VB at L6 and the surface CB at L1 get pulled down to reduce the overall gap to 1.7 eV.

For the bulk-like layers L3 and L2, the gap is that found in the bulk. However for the two surface layers, there is a pulling down of the conduction band which results in the closing of the gap. We note that, the lowest CB is the Ti atom nearest to the CaO termination, thus, hinting that this will be the lowest energy CB and most likely the first to be filled in the case of a metallic state. The character of the lowest CB is dominant t_{2g}, in particular dxy with a minority spattering of e_g, which was already the case in the bulk.

In the case of both experiments and previous calculations done in STO, oxygen vacancies were necessary to provide the extra electrons for the 2DEG. We will investigate the role of defects for the case of one and two defects with the following configurations. For

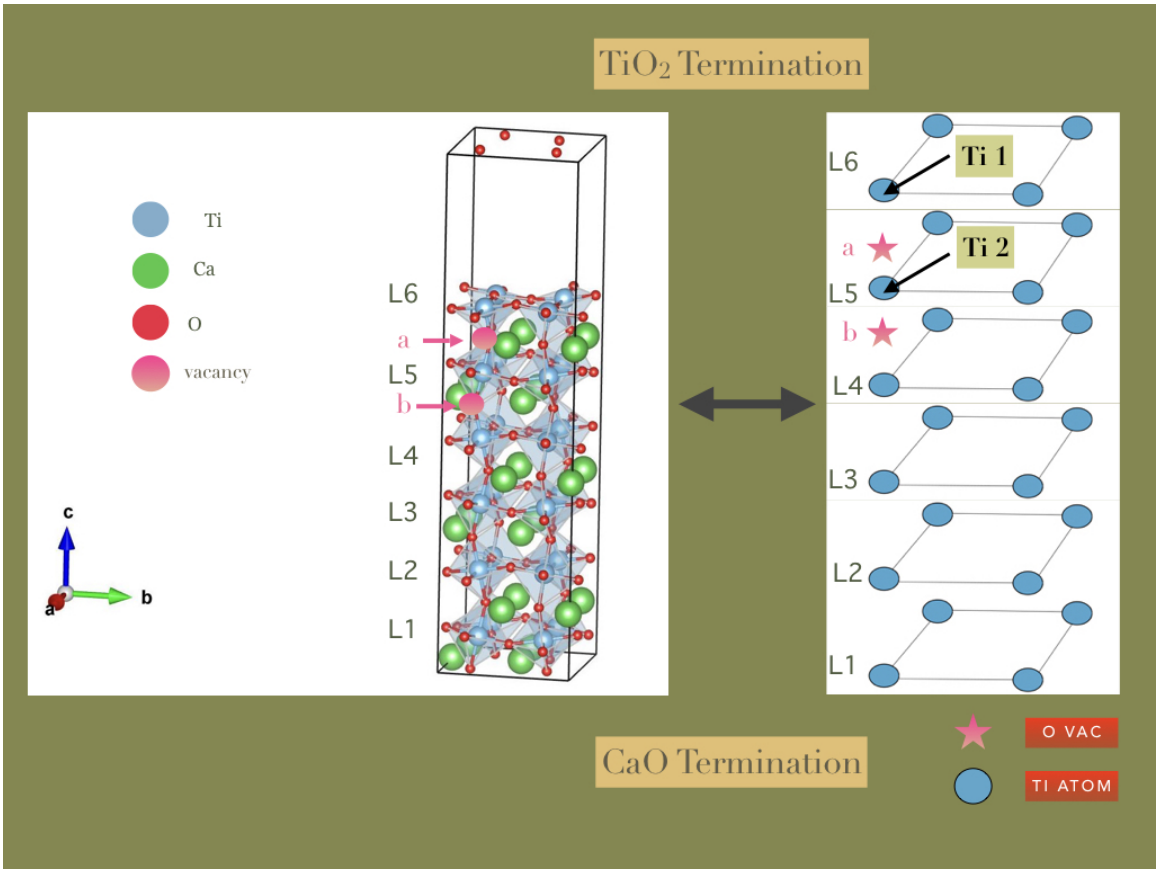

Figure 5.6: The left panel shows the vacancy configuration is shown in the slab- for the single vacancy, only one apical oxygen, a, is removed and for the double vacancy, both oxygens a and b are removed. The right panel is the simplified artist's view of the slab and its vacancies, showing just the TiO_2 planes and the relevant vacancies.

one vacancy (marked by a), the apical oxygen of a Ti atom in the subsurface TiO_2 layer, L5, is removed. For the case of two vacancies, the other apical oxygen (marked by b), for this Ti is removed. This particular vacancy configuration was the one explored successfully in the case of STO where it was necessary to explain the 2DEG and the localised state found at -1.3 eV below the E_F as we will see later. Altmeyer et al. [106] investigated the impact of O vacancies on the spin degrees of freedom of the electronic states. They found that several di-vacancy configurations lead to similar qualitative features (spin textures due to t_{2g} carriers at E_F; localized e_g moments polarising the 2DEG) and their paper focused on one particular choice (di-vacancies on the TiO_2 top surface), but quoted a few alternative configurations. Since the study emphasized the spin sector, the characteristics of the charge sector were somewhat downplayed but two aspects emerged for the latter (private

communication). One was that the vertical, sub-surface di-vacancy configuration successfully captured the in-gap state at energy -1.3 eV. Two was that for all configurations, a spatial dichotomy was observed between the extended and the localized states (the 2DEG stays away from the layer(s) where the vacancies sit. This is shown in Figure 5.7

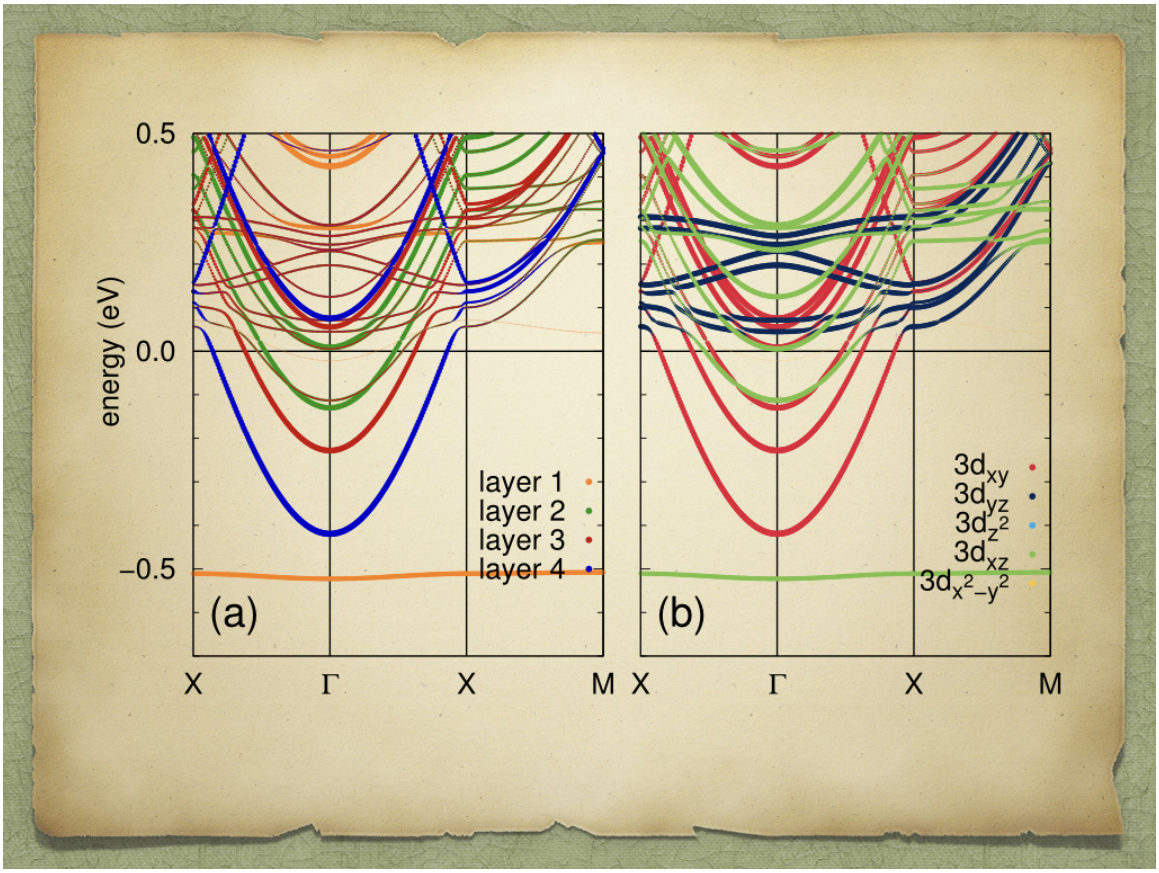

Figure 5.7: Band structure plots for di-vacancies in STO decomposed on the layers of the slab (left panel) and on their orbital character (right panel). Layer 1 on the figure is where vacancies have been created and Layer 4 where the gas is found for calculations done by Altmeyer et al.

5.3.5 Surface characterisation with defects : Oxygen vacancies

Non spin-polarised calculations

Having characterised the surface and noting the nature of the conduction bands as well as their location (CaO termination), we will now move on to a surface with defects. Investigations on both STO and in CTO have revealed that the gas prefers to be furtherest

away from the vacancies. Since the lowest CB is near the CaO termination, vacancies will be created close to the other termination, i.e. the TiO_2 termination. To capture both the localised state found at -1.3 eV and the filled conduction bands showing the 2DEG, apical oxygen vacancies will be introduced for the subsurface TiO_2 layer lying just below the TiO_2 terminated surface[2]. For the case of one sub-surface vacancy, there is no 2DEG for

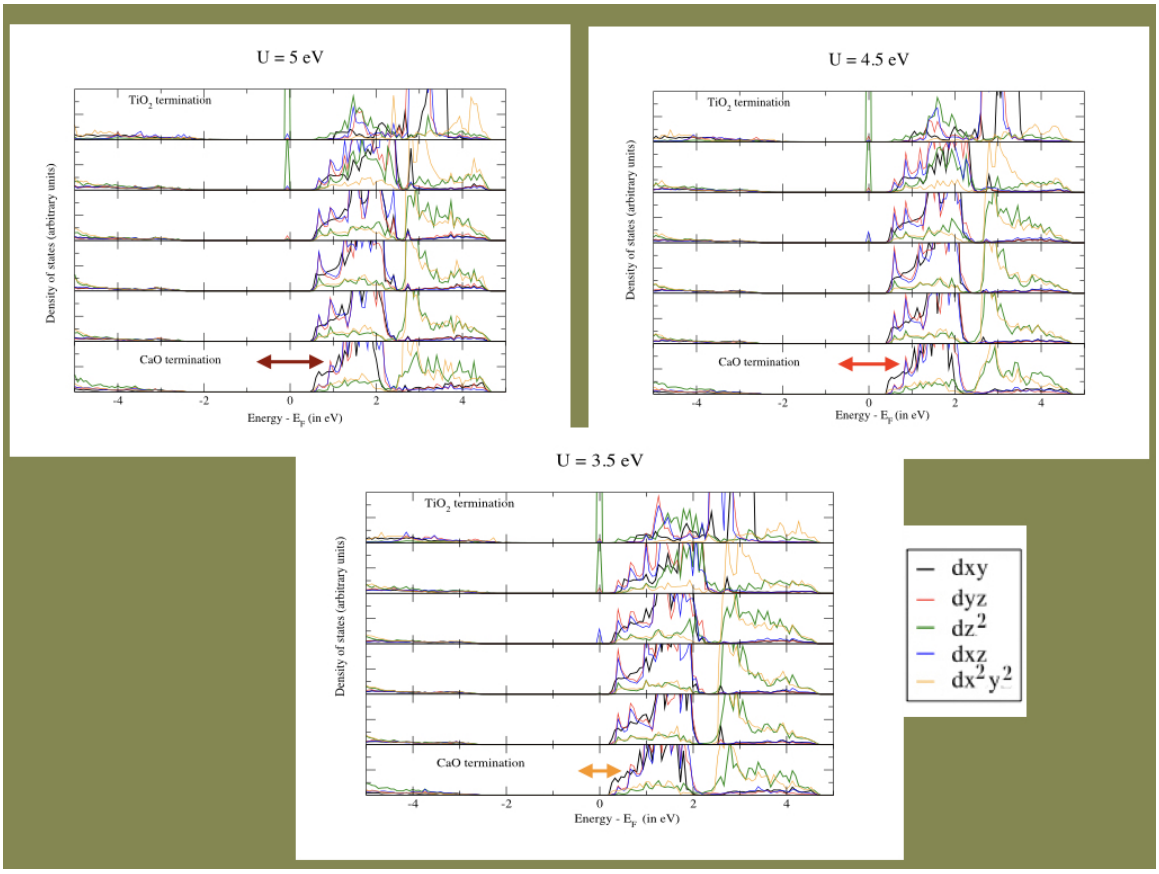

Figure 5.8: Single apical sub-surface vacancy created in the slab for various values of U. From top to bottom, left to right, U=5 eV, 4.5 eV and 3.5 eV and for all the cases, the 2 electrons released from the vacancy are localised at Ti 1 and 2. However the distance between the CB minimum, located at L6, and the localised state becomes lesser as the U is diminished as is indicated by the arrows.

U=5 to 3.5 eV and a localised state appears at around -1.3 eV below E_F. Another localised state near E_F seems to move closer to the bottom of the CB as U is reduced in value as is shown in Figure 5.8. If the electrons are counted, then the two extra electrons arising from

[2]This vacancy configuration has not been optimised for CTO and the author admits that other "better" configurations might be found but nonetheless, the results obtained for this particular configuration show an excellent agreement with experiments.

the vacancy, are both localised at the adjacent Ti atoms, Ti 1 and 2 as shown in Fig. 5.6 and have a d_{z^2} character. The orbital character can be understood by seeing that d_{z^2} orbitals are the most affected due to the apical vacancy as they have their orbital lobes pointing in the $\hat{z}$ direction.

If now the Ti atom which had previously lost one apical oxygen, is made to also lose its remaining apical oxygen, two states appear, one localised state close to -1.3 eV and another delocalised state which is evidenced by the filled conduction bands. However, the delocalised state does not occur for any value of U; U needs to lie in the range of 3.5 to 4.5 eV. The value of U is to be chosen carefully because it drives a metal to insulator transition if increased to an unphysical value.

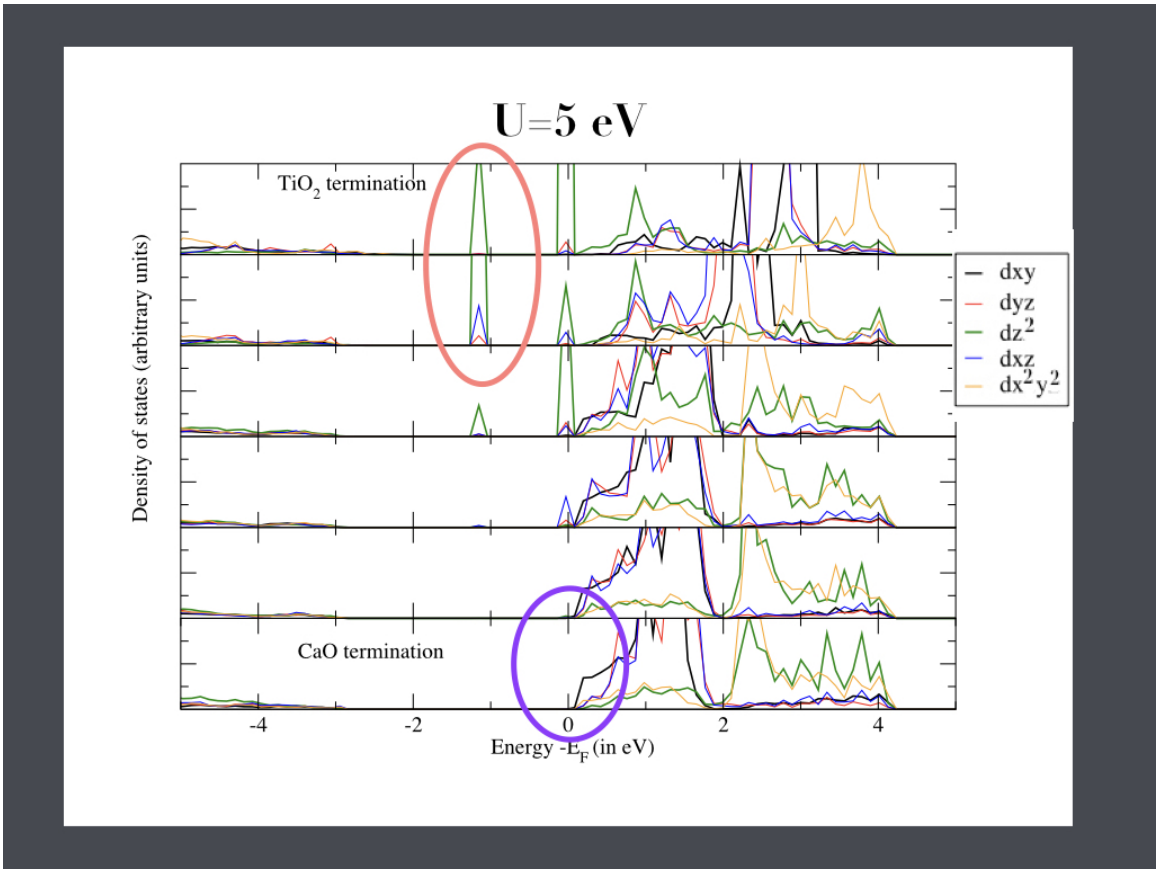

Figure 5.9: The PDOS for the 2 vacancies using U=5 is shown. For U=5 eV, two localised states, each with two electrons, one around -1.3 eV and another close to E_F indicate that the 4 electrons released by the vacancies have been localised on adjacent Ti atoms. The orbital character of the states is d_{z^2} as is expected for apical vacancies.

The value of U=5 eV is derived from STO which is different from CTO as the latter

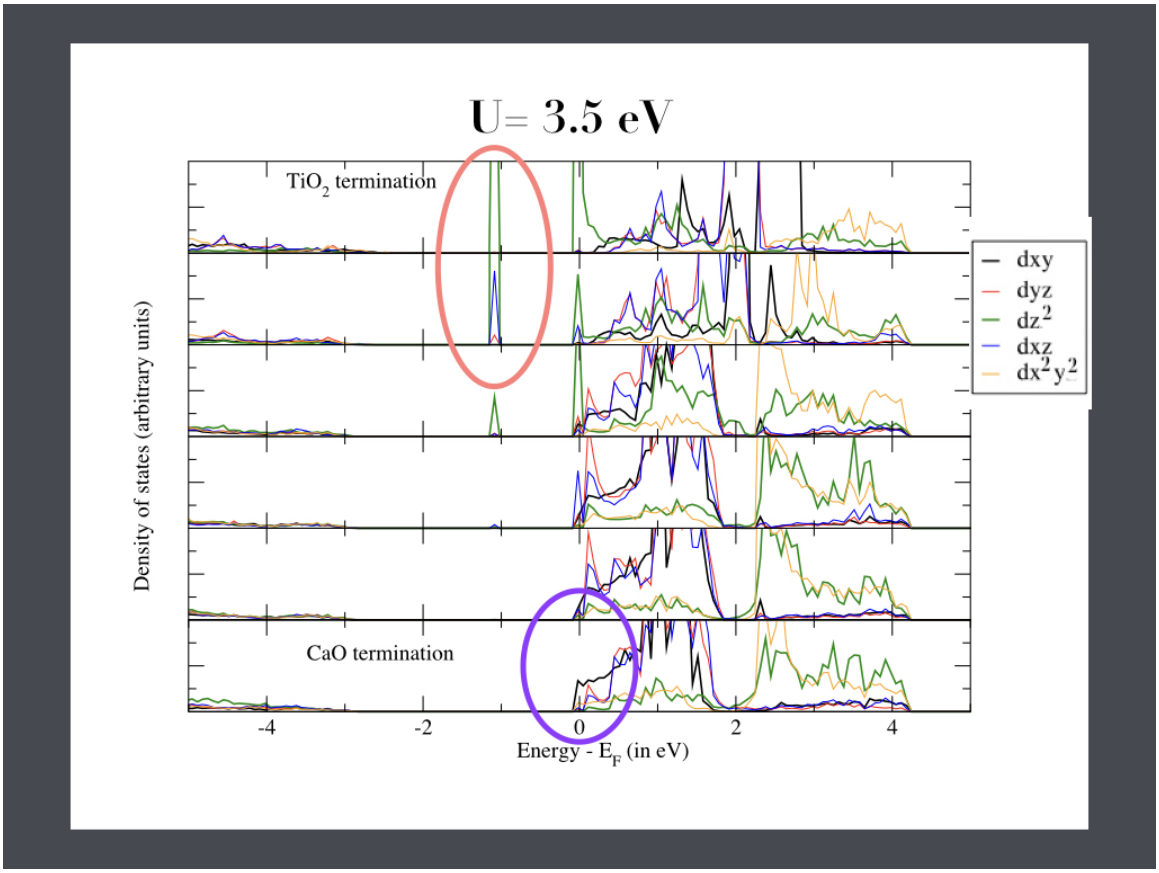

Figure 5.10: The PDOS for the 2 vacancies using U= 3.5 eV is shown. The localised state close to the E_F moves into the conduction band to form the gas. The orbital character of the states is d_{z^2} as is expected for apical vacancies.

has tilts and rotations which make the system more insulating. The difference in the confinement for both STO and CTO also suggests that the filling of the bands will be low and thus that electron-electron correlations (represented by the Hubbard U) will be low. Experimentally in ARPES, there is very little mass re-normalisation for CTO from the bulk which hints at low correlations. The gap at the surface without defects for U=3.5 eV is 0.25 eV less than what is obtained for U=5 eV and this is enough to drive an insulator to metal transition.

Analysis of the PDOS for various values of U - for 5 eV, as shown in Fig 5.10, shows two localised states, one near E_F and another in the gap. These two states lie in the TiO_2 terminated surface and the sub-surface layer. As the value of U is decreased, the state near E_F hybridizes with the conduction band and the bands at the opposite termination (CaO) start getting filled. The optimum filling of the bands corresponding to the lowest d_{xy} bands

observed in experiments and the optimal position of the in-gap state is achieved at U=3.5 eV. The localised state contains two electrons released by the vacancies and the remaining two electrons form the gas. From the PDOS, the lowest d_{xy} band is 60 m eV below the E_F. If now a band structure is plotted, then the orbital character for the lowest CB is found to be at the CaO termination and of a dominant d_{xy} character near Γ and it gradually changes to a d_{z^2} character, showing some hybridization with the localised state found close to E_F. The next band is found to be a mixture of d_{xy} and d_{yz} at Γ and then evolves to a d_{z^2} and then a d_{yz} band. These two bands actually cross at this point where their characters are similar and the crossing occurs between point A and B as shown in Figure 5.11. When compared to the experimental data, the position in energy of the lowest band is off by around 50 meV but the orbital character seems to match. The less dispersive band as seen in ARPES can also be seen here, however the character is a mix between t_{2g} and e_g which is to be expected with the tilting but which is difficult to determine experimentally.

Spin-polarised calculations

If now we add spin-polarisation to the system and allow for magnetic solutions, we find a ferrimagnetic state as compared to a ferromagnetic state found in STO. The initial configuration can be anti-ferromagnetic or ferromagnetic, the Ti atoms close to the vacancy have the maximum magnetic moment. The energy of this state (-900.10 eV) is 1.05 eV lower than the non magnetic solution (-899.05 eV) which is not enough to favour this state so the system might be in a mixed magnetic-non magnetic state (i.e. fluctuating). If the PDOS is analysed, three electrons are found to be localised and one delocalised, filling the conduction band. Out of the three localised electrons, one is at the Ti site with two apical vacancies and the two others are shared over this Ti atom and the one at the TiO_2 termination. Other than the apical Ti, no other Ti atom has any localised electron in either the surface or sub-surface TiO_2 plane. The orbital character of this localised state is again dominant d_{z^2}. The distribution of three electrons over two Ti atoms can be explained in the following way, using Molecular Orbital Theory. Among the two Ti atoms involved, the Ti atom in the surface layer has a lower energy because less apical bonds are broken while for the sub-surface layer, the creation of vacancies means breakage of two apical bonds which

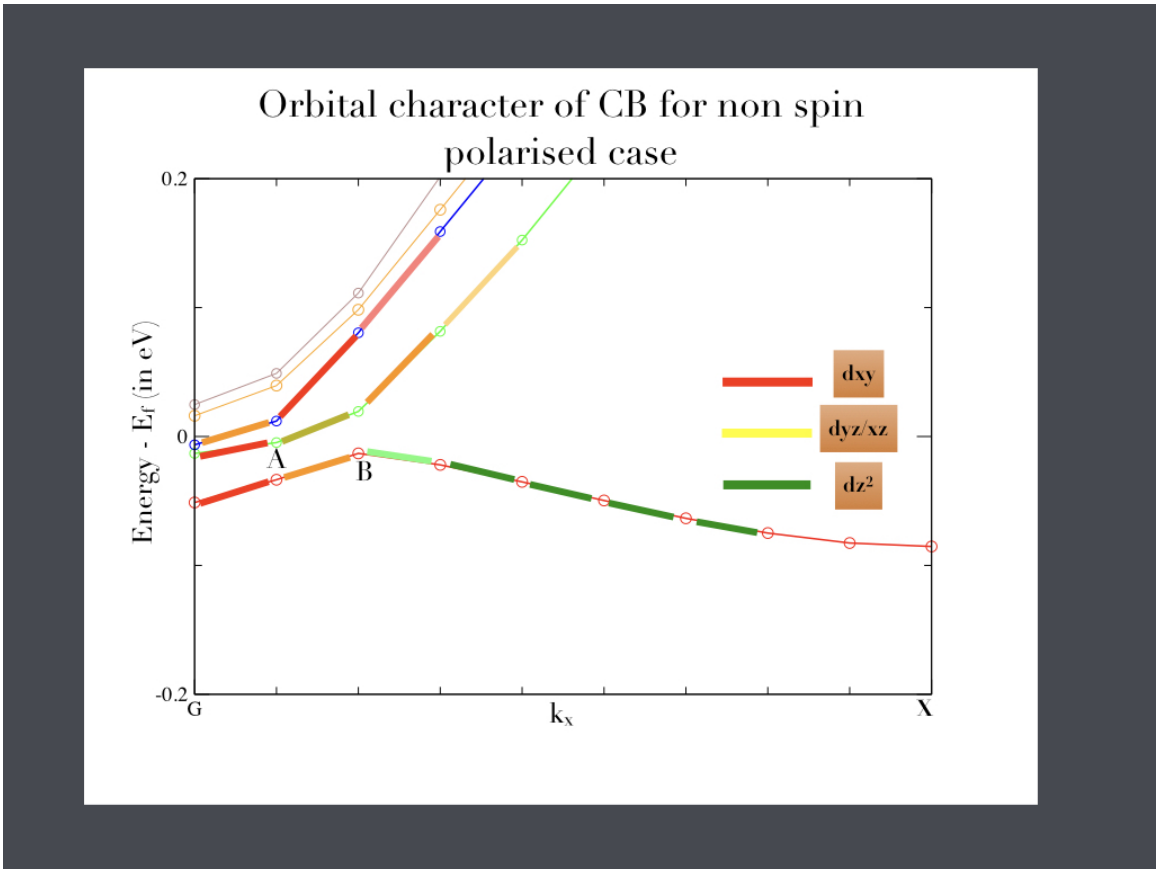

Figure 5.11: The three bands below E_F for U=3.5 eV, sorted according to the energy with their orbital character, are shown. The lowest band begins as a dominant d_{xy} band and quickly changes to a d_{z^2} band indicating a hybridization with a localised state near E_F. The second band begins similarly but changes to a d_{yz}. There is band crossing between these two bands between point A and B.

raises its energy. Then, the two d orbitals of Ti atoms near the vacancy, d1 and d2, form an anti-bonding and bonding orbital as seen in Figs. 5.12 and 5.13, which get one electron each with the same spin and a non-bonding spin on Ti subsurface gets an electron of the opposite spins. The on site Hubbard correlation prevents two electrons of opposite spin to occupy the same site and thus the other two electrons get localised over two Ti atoms. The Hund's coupling maximises the spin over the remaining two electrons. Irrespective of an initial configuration bias, which can be anti-ferro or ferro magnetic, the final configuration is always ferrimagnetic which is contrast with STO which prefers to be ferromagnetic. An artist's representation of the magnetic moments and the spin states of the three localised electrons is shown in Figure 5.13

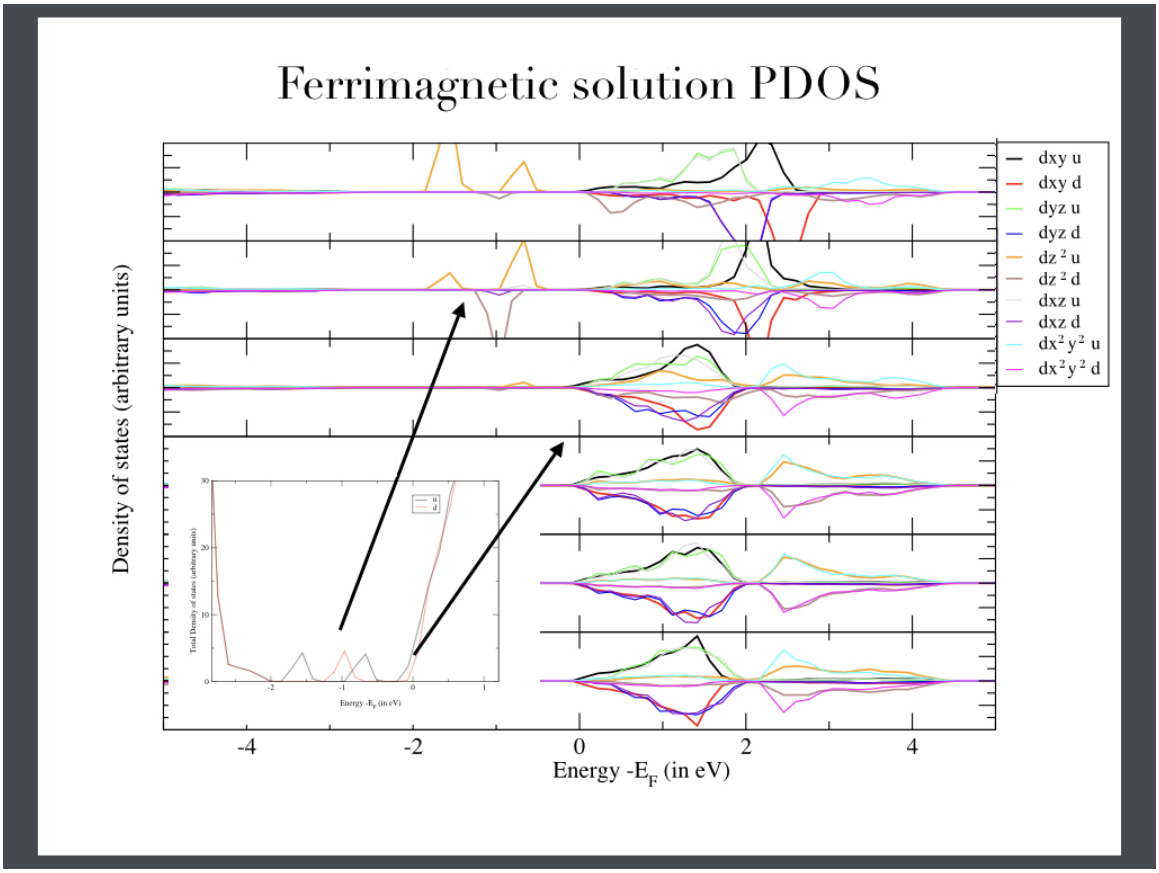

Figure 5.12: The PDOS for initial ferromagnetic configurations are shown and the largest magnetic moments are the one found on the adjacent Ti atoms, Ti 1 and 2, as encircled. The inset shows the total DOS and shows three electrons localised while one electron delocalised in the CB. The system prefers to be in a ferrimagnetic state irrespective of its initial configuration.

The remaining electron is delocalised in the conduction bands and gives rise to a spin polarised gas which has the same spin as the electrons in the bonding and anti-bonding orbitals. Thus, magnetism does not seem to destroy the gas, making it spin polarised instead. However, the gas prefers to live closer to where the vacancy is created. If the band structure is now analysed, the lowest band is found to be at 150 meV below E_F and is of a mixed t_{2g} character which then evolves to a pure $d_{yz/xz}$ character. The next band is of a similar nature while the ones above it are all dominant d_{xy} near the Γ and then begin to change to a $d_{yz/xz}$ character. Although the position in energy of this state below E_F seems to be that seen experimentally, the orbital character of the bands does not seem to match. Since the energies of the spin polarised and non spin polarised systems are very close to

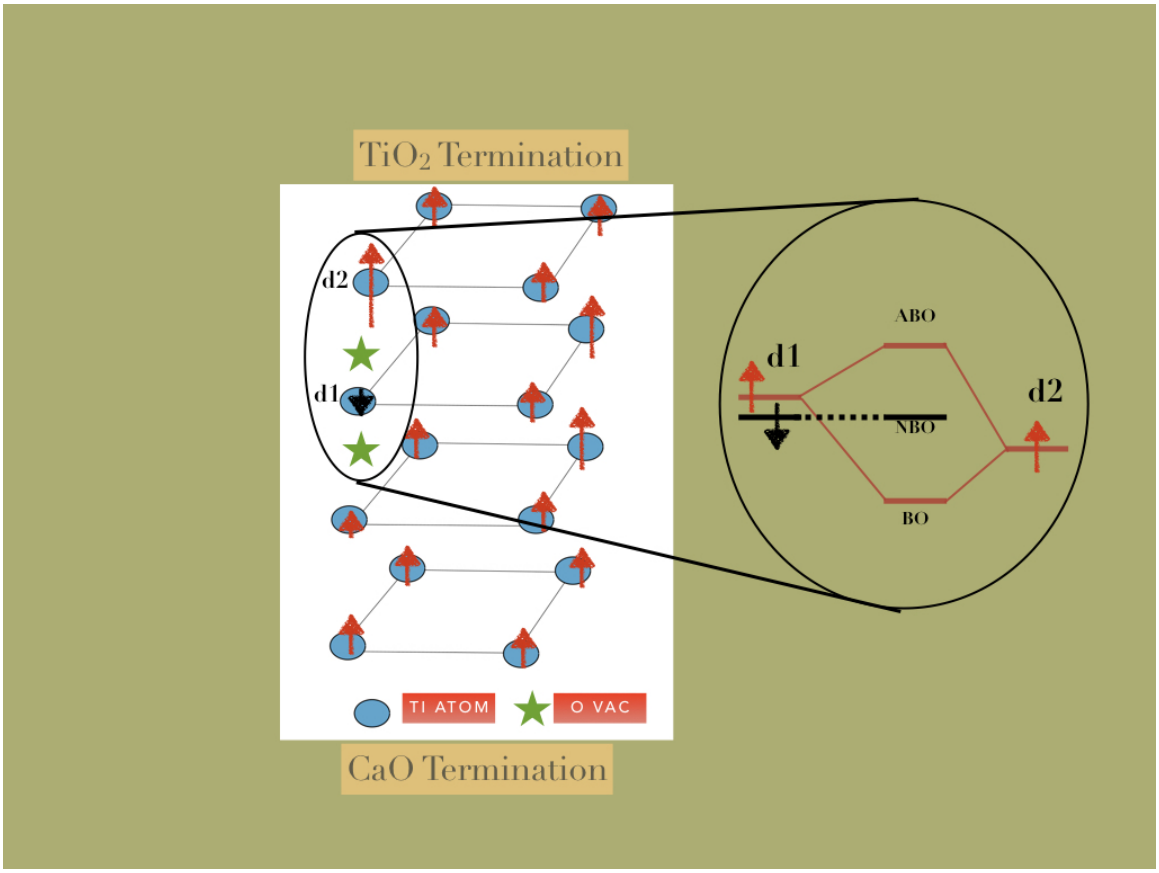

Figure 5.13: An artist's representation of the ferrimagnetic state is shown in the next figure. If the states of the two Ti atoms, denoted by d1 in layer L5 and d2 in layer L6, is investigated, then the electrons occupy one bonding and anti-bonding orbital formed between these two orbitals and a non bonding orbital (shown in inset). Note that two bulk layers, L3 and L2 have been omitted.

each other, the system might prefer one configuration or the other. If the band structures and the PDOS are contrasted for the spin-polarised and non spin polarised calculations, the spin-polarised band seems to give the right location of the CB minimum and the non-spin polarised the right orbital character of the bands. But since both configurations are probable, it is possible that the system prefers a mixture of the two, with ferrimagnetic patches present in a 2DEG. It is also to be noted that this analysis is done for a particular vacancy configuration and in all probability, other vacancy configurations might also exist which might change the orbital character. Preliminary tests done for surface vacancies at the TiO_2 termination in non spin-polarised smaller slabs seem to suggest that the orbital character of the CB and the position in energy matches the experimental values closely while the

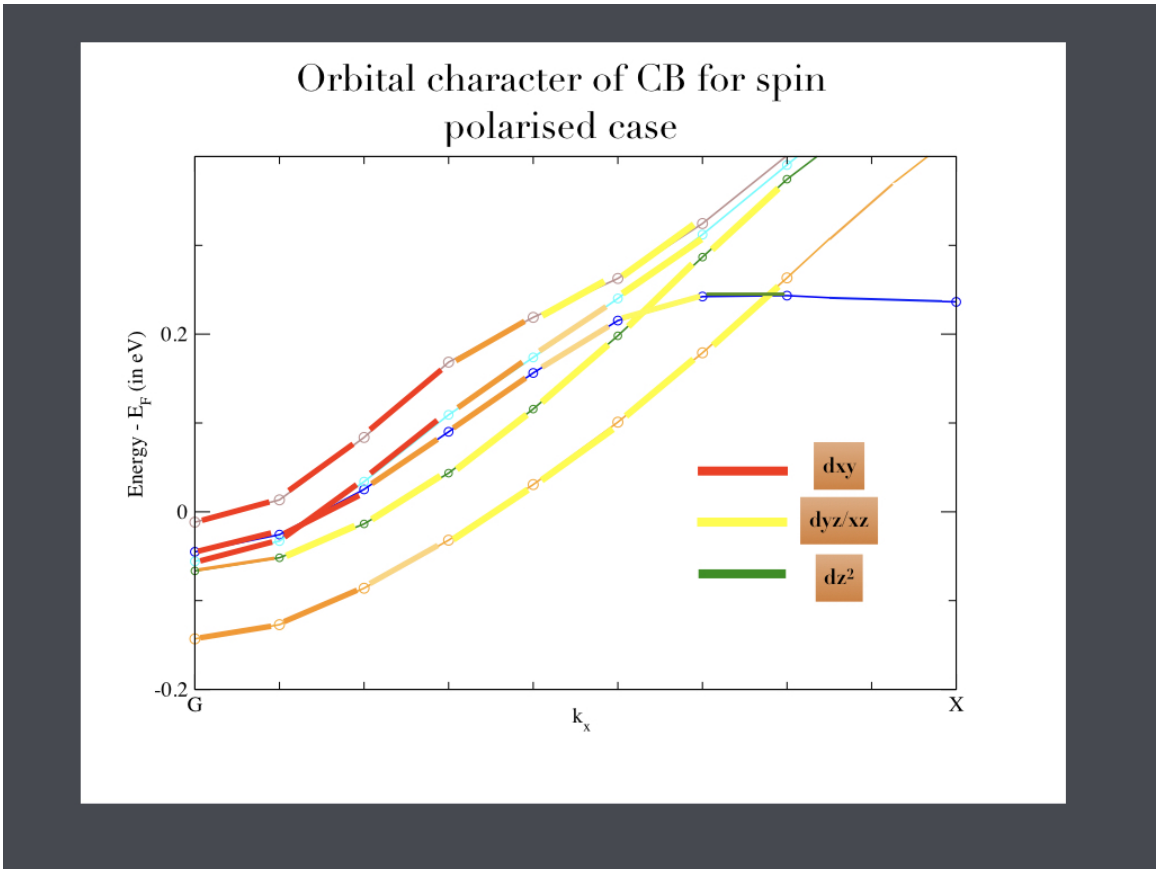

Figure 5.14: The band structure for the spin-polarised calculation is shown here with the bands sorted according to their energies. The lowest CB is at 150 meV below E_F and is of a mixed t_{2g} character and then evolves into a pure $d_{xz/yz}$ character.

localised state is not as visible. It is possible that multiple vacancy configurations also exist at the surface as they are averaged over experimentally. The magnetic state, if it occurs, will also be ferrimagnetic in nature. While, the 2DEG is not destroyed in the presence of magnetism, the gas can become spin-polarised. There is an orbital dichotomy which makes both magnetism and this 2DEG possible in this system as the orbitals involved in the localised moments are primarily d_{z^2} while the gas prefers the d_{xy} or the $d_{xz/yz}$ orbitals. The question of topology still remains an open one as most of the ingredients for a TCI state, like that in the $SrIrO_3$ compound, are present here. In CTO, the tilts and the rotations of the octahedra in all three directions give rise to a anti-ferro distortive structure which is similar to that of $SrIrO_3$ [141]. Even if there is a chance for a small bulk SOC coupling to be present, then the possibility of finding a TCI state is very high.

Chapter 6

Conclusions and Perspectives

The beginning of knowledge is the discovery of something we do not understand.

Frank Herbert

In this thesis, we have tried to show that transition metal oxides (TMOs) can become an interesting playground for topological physics. TMOs are already known to be multi-functional and topology could be an interesting feather to add to its cap. In the first chapter, we discuss a fascinating oxide, $SrTiO_3$ (STO) which is known to be an insulator in the bulk and yet contains a metallic state pinned to its surface. We showed that if a theoretical modelling is done based on the band dispersion and Fermi surface seen in ARPES, one finds three band crossings. At these points, all three t_{2g} bands having equal energy and thus, any perturbation added to the model, should have lifted this degeneracy. We showed that these points are stable with respect to bulk spin-orbit coupling and in the presence of an Orbital Mixing (OM) term, leads to band inversions. We further showed that this OM term is of a Rashba-like form and can lead to the spin windings and even topological edge states. This model could also be applied to a heterostructure of $LaAlO_3/SrTiO_3$ as well since it has a metallic state at the interface of the two constituent materials of a similar nature. Similar spin windings and topological edge states are then predicted.

While the surface proved to be an interesting beast on its own when compared to the bulk, there are still mysteries to be understood. For example, surface rumplings, which try to compensate for the polarity of the surfaces, inadvertently play a part in removing the degeneracy of the bulk bands and also introduce the necessary element for band inversion. But could there be other effects hitherto not thought of? For example, defects or vacancies are seen to be important players in creating a confinement potential in the case of STO but in the case of LAO/STO, this is just one of the possible mechanisms at play. Could there be a way to distinguish the vacancies as the sole mechanism responsible for the gas? [142, 16]

In LAO/STO, there exists another interesting line of thought- addition of capping layers to reduce the number of LAO layers required to create the metallic state. Ab-initio studies have shown that using metallic capping layers can make this possible [143]. Experimental work has already been done in this direction by using capping layers of metals to reduce the

number of LAO layers required, albeit for the purpose of making spin pumping effective to make possible spintronic devices [144, 145], One of the mecanisms proposed to explain this phenomena is the oxidation of the metal capping layer. The metal present will oxidise itself by sucking oxygen out of the LAO layer, thus creating vacancies in the topmost LAO layer, liberating electrons which then form the 2DEG. This neat idea has already been used in the case of the (001) STO surface by Santander et al to create the 2DEG [83]. Instead of using metals, another idea is to use layers of STO as capping layers. In order to explore this line of thought, we are trying to work on capping layers of STO, which translates into using STO twice, once as a substrate and another as the capping layer itself. Preliminary experiments have shown that such a scenario is indeed possible [146] where only 4 unit cells are needed (n of LAO and m of capped STO where n+m=4). Preliminary DFT studies however do not find this behaviour and seem to suggest insulating behaviour for 1 unit cell thick LAO capped with STO. The origin of this behaviour as to why STO is an effective means to reduce the number of LAO layers needed, should be studied further, by the means of ab-initio studies and it is possible that surfaces or interfaces might again play an important role. And where surfaces or interfaces enter, topology again might manifest itself which could be another avenue to be explored.

Once ab-initio studies have been done, a tight binding analysis might show that topological states might exist. However, the nature of the topological states need to be explored further - on the surface of STO itself, we have shown that there are Dirac points where the band inversions take place. They are four by symmetry and come in pairs of time reversal symmetric partners. The topological states which exist over the Brillouin Zone (BZ) can be both between points B and D or B and $B^{'}$ of Figure 6.1 and it could be interesting to explore the stability of the two and whether they reinforce each other or not. The coupling of these two symmetries could also be explored and their effects on the nature of the topological states could be a future study. The experimental detection of these topological states remains a challenge and it would be interesting to see the development of these thought experiments into physical ones.

Apart from the (001) orientation, there are other interesting orientations which show a 2DEG and strange transport properties. As shown in Chapter 4, increasing the carrier

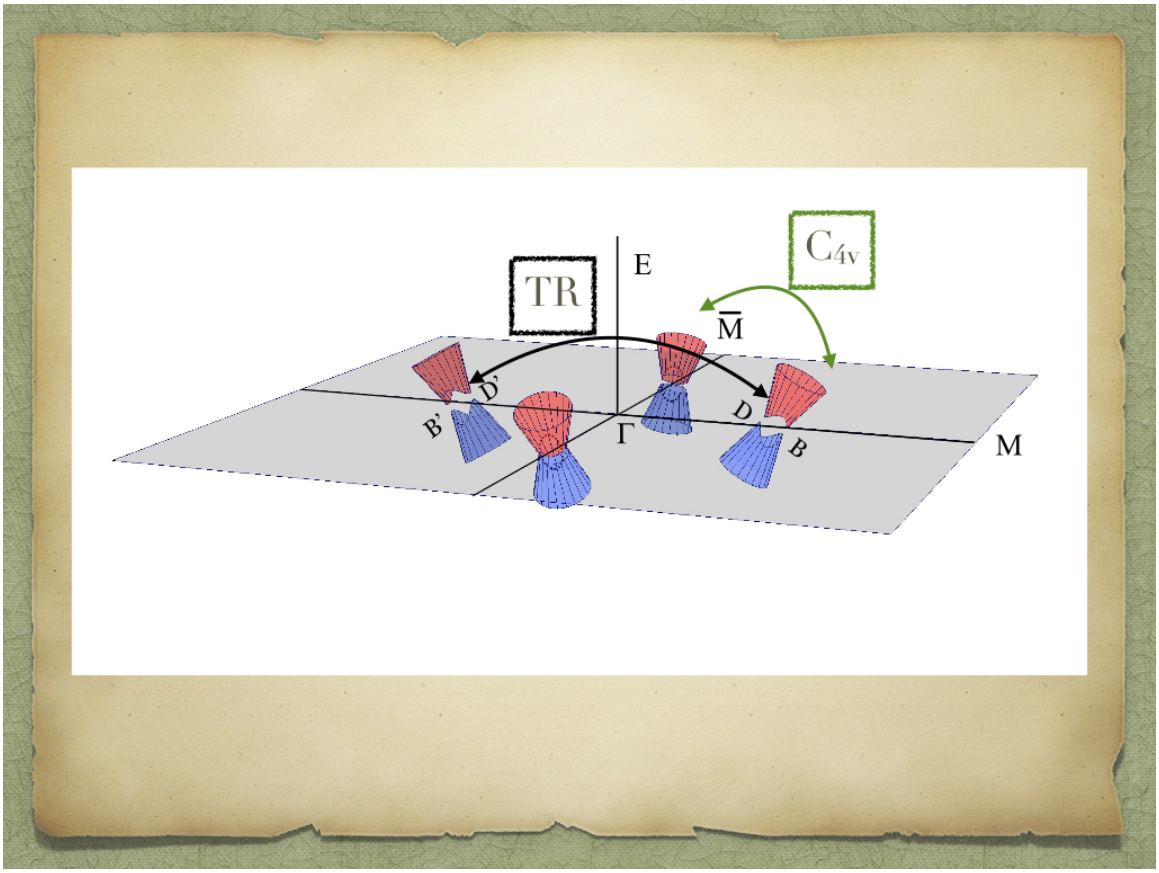

Figure 6.1: An artist's view of the tilted and gapped Dirac cones shown across the Brillouin Zone.The points B and D are the points between which topological states might exist but they also might exist across the BZ between B and B′. Adapted from [79]

.

concentration in the (111) oriented surface of LAO/STO via gating of the sample results in firstly, one band getting populated and next, a second band to start appearing. However, the population of the second band increases at the expense of the first band which is odd to say in the least. An explanation based on Hubbard U type correlations has been proposed as the number of carriers added could contribute to increasing electron-electron correlations. A tight binding method is applied first to understand the different energy scales that might be present in the (111) orientation, including the kinetic energy, the bulk spin-orbit coupling (SOC) or the trigonal field (TF). Next using Poisson-Schrödiner (PS) calculations, we show that the confinement potential induces a sub-band structure and two sets of sub-bands seem to lie close to the Fermi energy E_F. Then correlations in the form of

the Hubbard U between orbitals of like and unlike nature are added in a self-consistent approach to determine the populations of the sub-bands. A more sophisticated self-consistent method could be used which does not use the rigid band model used by tight-binding but instead uses Poisson-Schrödiner (PS) calculations. This could be a way to firstly identify the point where the band inversion occurs and could also verify the inversion of the populations of the sub-bands. It could also be a more accurate way of predicting the band structures arising from such population inversions. The band inversions will be important in the topological effects as topology in these systems can be twofold, one arising from the band inversion seen at the three band crossings similar to Chapter 3 or another arising from the parity of the wave functions similar to KTO (111) [35].

In the next chapter, we have shown that in $CaTiO_3$ (CTO), there can also exist a metallic state via ab-initio studies. This is a neat verification of the experimental ARPES measurements which predict that a 2DEG should exist also for CTO with slightly different characteristics than the gas found in STO. We show that for a particular vacancy configuration and a particular value of the Hubbard correlations, U, one can find both a localised vacancy state and filled conduction bands consisting of delocalised electrons. We have also showed that in the presence of magnetism, there exists a ferrimagnetic state and the 2DEG becomes spin-polarised.

In the above systems, there is an interplay between the extent of localisation and delocalisation with the vacancies localising certain electrons and yet releasing certain others to form a delocalised state. To understand this better, orbital dichotomy has been proposed, in the case of ab-initio findings in both STO [106] and $CaTiO_3$ (CTO). Orbital dichotomy plays a very important role in segregating the orbitals which are involved in localised or delocalised states, with the t_{2g} orbitals being the epicentre of delocalised electrons in the conduction band, and e_g states having the localised electrons all to themselves. However, this could depend on the type of vacancies created and needs to be investigated further. Moreover, since experiments like ARPES average over all vacancy configurations, it would be interesting to see what is the final vacancy state of the system. An in-depth study of the possible vacancy configurations could be done in the case of CTO as well which could enlighten us on this issue. Another question arises when discussing the insulator to

metal transition, the value of the Hubbard U used and alternate methods like DMFT+U or DMFT+LDA could validate a particular range of values of U used in DFT calculations.

Another very important issue raised is that of magnetism and its impact on the metallic state and on the possible topological signatures. The report of magnetism at the surface of STO raises the issue of the stability of the topological state to time reversal symmetry breaking but from an experimental standpoint, the claim of magnetism is still debatable [103][72][104][105]. If a purported ferromagnetic exchange splitting affected the t_{2g} carriers, that would be detrimental to the topological edge states observed. A possible way out of this dilemma could be to invoke orbital dichotomy and allocate the magnetic behaviour to the localised orbitals while leaving the delocalised states in the conduction band become spin-polarised. But in CTO, the magnetic state is ferrimagnetic as compared to ferromagnetism in STO which might again impact the topological states, which could be the focus on future studies. In fact, if now a tight binding model can be made for the CTO surface, then the possibility of exploring the topology becomes real.

In all, TMOs can manifest very unique topological properties and can show both kinds of topologies, be it spin-orbit driven or of the topological crystalline insulator kind. They should be the focus of future studies to add yet another jewel to the crown of multifunctionality which these oxides bear.

Chapter 7

Appendices

7.1 Appendix A : Details of the tight binding Hamiltonian for $SrTiO_3$

7.1.1 Eigenstates in the absence of the Orbital mixing term

In the bulk, the Hamiltonian can be modeled by three tight-binding bands in the basis of the t_{2g} manifold, $|xy\rangle, |yz\rangle, |xz\rangle$. Once spin-orbit coupling is added in the bulk, the spin and orbital degrees of freedom are locked and the Hamiltonian can be re-arranged to take a block-diagonal form. The two blocks are related by time-reversal symmetry and they can then be represented in the basis of $|xy;\downarrow\rangle, |yz;\uparrow\rangle, |xz;\uparrow\rangle$ and its time reversed partner. The spectrum in the first quadrant of the BZ, near Γ_{dp}, is plotted in Fig. 1 showing three bands, each doubly degenerate. The three eigenvalues, denoted by E_b, E_c, E_d, are arranged in increasing order of the energy; the first two form the tilted Dirac cones while the last one is the higher band. The tilt of the cones can be removed before the addition of orbital mixing. The highest energy band can be projected out in order to restrict ourselves to the low energy states. The Hamiltonian is then reduced to a block diagonal form with the upper block consisting of eigenvectors corresponding to energy E_b, i.e. $|B\rangle$ and its time reversed partner $|B^*\rangle$ and a lower block corresponding to the energy E_c with eigenvectors $|C\rangle$ and its time reversed partner $|C^*\rangle$. $|B\rangle$ and $|C\rangle$ can be represented as a linear combination of all three d orbitals and can be formally noted as

$$|B\rangle = a_1 |xy;\downarrow\rangle + b_1 |yz;\uparrow\rangle - ic_1 |xz;\uparrow\rangle \tag{7.1}$$

$$|C\rangle = a_2 |xy;\downarrow\rangle + b_2 |yz;\uparrow\rangle - ic_2 |xz;\uparrow\rangle , \tag{7.2}$$

where a_1, b_1, c_1, a_2, b_2 and c_2 are real functions of k.

7.1.2 Eigenstates in the presence of the Orbital mixing term

Two approaches can be used to model the spectrum and the eigenstates. One consists of a perturbative approach that mostly uses two bands at a time to add orbital mixing in

two steps, and another which is a variational approach detailed in the next section. The first approach is applied in a couple of steps. First we write down the Hamiltonian in the basis of $|B\rangle$,$|B^*\rangle$,$|C\rangle$ and $|C^*\rangle$

$$\begin{bmatrix} E_b & R_1^* & 0 & 0 \\ R_1 & E_b & 0 & 0 \\ 0 & 0 & E_c & R_2^* \\ 0 & 0 & R_2 & E_c \end{bmatrix}, \tag{7.3}$$

where $R_1 = 4ga_1[i\sin(k_x)b_1 + \sin(k_y)c_1]$ and $R_2 = 4ga_2[i\sin(k_x)b_2 + \sin(k_y)c_2]$. Degenerate perturbation theory can then be applied to each of the blocks and would cause the cones to become split into bonding and anti-bonding branches, while adding a phase to each of these branches. The split cones now begin crossing at fixed points ABCD as shown in Fig. (2). The eigenvectors of (7.3) take the form

$$\text{BO}_\text{b} = \frac{ie^{-i\psi_1}}{\sqrt{2}}|B\rangle + \frac{1}{\sqrt{2}}|B^*\rangle \equiv |B_B\rangle \tag{7.4}$$

corresponding to $E_b - |R_1|$ and

$$\text{ABO}_\text{b} = \frac{-ie^{i\psi_1}}{\sqrt{2}}|B^*\rangle - \frac{1}{\sqrt{2}}|B\rangle \equiv |AB_B\rangle \tag{7.5}$$

for $E_b + |R_1|$. Similarly we have bonding and anti-bonding orbitals of the same character for the subspace spanned by $|C\rangle, |C^*\rangle$,

$$\text{BO}_\text{c} = \frac{ie^{-i\psi_2}}{\sqrt{2}}|C\rangle + \frac{1}{\sqrt{2}}|C^*\rangle \equiv |B_C\rangle \tag{7.6}$$

for $E_c - |R_2|$ and

$$\text{ABO}_\text{c} = \frac{-ie^{i\psi_2}}{\sqrt{2}}|C^*\rangle - \frac{1}{\sqrt{2}}|C\rangle \equiv |AB_C\rangle \tag{7.7}$$

for $E_c + |R_2|$. The phases ψ_1 and ψ_2 are given by $\tan(\psi_1) = c_1\sin(k_y)/b_1\sin(k_x)$ and $\tan(\psi_2) = c_2\sin(k_y)/b_2\sin(k_x)$. The spin texture for a particular phase can then be modelled by a two component vector. For phase ψ_1 the two components are

$(-2ga_1c_1\sin(k_y)/\sqrt{2}|R_1|, 2ga_1b_1\sin(k_x)/\sqrt{2}|R_1|)$. Similarly, the spin texture for the

other phase ψ_2 can also be calculated. The phase ψ_1 is shown for a constant energy contour which cuts two branches of the energy, as seen in Fig. 3 of the main text. We also find that $\psi_1 = -\psi_2$ with their branch cuts extending from Γ_{dp} to M and from Γ to Γ_{dp}. Secondly, the orbital mixing term which gaps out the split Dirac cones is added and the Hamiltonian takes the following form in the basis of $|B_b\rangle, |AB_c\rangle, |B_c\rangle$ and $|AB_b\rangle$

$$\begin{bmatrix} E_b - |R_1| & -2g\sin k_y\beta_{ac} & w^*\beta_{ab}\sin k_x & 0 \\ -2g\sin k_y\beta_{ac} & E_c + |R_2| & 0 & -w^*\beta_{ab}\sin k_x \\ w\beta_{ab}\sin k_x & 0 & E_c - |R_2| & -2g\sin k_y\beta_{ac} \\ 0 & -w\beta_{ab}\sin k_x & -2g\sin k_y\beta_{ac} & E_b + |R_1| \end{bmatrix} \tag{7.8}$$

where $w = -2ge^{-i\psi_1}$. With the matrix elements given in Hamiltonian (7.8) and that the unperturbed energies of the bonding and the anti-bonding orbitals, the perturbed energies take the following form

$$\begin{aligned} \tilde{E}_{AB_b} &= E_b + |R_1| + \tfrac{4g^2\delta^2}{\Delta E + |R_1| + |R_2|} + \tfrac{4g^2\eta^2}{\Delta E + |R_1| - |R_2|}, \\ \tilde{E}_{B_b} &= E_b - |R_1| + \tfrac{4g^2\delta^2}{\Delta E - |R_1| - |R_2|} + \tfrac{4g^2\eta^2}{\Delta E - |R_1| + |R_2|}, \\ \tilde{E}_{AB_c} &= E_c + |R_2| - \tfrac{4g^2\delta^2}{\Delta E - |R_1| - |R_2|} - \tfrac{4g^2\eta^2}{\Delta E + |R_1| - |R_2|}, \\ \tilde{E}_{B_c} &= E_c - |R_2| - \tfrac{4g^2\delta^2}{\Delta E + |R_1| + |R_2|} - \tfrac{4g^2\eta^2}{\Delta E - |R_1| + |R_2|}, \end{aligned} \tag{7.9}$$

where $\delta = \beta_{ac}\sin(k_y)$, $\eta = \beta_{ab}\sin(k_x)$, $\Delta E = E_b - E_c$, $\beta_{ab} = a_2b_1 + b_2a_1$ and $\beta_{ac} = a_1c_2 + c_1a_2$. At the crossing points ABCD, the energy values obtained above in Eqs. (7.9) start diverging as the energy gap between the two bands becomes zero. At these points only two bands cross at a time and degenerate perturbation theory needs to be applied again to get an analytic handle on the energies. A comparison between the perturbed and the numerical energy values can be seen in Fig. 7.1 where the black dots denote the data points generated by the perturbative approach while the solid bands signify the numerical data. The perturbation theory shows a good agreement with the numerical values away from the region containing the points ABCD.

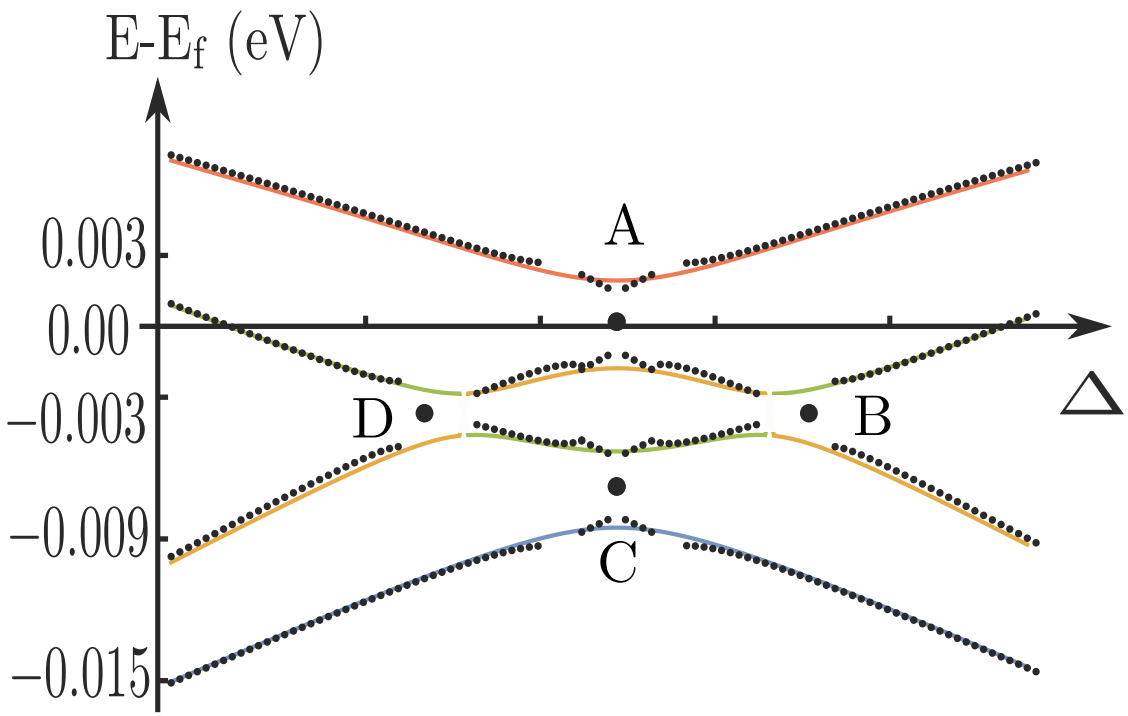

Figure 7.1: The energies as calculated in Eqs. (7.9) are shown as black dots which are then overlaid on the numerically calculated bands as shown in earlier figures.

The eigenstates and the phase ψ can also be calculated in a similar fashion. The phase ψ gets renormalised at the crossing points and will no longer be quantized as one goes around the Dirac point. Again at the avoided crossing points ABCD, degenerate perturbation theory will have to be applied, involving two bands at a time, to get the correct value of the phase. The variations of β_{ab} and β_{ac} as one goes around the DP can be seen in Figure 7.2 as well as the variations of the phase. At the x-axis, is the variation in the angle as one goes around the Dirac point and on the y-axis are arbitrary units to define the magnitude of the coefficients. For $\theta = \pi/4$ or for the $k_x = k_y$ direction, both β_{ab} and β_{ac} go to zero and hence in this direction, one sees no band inversion. The variation of $b_1/c_1(b_2/c_2)$ explains the branch cut seen in the phase below (above) the DP. Above (below) the DP, the point of inflexion for the phase is at $\pi/4(3\pi/4)$ and is seen as a branch cut with the phase winding from positive to negative as one increases θ.

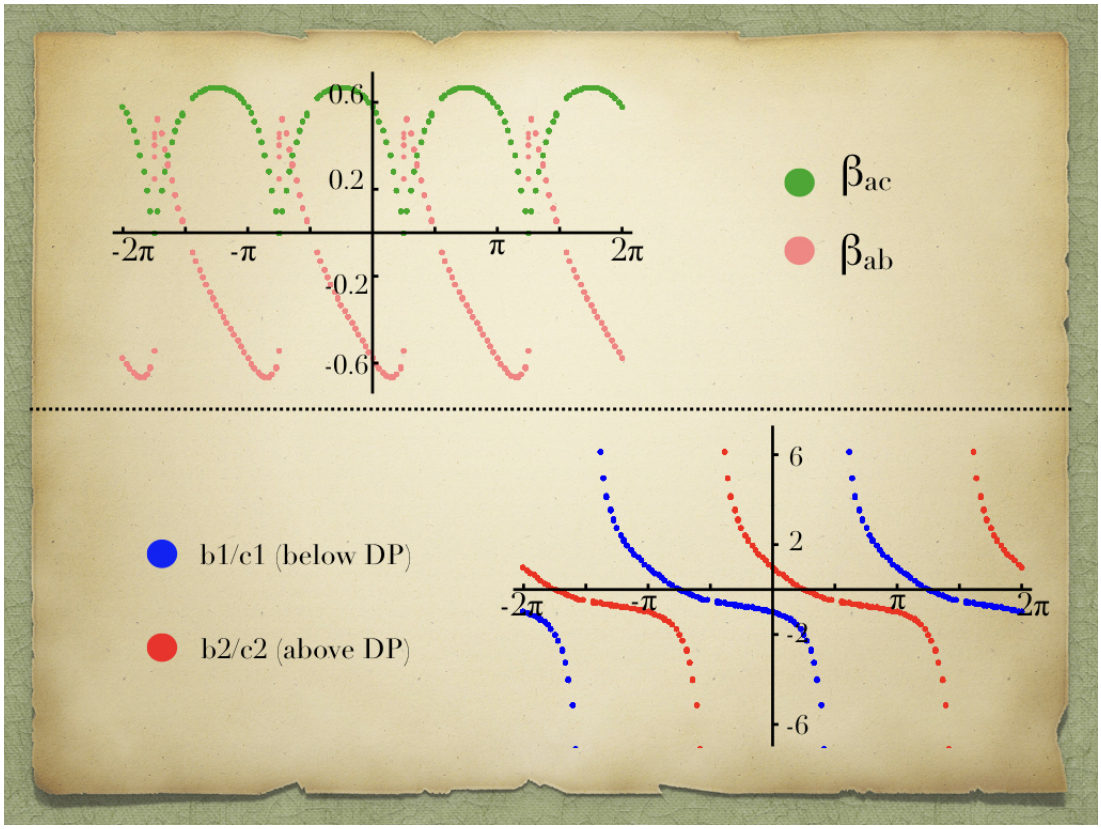

Figure 7.2: Upper panel, the form of the coefficients β_{ab}, β_{ac}. Lower panel, the ratio of the coefficients of the eigenvectors of the spin-orbit coupled basis below and above the DP.

7.2 Appendix B : Spin-textures LAO/STO $(0\,0\,1)$

If a tight binding modelling is done, using the ARPES data derived from [93], then Hamiltonian similar to Eq. 27 from Chapter 3 is obtained with different hopping parameters. Excellent fitting of the ARPES energy dispersion curves is obtained with a = 3.90 Å, t_1 = 0.356 eV, t_2 = 0.033 eV, λ = 0.025 eV, g = 0.005 eV and $\epsilon_1 - V_0$ = -0.091 eV (2nd dxy band) and g = 0:005 eV , $\epsilon_2 - V_0$ = -0.05 eV for $d_{yz/xz}$ bands. Poisson-Schrondiger calculations have been done to precisely calculate the shift of the heavy and light bands for a filling of 2.5 $\times 10^{14}$ cm^{-2}. The band structure in the vicinity of the crossing point in two directions ΓM and Δ perpendicular to it, with the orbital mixing term added looks like the split and gapped spectrum seen in Chapter 3 for the case of STO (001). The band structure is seen in the Figure 7.3

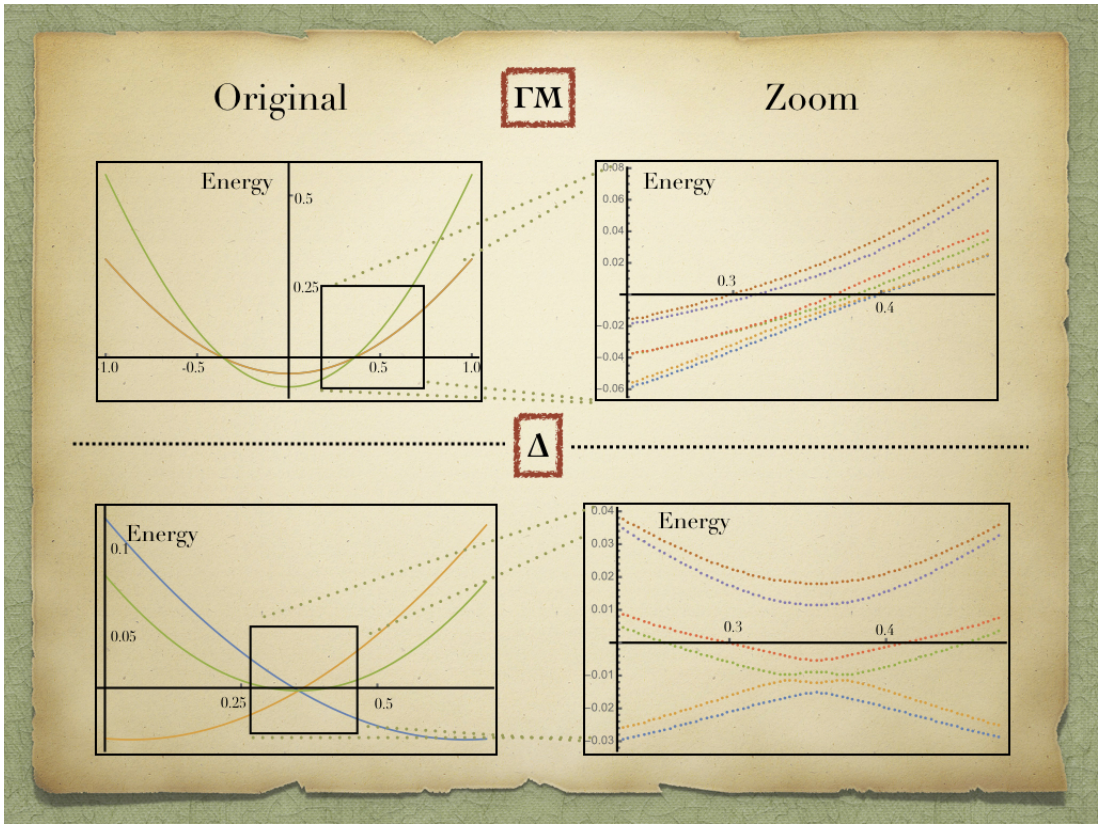

Figure 7.3: The band structure for LAO/STO are shown after a tight binding modelling in the ΓM direction and direction Δ perpendicular to it. The addition of OM gives the same split and gapped spectrum as observed in the case of STO (001) seen in Chapter 3.

If now a similar tight-binding modelling is done on the pertinent bands, a similar phase will accumulate and the following spin textures shall be seen near the DP with a similar winding as can be seen in Figure 7.4

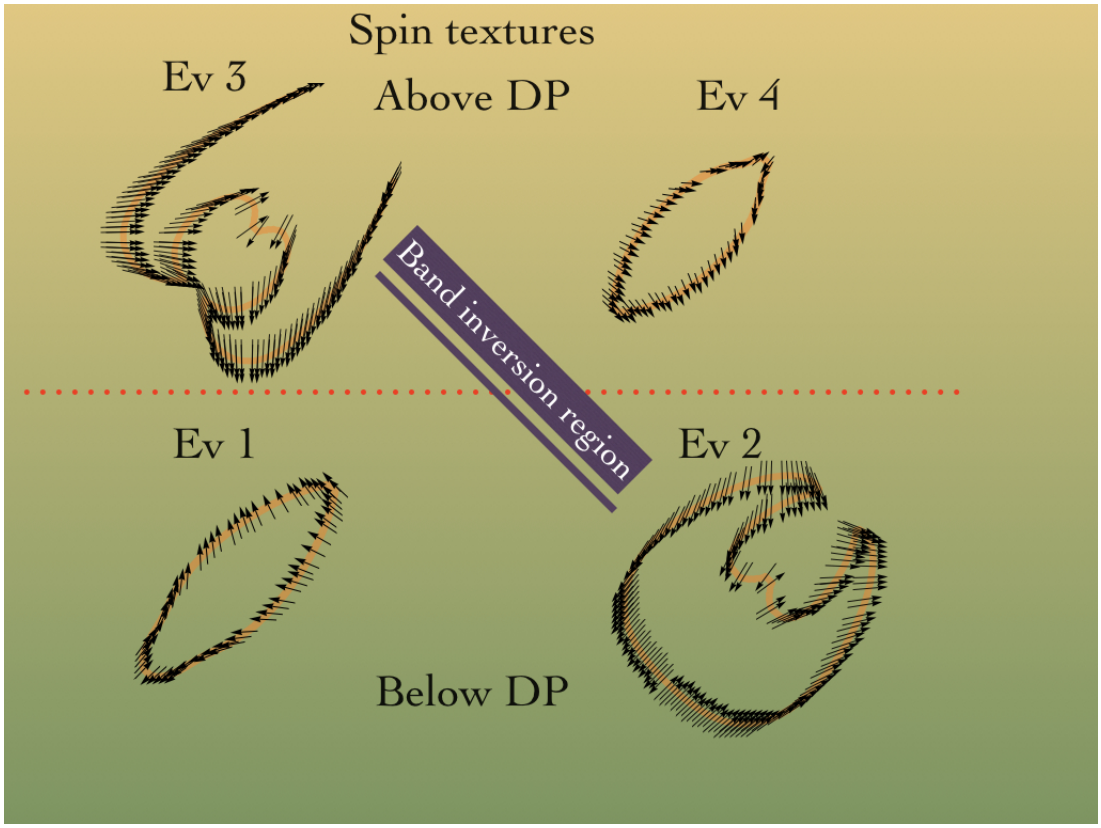

Figure 7.4: The spin textures for LAO/STO are shown after a tight binding modelling. There are four energy contours, two above and two below the DP, showing exactly similar spin textures as that in STO.

7.3 Appendix C : Multi-band Magneto transport

7.3.1 Hall constant for the multi-band case

From the PS modelling of the tight-binding dispersions, we inferred that within the experimental range of back-gate voltages, two energy sub-bands are occupied, the lower one yielding a manifold of three bands and the upper one a group of three bands as well. In using an Ohmic description of transport, each of these bands acts as a current carrying channel and overall the system is equivalent to a parallel network of resistors R_n, $n = 1, ..., 6$.

Accordingly, $R^{-1} = \sum_n {R_n}^{-1}$ for the total resistance R. In 2D, a similar expression holds for the resistivities ρ, ρ_n, and we have

$$\rho^{-1} = \sum_n {\rho_n}^{-1} \tag{7.10}$$

From the Drude theory of transport we determine the conductivities σ_n of the channels from which we deduce ${\rho_n}^{-1} = \sigma_n$.

$$\sigma_n = \left[\begin{smallmatrix} A_n & B_n B \\ -B_n B & A_n \end{smallmatrix} \right]. \tag{7.11}$$

Where, in the presence of a a magnetic field B, $A_n = \frac{\sigma_{0,n}}{[1+(\mu_n B)^2]}$, $B_n = \frac{\sigma_{0,n}\mu_n}{[1+(\mu_n B)^2]}$. Here, $\sigma_{0,n}$, μ_n denote the zero field conductivity and mobility of channel n, respectively.

Using Eq.(7.10), we get

$$\rho^{-1} = \left[\begin{smallmatrix} \sum_n A_n & \sum_n B_n B \\ -\sum_n B_n B & \sum_n A_n \end{smallmatrix} \right]. \tag{7.12}$$

Inverting the 2×2 matrix gives the resistivity of the network and hence the total resistance R. The diagonal entries are the component of the longitudinal magneto-resistance and the off-diagonal terms yield the Hall constant R_H

$$R_H = \frac{\sum_n B_n}{(\sum_n A_n)^2 + (\sum_n B_n B)^2} \tag{7.13}$$

In the high field limit ($\mu_n B >> 1 \equiv \emptyset_c \tau_n >> 1$, for *all* n), the total carrier concentration is the sum of the carrier concentrations of all the bands (these are all electron-like states).

In the zero field limit, we find that

$$R_H = \frac{\sum_n -e\ n_{2D,n}(\mu_n)^2}{\sum_n (-e\ n_{2D,n}\mu_n)^2} \tag{7.14}$$

where $n_{2D,n}$ is the carrier density in band n.

7.3.2 Modeling the experimental data

As mentioned in the previous subsection, two sub-bands become populated as the back-gate voltage is increased within the experimentally accessible range. For the lower energy sub-band, two bands have higher carrier concentrations for a given value of the Fermi energy E_F. These correspond to carriers spatially located close to the interface and hence we consider that their mobilities are at least one order of magnitude smaller than those of the rest. Within that manifold, Figure 1 (c) from Ch 4 shows that the population of band 2 or n_1 versus E_F has a non monotonic variation. We ascribe to this band a mobility μ_1 approximately given by the experimental data Figure 1(d) from Ch 3. The mobilities of the remaining band in that manifold is very small and it does not contribute significantly to the Hall constant R_H. One state in the higher energy sub-band is populated within the range of E_F relevant for experiments which is band 6 or n_2. Its mobility is chosen to be approximately a factor of two smaller than the experimentally estimated value. The other two states are not populated for the range of gate voltages considered. We input the theoretical data into Eq.(7.13) which leads to Figure 7.5. We set the starting and end values of E_F to the appropriate experimental back-gate voltages.

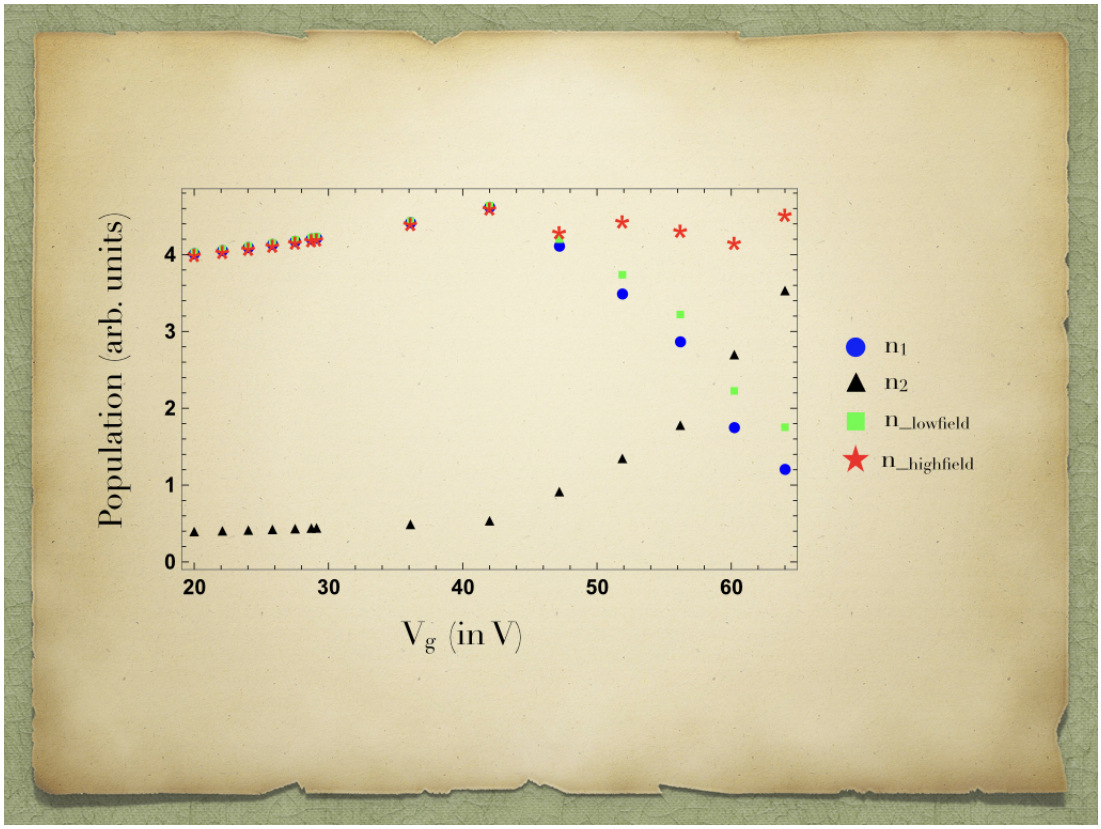

Figure 7.5: The populations for sub-band 1 n_1 (blue circles) and sub-band 2 n_2 (black triangles) is shown along with the total population of the sub-bands at low field (green squares) and high field (red stars). As soon as the population of sub-band 2 becomes zero, the sum of the total population starts deviating from n_1 even though the mobility of n_2 is low.

7.4 Appendix D : Density Functional Theory

Density Functional Theory (DFT) is an ab-initio method which tries to resolve an N-body problem, difficult to solve analytically. To do this in a finite time, numerous approximations are used and this section will explain the ones which are most commonly used.

7.4.1 Born-Oppenheimer approximation

The basic idea in quantum mechanics to understand the properties of the system revolves around the solution of the Schrödinger equation. In solid-state physics, it boils down to solving this equation for a system of N atoms-N electrons and N nuclei.

$$\begin{aligned}\Bigg(-\sum_i \frac{\hbar^2}{2m_e}\frac{\partial^2}{\partial \vec{r_i}^2} - \sum_I \frac{\hbar^2}{2M_I}\frac{\partial^2}{\partial \vec{R_I}^2} \\ + \frac{e^2}{2}\sum_{i\neq j}\frac{1}{|\vec{r_i}-\vec{r_j}|} + \frac{e^2}{2}\sum_{I\neq J}\frac{Z_I Z_J}{\left|\vec{R_I}-\vec{R_J}\right|} + \frac{e^2}{2}\sum_{i,I}\frac{Z_I}{\left|\vec{r_i}-\vec{R_I}\right|}\Bigg)\left|\Psi^\alpha(\vec{r},\vec{R})\right\rangle \\ = E_\alpha(\vec{r},\vec{R})\left|\Psi^\alpha(\vec{r},\vec{R})\right\rangle \end{aligned} \tag{7.15}$$

where $e^2 = \frac{q_e^2}{4\pi\epsilon_0}$ and q_e is the charge of an electron, m_e and M_I are the masses of the electron and the nuclei respectively. $\vec{r_i}$ denotes the position of the electrons while $\vec{R_I}$ denotes the position of the nucleus respectively and Z_I is the atomic number of the nucleus. $\left|\Psi^\alpha(\vec{r},\vec{R})\right\rangle$ is the N body wave function with the index $\alpha \in (1, N)$ denoting the number of eigenvalues and E_α corresponds to the αth eigenvalue.

The first two terms denote the kinetic energy of the electron and the nuclei respectively and the next three terms denote the Couloumb interactions, the first of the three being the electron-electron interaction, the second the inter-nuclei interaction and the last showing the interaction between electrons and the nuclei.

The solution of such an equation is not easy because it involves a wave function of N electrons and nuclei which are correlated among themselves. The most impacted by these correlations are the valence electrons and the electrons in a solid behave very differently than those in free atoms. The Born-Oppenheimer (BO) approximation tries to make this

problem simpler by assuming the nuclei are almost immobile compared to the rapid motion of the electrons, which are much lighter than the nuclei. This translates into approximating that the electronic state of the electrons relaxes to its ground state configuration after each step of ionic motion. This results in the separation of the wave function into an electronic and an ionic part corresponding to the nuclei. $\Psi(\vec{r},\vec{R}) = \Phi(\vec{R})\psi(\vec{r})$. In the first step, the nuclear kinetic energy is neglected and in the remaining electronic Hamiltonian, the nuclear positions appear as parameters. It is to be noted that this does not remove the interaction between the electrons and the nuclei, the electrons just "feel" the Coulomb potential of the clamped nuclei. This divides Eq. 7.15 into an ionic and an electronic part with the electronic Hamiltonian given by-

$$\begin{aligned}
&\left(-\sum_i \frac{\hbar^2}{2m_e}\frac{\partial^2}{\partial \vec{r_i}^2} - + \frac{e^2}{2}\sum_{i\neq j}\frac{1}{|\vec{r_i}-\vec{r_j}|}\right. \\
&+ \qquad \left. \frac{e^2}{2}\sum_{I\neq J}\frac{Z_I Z_J}{\left|\vec{R_I}-\vec{R_J}\right|} + \frac{e^2}{2}\sum_{i,I}\frac{Z_I}{\left|\vec{r_i}-\vec{R_I}\right|}\right)|\psi(\vec{r})\rangle \\
&= E(\vec{R})\psi_{\vec{R}}(\vec{r}) \qquad (7.16)
\end{aligned}$$

The energy $E(\vec{R})$ depends on the position of the nuclei chosen and can be mapped out by varying the position $\vec{R}$ and repeatedly solving the SWE. In the second step of the BO approximation, the nuclear kinetic energy is re-introduced and the SWE for the nuclei is solved-

$$\left(\sum_I \frac{\hbar^2}{2M_I}\frac{\partial^2}{\partial \vec{R_I}^2} + E(\vec{R})\right)\Phi(\vec{R}) = \epsilon\Phi(\vec{R}) \qquad (7.17)$$

This boils down to solving the SWE for N electrons moving in a periodic potential of a lattice or of the nuclei with some electron-electron interactions. However, even after the BO approximation, the resolution of the N electron wavefunction is not an easy task. To reduce this problem, several approximations are then used, as detailed below.

7.4.2 Density Functional Theory

The backbone of DFT are the two theorems of Hohenburg and Kohn [147] which explicit that it is possible to describe the ground state of a solid as a function of the electronic density $n(\vec{r})$. The total energy of the system is also a functional of the electronic density for which we can apply the variational principle- the unique density that minimises this functional is the ground state density $n_0(\vec{r})$.

First Theorem : For all electronic systems in interaction with an external potential $V_{ext}(\vec{r})$, the electronic ground state density $n_0(\vec{r})$ is uniquely determined by this potential.

Second Theorem : There exists a universal functional $E[n]$ (where the energy is expressed as a function of the electronic density), which is valid for all external potentials $V_{ext}(\vec{r})$. For a particular $V_{ext}(\vec{r})$, the ground state energy of the system is the value which minimises the energy functional $E[n]$ and its corresponding density n is the ground state density $n_0(\vec{r})$. Thus, there is a direct correspondence between the electronic density $n_0(\vec{r})$ and the external potential $V_{ext}(\vec{r})$. For a system of N interacting electrons in an external potential $V_{ext}(\vec{r})$, the ground state energy can be written down as-

$$\begin{aligned} E_0[n_0(\vec{r})] &= F[n_0(\vec{r})] + \int V_{ext}(\vec{r}) n_0(\vec{r}) d^3\vec{r} \\ &= \min_{n(\vec{r})} E_0[n_0(\vec{r})] = \min_{n(\vec{r})} \left[F[n(\vec{r})] + \int V_{ext}(\vec{r}) n(\vec{r}) d^3\vec{r} \right] \end{aligned} \tag{7.18}$$

where $F[n(\vec{r})]$ is the universal functional of Hohenburg and Kohn, which regroups the kinetic energy of the electrons and the electron-electron interactions, $n_0(\vec{r})$ is the density that minimises $E_0[n(\vec{r})]$ and $V_{ext}(\vec{r})$ is the external ionic potential. The Eq. 7.18 translates into determining the ground state by minimising the functional $F[n(\vec{r})]$ by imposing the conservation of the total number of electrons equal to N.

$$\int n(\vec{r}) d\vec{r} = N \tag{7.19}$$

Kohn and Sham proposed that the functional $F[n(\vec{r})]$ could be written down as-

$$F[n(\vec{r})] = T_0[n(\vec{r})] + \frac{e^2}{2}\int \frac{n(\vec{r})n(\vec{r'})}{\left|\vec{r}-\vec{r'}\right|} d^3\vec{r}d^3\vec{r'} + E_{xc}[n(\vec{r})] \tag{7.20}$$

where $T_0[n(\vec{r})]$ is the kinetic energy of a non-interacting gas of density $n(\vec{r})$, the second term is the Hartee energy and the third is the exchange-correlation energy. It is the last term where all the difficulty in the resolution of the equation lies and where all kinds of approximations will be used. We can choose to express the electronic density as a sum of the absolute value of orthonormal single electron wave functions $n(\vec{r}) = \sum_{i\in(occup)} |\phi_i(\vec{r})|^2$. This expression is trying to decouple a multi-electron problem to a single electron problem. However $n(\vec{r})$ can also be used to apply the variational principle which lead to a system of one-particle equations, without any interaction in an effective potential V_{KS}

$$V_{KS}n(\vec{r}) = V_{ext}n(\vec{r}) + V_{Hartree}n(\vec{r}) + V_{xc}n(\vec{r}) \tag{7.21}$$

which then leads to the Hamiltonian

$$H_{KS}\phi_i = (T_0 + V_{KS})\phi_i = \epsilon_i\phi_i \tag{7.22}$$

Here the first term is the kinetic energy, in the absence of interactions, which is defined as

$$T_0[n(\vec{r})] = -\sum_i f_i \int \phi_i^* \vec{r}\frac{\hbar^2\nabla^2}{2m_e}\phi_i(\vec{r})d^3\vec{r} \tag{7.23}$$

where f_i is the Fermi distribution at 0K. The Hartree potential $V_{Hartree}(\vec{r})$ is defined as

$$V_{Hartree}(\vec{r}) = \frac{e^2}{2}\int \frac{n(\vec{r'})}{\left|\vec{r}-\vec{r'}\right|} d^3\vec{r'} \tag{7.24}$$

and the density of the wave states can be obtained by the following equation-

$$n(\vec{r}) = \int_{-\infty}^{E_F} \left(\sum_i f_i|\phi_i(\vec{r})|^2\delta(E-\epsilon_i)\right) dE \tag{7.25}$$

The exchange potential is defined as the derivative of the exchange energy with respect to the density-

$$V_{xc}(\vec{r}) = \frac{\partial E_{xc}[n(\vec{r})]}{\partial n(\vec{r})} \tag{7.26}$$

Since the $V_{Hartree}$ and the V_{xc} are themselves dependent on the density and the density is a result of the resolution of Eq. 7.22, the density and the potential need to be solved in a self-consistent manner until a defined convergence criterion is reached. An initial single-particle wave-function ϕ_i^{in} is considered and the $n(\vec{r})^{in}$ is constructed from it which then define the potentials. Next the Eq. 7.22 is resolved to give rise to new electronic density $n(\vec{r})^{out}$. These two densities are compared - if they are extremely different, the procedure is repeated but if they are similar, self-consistency is achieved with respect to the convergence criterion, the procedure is stopped.

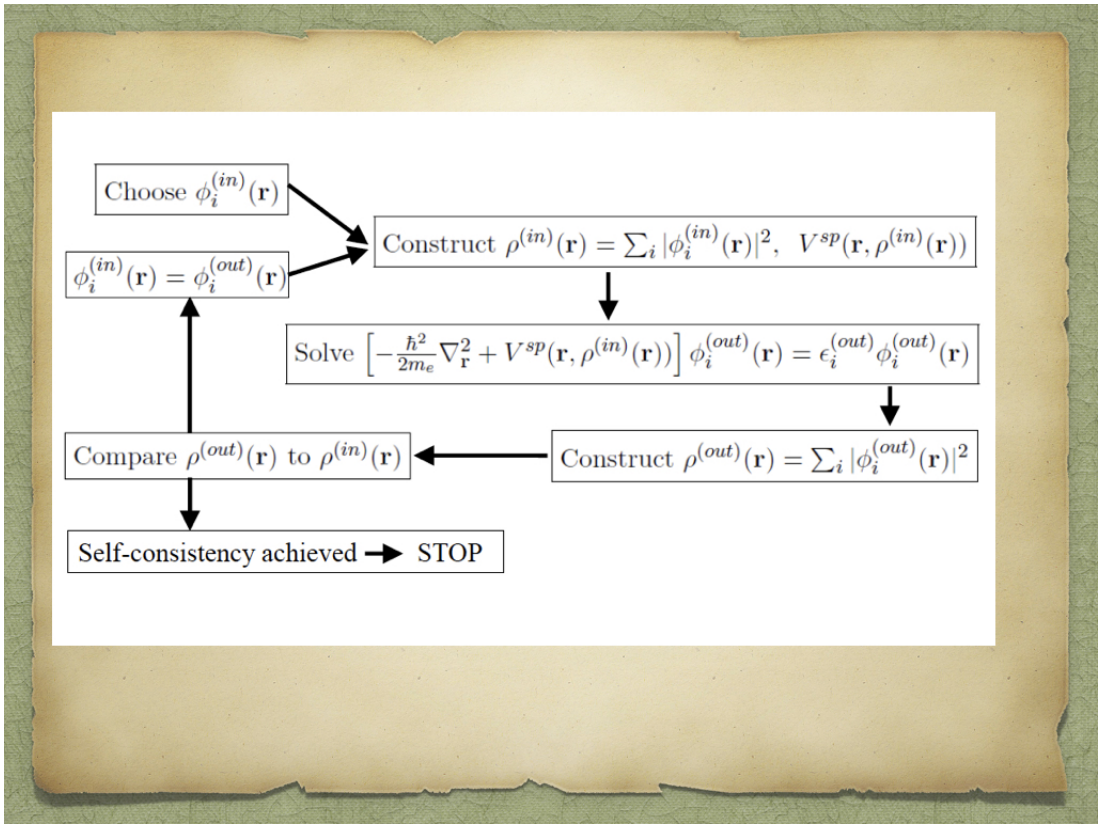

Figure 7.6: The self consistent cycle of evaluating the potential and the density of the wave function. Adapted from lectures given by Jacek Goniakowski in M2 Condensed Matter Physics, ENS.

7.4.3 LDA, GGA and other approximations

In the previous section, we saw that from an N body problem, we have simplified the problem to a single body problem. However, the exchange correlation potential still has to be approximated because it cannot be exact. There are various approximations that are used, notably the Local Density Approximation (LDA), Generalised Gradient Approach (GGA) or the hybrid functionals.

LDA approximation

The LDA approximation supposes that the exchange potential is a functional of the local electronic density where the system behaves locally like a homogeneous electron gas with density $n(\vec{r})$. The exchange correlation energy is then

$$E_{xc}^{LDA} = \int \epsilon_{xc}[n(\vec{r})]n(\vec{r})d^3\vec{r} \tag{7.27}$$

where $\epsilon_{xc}[n(\vec{r})]$ corresponds to the exchange correlation energy per electron for a homogeneous electron gas of density $\epsilon_{xc}[n(\vec{r})]$. $\epsilon_{xc}[n(\vec{r})]$ can further be divided into a local exchange energy and a local correlation energy-

$$\epsilon_{xc}[n(\vec{r})] = \epsilon_x[n(\vec{r})] + \epsilon_c[n(\vec{r})] \tag{7.28}$$

The exchange energy per electron can be approximated by the Dirac functional and the exact correlation energy has been obtained by Monte-Carlo simulations for some homogeneous electron gases. For the LDA calculations, those proposed by Perdew and Wang have been used[Perdew92]. A spin polarised version of the LDA, the LSDA (Local Spin Density Approximation) also exists which comprises of decomposing the total electronic density over the two spins. With the addition of spin, an additional degree of freedom appears in Eq. 7.22.

Generalised Gradient Approximation

The LDA approximation is based on the idea that the exchange energy functional can be approximated as a homogeneous electronic density even though in real life, that is not the case. To account for the deviations from the ideal homogeneous gas scenario, an approach which takes into account the local density and the gradients of the local density. This is the popular Generalised Gradient Approach (GGA) and the GGA energy is defined as-

$$E_{xc}^{GGA} = \int \epsilon_{xc}^{LDA}[n(\vec{r})] F_{xc}^{GGA}[n(\vec{r}), s] d^3\vec{r} \tag{7.29}$$

where $s = \left(\frac{\nabla n}{2k_F n}\right)_{n=n(\vec{r})}$. It is generalised by applying constraints like

$$n_x \quad < 0 \tag{7.30}$$

$$\int d^3r' n_x(\vec{r}, \vec{r'}) \quad = -1 \tag{7.31}$$

$$\int d^3r' n_c(\vec{r}, \vec{r'}) \quad = 0 \tag{7.32}$$

where n_x is the exchange and n_c the correlation density. The advantage of GGA over LDA is that it gives better precision over the total value of the energy and atomization energies and is more realistic for magnetic solids and gives an improved description of relative stability of the bulk phases. The GGA approximation gives better results for materials which have a variation of the spatial density like transition metal oxides for which the electrons are fairly localised. However, GGA softens the bonds, increases the lattice constants and decreases the bulk moduli favours lower coordination as compared to LDA. The version of GGA used for the calculations is Perdew-Burke-Ernzerhof (PBE) [134].

Beyond LDA and GGA

The major shortcomings of LDA or GGA lies in the auto-interaction of the electron, i.e. the interaction of an electron with itself which is introduced in the Hartree term and is not completely cancelled out by the exchange-correlation term. This is an inherent error because of a mean-field approach applied which neglects any coupling between the electrons.

There also lies another problem, that of the continuity of the energy and potential of the system; normally the potential should be a discontinuous function with discontinuities at integer values of N number of electrons. However, the potential and all the derivatives of the energy are continuous and the occupied and unoccupied states are all solutions of the same N electron problem while they should be the solutions of N-1 and N+1 systems respectively. This poses a problem specially in cases when the electron has an interplay between being delocalised and localisation at an atomic site, which is the case for the d-electrons. To correct this, various appoximations like the Hartree-Fock Method, the GWA approximation, the LDA+U approach or the Hybrid approach are proposed. We shall mainly focus on the LDA+U approach and carry out some calculations with the Hybrid functionals.

LDA+U approach

The basis of this approach is to add the correlations in the LDA or GGA (which we shall collectively call DFT) approach to better model the d electrons which are strongly correlated due to their narrow bandwidth. The theoretical model used for this approach is the Mott-Hubbard, which describes the interplay between a hopping integral t and Coulomb repulsion U between electrons of the same atom. The idea is to integrate the DFT with the Hubbard correlations uniquely added to the d orbitals. The Mott-Hubbard Hamiltonian is the following-

$$H_U = U/2 \sum_{m,m',\sigma} \hat{n}_{m,\sigma}\hat{n}_{m',-\sigma} + \frac{U-J}{2} \sum_{m\neq m'} \hat{n}_{m,\sigma}\hat{n}_{m',\sigma} \tag{7.33}$$

where U is the increase in the energy for placing an extra electron and J is the Hund's coupling. In a nutshell, the impact of U can be summarised in the following formula

$$\Delta V_{m,\sigma} = (U-J)(\frac{1}{2} - n^{\sigma}_{m}) \tag{7.34}$$

This will result in the occupied orbitals with $n^{\sigma}_{m} = 1$ to be pushed down by U-J and the unoccupied bands $n^{\sigma}_{m} = 0$ to be pushed up by U-J which better approximates the gap and the magnetic moments. The two parameters U and J are fixed by the user and normally

deduced by experiments or calculations. The resulting DFT+U functional penalizes partial occupation of the localized orbitals and favours disproportionation in fully occupied or completely empty orbitals. The Hybrid functionals are implicit density functionals formulated in terms of $E[\phi_i]$as compared to the explicit density functionals like LDA and GGA. If we take the exact exchange in terms of the wave functions ϕ_i

$$E_x[\phi_i] = \frac{1}{2}\int \frac{\sum_{i,j}\phi_i^*(\vec{r})\phi_j^*(\vec{r}')\phi_i(\vec{r}')\phi_j(\vec{r})}{|\vec{r}-\vec{r}'|}d^3\vec{r}d^3\vec{r}' \tag{7.35}$$

then the hybrid functional interpolation uses a part of the DFT and a part of the exact correlation energy in Eq. 7.35 with the mixing parameters taken from fitting thermochemical data and experimental energies.

List of Figures

List of Tables

Bibliography

[1] DI Khomskii and GA Sawatzky. “Interplay between spin, charge and orbital degrees of freedom in magnetic oxides”. In: Solid state communications 102.2-3 (1997), pp. 87–99.

[2] BG Idlis and Yu V Kopaev. “On the theory of phase transitions in vanadium oxides VnO2n-1 (magneli phases)”. In: Solid State Communications 45.3 (1983), pp. 301–304.

[3] Dirk Van Der Marel, Jacobus Lodevicus Martinu van Mechelen, and II Mazin. “Common Fermi-liquid origin of T 2 resistivity and superconductivity in n-type SrTiO 3”. In: Physical Review B 84.20 (2011), p. 205111.

[4] Maria Luisa Medarde. “Structural, magnetic and electronic properties of perovskites (R= rare earth)”. In: Journal of Physics: Condensed Matter 9.8 (1997), p. 1679.

[5] G Catalan. “Progress in perovskite nickelate research”. In: Phase Transitions 81.7-8 (2008), pp. 729–749.

[6] HY Hwang et al. “Lattice Effects on the Magnetoresistance in Doped LaMn O 3”. In: Physical review letters 75.5 (1995), p. 914.

[7] A Ohtomo and HY Hwang. “A high-mobility electron gas at the LaAlO 3/SrTiO 3 heterointerface”. In: Nature 427.6973 (2004), p. 423.

[8] AF Santander-Syro et al. “Two-dimensional electron gas with universal subbands at the surface of SrTiO3”. In: Nature 469.7329 (2011), pp. 189–193.

[9] AF Santander-Syro et al. “Giant spin splitting of the two-dimensional electron gas at the surface of SrTiO3”. In: Nature materials 13.12 (2014), pp. 1085–1090.

[10] Alexander K Tagantsev. “Electric polarization in crystals and its response to thermal and elastic perturbations”. In: Phase Transitions: A Multinational Journal 35.3-4 (1991), pp. 119–203.

[11] L Eric Cross. “Flexoelectric effects: Charge separation in insulating solids subjected to elastic strain gradients”. In: Journal of Materials Science 41.1 (2006), pp. 53–63.

[12] G Logvenov, A Gozar, and I Bozovic. “High-temperature superconductivity in a single copper-oxygen plane”. In: Science 326.5953 (2009), pp. 699–702.

[13] GA Baraff, Joel A Appelbaum, and DR Hamann. “Self-consistent calculation of the electronic structure at an abrupt GaAs-Ge interface”. In: Physical Review Letters 38.5 (1977), p. 237.

[14] WA Harrison et al. “Polar heterojunction interfaces”. In: Physical Review B 18.8 (1978), p. 4402.

[15] Jun Nishimura et al. “Controlled carrier generation at a polarity-discontinued perovskite heterointerface”. In: Japanese journal of applied physics 43.8A (2004), p. L1032.

[16] Liping Yu and Alex Zunger. “A polarity-induced defect mechanism for conductivity and magnetism at polar–nonpolar oxide interfaces”. In: Nature communications 5 (2014), p. 5118.

[17] Alexandre I Buzdin. “Proximity effects in superconductor-ferromagnet heterostructures”. In: Reviews of modern physics 77.3 (2005), p. 935.

[18] Pavlo Zubko et al. “Interface physics in complex oxide heterostructures”. In: Annu. Rev. Condens. 2.1 (2011), pp. 141–165.

[19] Julie A Bert et al. “Direct imaging of the coexistence of ferromagnetism and superconductivity at the LaAlO 3/SrTiO 3 interface”. In: Nature physics 7.10 (2011), p. 767.

[20] Alexander Brinkman et al. “Magnetic effects at the interface between non-magnetic oxides”. In: Nature materials 6.7 (2007), p. 493.

[21] X Wang et al. “Electronic phase separation at the LaAlO 3/SrTiO 3 interface”. In: Nature communications 2 (2011), p. 188.

[22] R Matzdorf et al. “Ferromagnetism stabilized by lattice distortion at the surface of the p-wave superconductor Sr2RuO4”. In: Science 289.5480 (2000), pp. 746–748.

[23] Matthew Dawber et al. “New phenomena at the interfaces of very thin ferroelectric oxides”. In: Journal of Physics: Condensed Matter 20.26 (2008), p. 264015.

[24] SK t Streiffer et al. “Observation of Nanoscale 180° Stripe Domains in Ferroelectric P b T i O 3 Thin Films”. In: Physical review letters 89.6 (2002), p. 067601.

[25] Tobias C Rödel et al. “Two-dimensional electron systems in ATiO3 perovskites (A= Ca, Ba, Sr): control of orbital hybridization and order”. In: arXiv preprint arXiv:1705.10755 (2017).

[26] PD Dresselhaus et al. “Observation of spin precession in GaAs inversion layers using antilocalization”. In: Physical review letters 68.1 (1992), p. 106.

[27] Junsaku Nitta et al. “Gate Control of Spin-Orbit Interaction in an Inverted I n 0.53 G a 0.47 As/I n 0.52 A l 0.48 As Heterostructure”. In: Physical Review Letters 78.7 (1997), p. 1335.

[28] JB Miller et al. “Gate-controlled spin-orbit quantum interference effects in lateral transport”. In: Physical review letters 90.7 (2003), p. 076807.

[29] AD Caviglia et al. “Tunable Rashba spin-orbit interaction at oxide interfaces”. In: Physical review letters 104.12 (2010), p. 126803.

[30] David Hsieh et al. “Observation of time-reversal-protected single-Dirac-cone topological-insulator states in Bi 2 Te 3 and Sb 2 Te 3”. In: Physical review letters 103.14 (2009), p. 146401.

[31] Yuqi Xia et al. “Observation of a large-gap topological-insulator class with a single Dirac cone on the surface”. In: Nature physics 5.6 (2009), p. 398.

[32] Xi Dai et al. “Helical edge and surface states in HgTe quantum wells and bulk insulators”. In: Physical Review B 77.12 (2008), p. 125319.

[33] Stanislav Chadov et al. “Tunable multifunctional topological insulators in ternary Heusler compounds”. In: Nature materials 9.7 (2010), p. 541.

[34] Hsin Lin et al. “Half-Heusler ternary compounds as new multifunctional experimental platforms for topological quantum phenomena”. In: Nature materials 9.7 (2010), p. 546.

[35] C Bareille et al. “Two-dimensional electron gas with six-fold symmetry at the (111) surface of ktao 3”. In: Scientific reports 4 (2014), p. 3586.

[36] N. D. Mermin. “The topological theory of defects in ordered media”. In: Rev. Mod. Phys. 51 (3 1979), pp. 591–648.

[37] K. v. Klitzing, G. Dorda, and M. Pepper. “New Method for High-Accuracy Determination of the Fine-Structure Constant Based on Quantized Hall Resistance”. In: Phys. Rev. Lett. 45 (6 1980), pp. 494–497.

[38] Steven M Girvin. “Introduction to the fractional quantum Hall effect”. In: The Quantum Hall Effect Springer, 2005, pp. 133–162.

[39] F Duncan M Haldane. “Model for a quantum Hall effect without Landau levels: Condensed-matter realization of the” parity anomaly””. In: Physical Review Letters 61.18 (1988), p. 2015.

[40] Charles L Kane and Eugene J Mele. “Quantum spin Hall effect in graphene”. In: Physical review letters 95.22 (2005), p. 226801.

[41] Charles L Kane and Eugene J Mele. “Z 2 topological order and the quantum spin Hall effect”. In: Physical review letters 95.14 (2005), p. 146802.

[42] B Andrei Bernevig, Taylor L Hughes, and Shou-Cheng Zhang. “Quantum spin Hall effect and topological phase transition in HgTe quantum wells”. In: Science 314.5806 (2006), pp. 1757–1761.

[43] Joel E Moore and Leon Balents. “Topological invariants of time-reversal-invariant band structures”. In: Physical Review B 75.12 (2007), p. 121306.

[44] Liang Fu and Charles L Kane. “Topological insulators with inversion symmetry”. In: Physical Review B 76.4 (2007), p. 045302.

[45] YL Chen et al. “Experimental realization of a three-dimensional topological insulator, Bi2Te3”. In: science 325.5937 (2009), pp. 178–181.

[46] DJ Chadi and Marvin L Cohen. “Electronic Structure of Hg 1- x Cd x Te Alloys and Charge-Density Calculations Using Representative k Points”. In: Physical Review B 7.2 (1973), p. 692.

[47] Timothy H Hsieh et al. “Topological crystalline insulators in the SnTe material class”. In: Nature communications 3 (2012), p. 982.

[48] P Dziawa et al. “Topological crystalline insulator states in Pb 1- x Sn x Se”. In: Nature materials 11.12 (2012), p. 1023.

[49] Yoichi Ando and Liang Fu. “Topological crystalline insulators and topological superconductors: from concepts to materials”. In: Annu. Rev. Condens. Matter Phys. 6.1 (2015), pp. 361–381.

[50] Y Tanaka et al. “Experimental realization of a topological crystalline insulator in SnTe”. In: Nature Physics 8.11 (2012), p. 800.

[51] Junwei Liu, Wenhui Duan, and Liang Fu. “Two types of surface states in topological crystalline insulators”. In: Physical Review B 88.24 (2013), p. 241303.

[52] David Hsieh et al. “A topological Dirac insulator in a quantum spin Hall phase”. In: Nature 452.7190 (2008), p. 970.

[53] Rahul Roy. “Topological phases and the quantum spin Hall effect in three dimensions”. In: Physical Review B 79.19 (2009), p. 195322.

[54] Haijun Zhang et al. “Topological insulators in Bi 2 Se 3, Bi 2 Te 3 and Sb 2 Te 3 with a single Dirac cone on the surface”. In: Nature physics 5.6 (2009), p. 438.

[55] Jérome Cayssol. “Introduction to Dirac materials and topological insulators”. In: Comptes Rendus Physique 14.9-10 (2013). review in topical issue of ”Comptes Rendus de l’Académie des Sciences (Physique)” devoted to topological insulators and Dirac matter, pp. 760–778.

[56] Chaoxing Liu et al. “Quantum spin Hall effect in inverted type-II semiconductors”. In: Physical review letters 100.23 (2008), p. 236601.

[57] Markus König et al. “The quantum spin Hall effect: theory and experiment”. In: Journal of the Physical Society of Japan 77.3 (2008), p. 031007.

[58] Ivan Knez, Rui-Rui Du, and Gerard Sullivan. “Evidence for helical edge modes in inverted InAs/GaSb quantum wells”. In: Physical review letters 107.13 (2011), p. 136603.

[59] Chengwang Niu et al. “Two-dimensional topological crystalline insulator phase in quantum wells of trivial insulators”. In: 2D Materials 3.2 (2016), p. 025037.

[60] Roman Jackiw. “Fractional charge and zero modes for planar systems in a magnetic field”. In: Physical Review D 29.10 (1984), p. 2375.

[61] Gordon W Semenoff. “Condensed-matter simulation of a three-dimensional anomaly”. In: Physical Review Letters 53.26 (1984), p. 2449.

[62] Eduardo Fradkin, Elbio Dagotto, and Daniel Boyanovsky. “Physical realization of the parity anomaly in condensed matter physics”. In: Physical review letters 57.23 (1986), p. 2967.

[63] Yi Zhang et al. “Crossover of the three-dimensional topological insulator Bi 2 Se 3 to the two-dimensional limit”. In: Nature Physics 6.8 (2010), p. 584.

[64] K Alex Müller and H Burkard. “SrTi O 3: An intrinsic quantum paraelectric below 4 K”. In: Physical Review B 19.7 (1979), p. 3593.

[65] Fedwa El-Mellouhi et al. “Structural phase transitions of the metal oxide perovskites SrTiO 3, LaAlO 3, and LaTiO 3 studied with a screened hybrid functional”. In: Physical Review B 87.3 (2013), p. 035107.

[66] M Salluzzo et al. “Orbital reconstruction and the two-dimensional electron gas at the LaAlO 3/SrTiO 3 interface”. In: Physical review letters 102.16 (2009), p. 166804.

[67] Hiromi Unoki and Tunetaro Sakudo. “Electron spin resonance of Fe3+ in SrTiO3 with special reference to the 110 K phase transition”. In: Journal of the Physical Society of Japan 23.3 (1967), pp. 546–552.

[68] Jun John Sakurai and Jim Napolitano. Modern quantum mechanics. Cambridge University Press, 2017.

[69] Zhicheng Zhong, Anna Tóth, and Karsten Held. “Theory of spin-orbit coupling at LaAlO 3/SrTiO 3 interfaces and SrTiO 3 surfaces”. In: Physical Review B 87.16 (2013), p. 161102.

[70] W. Meevasana et al. “Creation and control of a two-dimensional electron liquid at the bare SrTiO3 surface”. In: Nature Materials 10.2 (2011), pp. 114–118.

[71] Roland Winkler. “Spin-orbit coupling effects in two-dimensional electron and hole systems”. In: Springer Tracts in Modern Physics 191 (2006), pp. 153–156.

[72] S. McKeownWalker et al. “Absence of giant spin splitting in the two-dimensional electron liquid at the surface of $\mathrm{SrTiO_3}$ (001)”. In: Phys. Rev. B 93 (24 2016), p. 245143.

[73] K Ueno et al. “Electric-field-induced superconductivity in an insulator”. In: Nature materials 7.11 (2008), p. 855.

[74] Tsuneya Ando, Alan B Fowler, and Frank Stern. “Electronic properties of two-dimensional systems”. In: Reviews of Modern Physics 54.2 (1982), p. 437.

[75] Alexandre Fete. “Magnetotransport experiments at the LaAlO3/SrTiO3 interface”. PhD thesis. University of Geneva, 2014.

[76] Johan Biscaras. “Supraconductivité bi-dimensionnelle à l’interface d’Oxydes de Titane”. PhD thesis. Paris 6, 2012.

[77] Massimiliano Stengel. “First-principles modeling of electrostatically doped perovskite systems”. In: Physical review letters 106.13 (2011), p. 136803.

[78] Guru Khalsa, Byounghak Lee, and AH MacDonald. “Theory of t 2 g electron-gas Rashba interactions”. In: Physical Review B 88.4 (2013), p. 041302.

[79] Manali Vivek, Mark O Goerbig, and Marc Gabay. “Topological states at the (001) surface of SrTiO 3”. In: Physical Review B 95.16 (2017), p. 165117.

[80] M. O. Goerbig et al. “Tilted anisotropic Dirac cones in quinoid-type graphene and $\alpha-(\mathrm{BEDT\text{-}TTF})_2\mathrm{I}_3$”. In: Phys. Rev. B 78 (4 2008), p. 045415.

[81] M. O. Goerbig et al. In: EPL 85 (2009), p. 57005.

[82] NC Plumb et al. “Mixed dimensionality of confined conducting electrons in the surface region of SrTiO 3”. In: Physical review letters 113.8 (2014), p. 086801.

[83] T. C. Rödel et al. “Universal Fabrication of 2D Electron Systems in Functional Oxides”. In: Advanced Materials 28.10 (2016), pp. 1976–1980.

[84] Juan Shen et al. “Ab initio study of the two-dimensional metallic state at the surface of SrTiO3: Importance of oxygen vacancies”. In: Phys. Rev. B 86.19 (2012).

[85] Harald O. Jeschke, Juan Shen, and Roser Valenti. “Localized versus itinerant states created by multiple oxygen vacancies in SrTiO3”. In: New Journal of Physics 17 (2015).

[86] V. N. Strocov, C. Cancellieri, and A. S. Mishchenko. “Electrons and polarons at oxide interfaces explored by soft-X-ray ARPES”. In: ArXiv e-prints (Dec. 2016). arXiv: 1612.05791 [cond-mat.mes-hall].

[87] NC Bristowe, PB Littlewood, and Emilio Artacho. “Surface defects and conduction in polar oxide heterostructures”. In: Physical Review B 83.20 (2011), p. 205405.

[88] Yun Li et al. “Formation of oxygen vacancies and charge carriers induced in the n-type interface of a LaAlO 3 overlayer on SrTiO 3 (001)”. In: Physical Review B 84.24 (2011), p. 245307.

[89] Pietro Delugas et al. “Spontaneous 2-dimensional carrier confinement at the n-type SrTiO 3/LaAlO 3 interface”. In: Physical review letters 106.16 (2011), p. 166807.

[90] M Sing et al. “Profiling the interface electron gas of LaAlO 3/SrTiO 3 heterostructures with hard X-ray photoelectron spectroscopy”. In: Physical Review Letters 102.17 (2009), p. 176805.

[91] NC Bristowe et al. “Proposal of a One-Dimensional Electron Gas in the Steps at the LaAlO 3- SrTiO 3 Interface”. In: Physical review letters 108.16 (2012), p. 166802.

[92] Vladimir N Strocov, Claudia Cancellieri, and Andrey S Mishchenko. “Electrons and polarons at oxide interfaces explored by soft-X-ray ARPES”. In: Spectroscopy of Complex Ox Springer, 2018, pp. 107–151.

[93] AEM Smink et al. “Gate-Tunable Band Structure of the LaAlO 3- SrTi O 3 Interface”. In: Physical review letters 118.10 (2017), p. 106401.

[94] NC Plumb et al. “From the SrTiO3 Surface to the LAlO3/SrTiO3 Interface: How thickness is critical”. In: arXiv preprint arXiv:1304.5948 (2013).

[95] S Gariglio et al. “Superconductivity at the LaAlO3/SrTiO3 interface”. In: Journal of Physics: Cond 21.16 (2009), p. 164213.

[96] Beena Kalisky et al. “Critical thickness for ferromagnetism in LaAlO 3/SrTiO 3 heterostructures”. In: Nature communications 3 (2012), p. 922.

[97] Patrick Gallagher et al. “A high-mobility electronic system at an electrolyte-gated oxide surface”. In: Nature communications 6 (2015), p. 6437.

[98] Russell S Deacon et al. “Josephson radiation from gapless Andreev bound states in HgTe-based topological junctions”. In: arXiv preprint arXiv:1603.09611 (2016).

[99] Liang Fu and Charles L Kane. “Josephson current and noise at a superconductor/quantum-spin-Hall-insulator/superconductor junction”. In: Physical Review B 79.16 (2009), p. 161408.

[100] J. Wiedenmann et al. “4π-periodic Josephson supercurrent in HgTe-based topological Josephson junctions”. In: Nature Communications 7 (2016), pp. 10303–10309.

[101] Anil Murani. “Supraconductivity par effet de proximité en présence de couplage spin-orbite en régime statique et dynamique”. PhD thesis. Université Paris Saclay, 2016.

[102] Shu-Ping Lee. Signatures of Topological Superconductors. California Institute of Technology, 2015.

[103] TC Rödel et al. “Orientational tuning of the Fermi sea of confined electrons at the SrTiO 3 (110) and (111) surfaces”. In: Physical Review Applied 1.5 (2014), p. 051002.

[104] Menyoung Lee et al. “Electrolyte Gate-Controlled Kondo Effect in $\mathrm{SrTiO_3}$”. In: Phys. Rev. Lett. 107 (25 2011), p. 256601.

[105] T. Taniuchi et al. “Imaging of room-temperature ferromagnetic nano-domains at the surface of a non-magnetic oxide”. In: Nature Communications 7 (2016), pp. 11781–11786.

[106] Michaela Altmeyer et al. “Magnetism, Spin Texture, and In-Gap States: Atomic Specialization at the Surface of Oxygen-Deficient SrTiO 3”. In: Physical review letters 116.15 (2016), p. 157203.

[107] J. A. Bert et al. “Direct imaging of the coexistence of ferromagnetism and superconductivity at the $LaAlO_3/SrTiO_3$ interface”. In: Nat. Phys. 7 (2011), pp. 767–771.

[108] J. A. Sulpizio et al. “Nanoscale Phenomena in Oxide Heterostructures”. In: Annual Review of Mate 44.1 (2014), pp. 117–149. eprint: http://dx.doi.org/10.1146/annurev-matsci-070813-113437.

[109] Marco Salluzzo. “Electronic Reconstruction at the Interface Between Band Insulating Oxides: The LaAlO3/SrTiO3 System”. In: Oxide Thin Films, Multilayers, and Nanocomposite Ed. by Paolo Mele et al. Cham: Springer International Publishing, 2015, pp. 181–211. ISBN: 978-3-319-14478-8.

[110] S McKeown Walker et al. “Control of a two-dimensional electron gas on SrTiO 3 (111) by atomic oxygen”. In: Physical review letters 113.17 (2014), p. 177601.

[111] E Maniv et al. “Strong correlations elucidate the electronic structure and phase diagram of LaAlO 3/SrTiO 3 interface”. In: Nature communications 6 (2015), p. 8239.

[112] Zhuoyu Chen et al. “Dual-Gate Modulation of Carrier Density and Disorder in an Oxide Two-Dimensional Electron System”. In: Nano letters 16.10 (2016), pp. 6130–6136.

[113] C Bell et al. “Dominant mobility modulation by the electric field effect at the LaAlO 3/SrTiO 3 interface”. In: Physical review letters 103.22 (2009), p. 226802.

[114] W Liu et al. “Magneto-transport study of top-and back-gated LaAlO3/SrTiO3 heterostructures”. In: APL materials 3.6 (2015), p. 062805.

[115] PK Rout, E Maniv, and Y Dagan. “Nonmonotonic superconductivity and spin-orbit interaction across the phase diagram of the (111) LaAlO _3/SrTiO _3 interface”. In: arXiv preprint arXiv:1706.01717 (2017).

[116] Oliver Hijano Cubelos. “Hétérostructures supraconductrices et isolants topologiques”. PhD thesis. Paris Saclay, 2015.

[117] James M Rondinelli and Nicola A Spaldin. “Structure and properties of functional oxide thin films: insights from electronic-structure calculations”. In: Advanced materials 23.30 (2011), pp. 3363–3381.

[118] RI Eglitis and David Vanderbilt. “Ab initio calculations of the atomic and electronic structure of CaTiO 3 (001) and (011) surfaces”. In: Physical Review B 78.15 (2008), p. 155420.

[119] RI Eglitis. “Ab initio calculations of SrTiO 3, BaTiO 3, PbTiO 3, CaTiO 3, SrZrO 3, PbZrO 3 and BaZrO 3 (001),(011) and (111) surfaces as well as F centers, polarons, KTN solid solutions and Nb impurities therein”. In: International Journal of Modern Physics B 28.17 (2014), p. 1430009.

[120] K Ueda et al. “Study on electronic structure of CaTiO3 by spectroscopic measurements and energy band calculations”. In: Journal of Physics: Condensed Matter 11.17 (1999), p. 3535.

[121] M Adachi et al. “CaTiO3, 1A-7”. In: Oxides. Springer, 2002, pp. 1–18.

[122] A Linz Jr and K Herrington. “Electrical and optical properties of synthetic calcium titanate crystal”. In: The Journal of Chemical Physics 28.5 (1958), pp. 824–825.

[123] Cheng-Liang Huang and Ming-Hung Weng. “Improved high Q value of MgTiO3-CaTiO3 microwave dielectric ceramics at low sintering temperature”. In: Materials Research Bulle 36.15 (2001), pp. 2741–2750.

[124] RP Wang and CJ Tao. “Nb-doped CaTiO3 transparent semiconductor thin films”. In: Journal of crystal growth 245.1-2 (2002), pp. 63–66.

[125] A Krause et al. “Investigation of band gap and permittivity of the perovskite CaTiO3 in ultrathin layers”. In: Journal of Physics D: Applied Physics 48.41 (2015), p. 415304.

[126] Satoshi Sasaki et al. “Orthorhombic perovskite CaTiO3 and CdTiO3: structure and space group”. In: Acta Crystallographica Section C: Crystal Structure Communications 43.9 (1987), pp. 1668–1674.

[127] Masatomo Yashima and Roushown Ali. “Structural phase transition and octahedral tilting in the calcium titanate perovskite CaTiO3”. In: Solid State Ionics 180.2-3 (2009), pp. 120–126.

[128] RH Buttner and EN Maslen. “Electron difference density and structural parameters in CaTiO3”. In: Acta Crystallographica Section B: Structural Science 48.5 (1992), pp. 644–649.

[129] Stefan Muff et al. “Observation of a two-dimensional electron gas at CaTiO3 film surfaces”. In: Applied Surface Science 432 (2018), pp. 41–45.

[130] Richard M Martin. Electronic structure: basic theory and practical methods. Cambridge university press, 2004.

[131] Rémi Arras. “Structure électronique au voisinage des défauts de la magnétite et des interfaces Fe3O4/MgO (001)”. PhD thesis. Université de Toulouse, Université Toulouse III-Paul Sabatier, 2010.

[132] G. Kresse and J. Furthmuller. “Efficient Iterative Schemes for ab initio Total Energy Calculations Using a Plane-Wave Basis Set”. In: Phys. Rev. B 54 (1996), pp. 11169–11186.

[133] G. Kresse and J. Hafner. “Ab initio Molecular Dynamics for Liquid Metals”. In: Phys. Rev. B 47 (1993), pp. 558–561.

[134] J. P. Perdew et al. “Atoms, molecules, solids, and surfaces: Applications of the generalized gradient approximation for exchange and correlation.” In: Phys. Rev. B 46 (1992), pp. 6671–6687.

[135] S. L. Dudarev et al. “Electron-Energy-Loss Spectra and the Structural Stability of Nickel Oxide: An LSDA+U Study”. In: Phys. Rev. B 57 (1998), pp. 1505–1509.

[136] J. Heyd, G. E. Scuseria, and M. Ernzerhof. “Hybrid functionals based on a screened Coulomb potential”. In: J. Chem. Phys. 118 (2003), p. 8207.

[137] J. Paier et al. “Screened hybrid density functionals applied to solids”. In: J. Chem. Phys. 124 (2006), p. 154709.

[138] P. E. Blöchl. “Projector Augmented-Wave Method”. In: Phys. Rev. B 50 (1994), pp. 17953–17979.

[139] G. Kresse and J. Joubert. “From Ultrasoft Pseudopotentials to the Projector Augmented-Wave Method”. In: Phys. Rev. B 59 (1999), pp. 1758–1775.

[140] Harald O Jeschke, Juan Shen, and Roser Valentí. “Localized versus itinerant states created by multiple oxygen vacancies in SrTiO3”. In: New Journal of Physics 17.2 (2015), p. 023034.

[141] Jean-Michel Carter et al. “Semimetal and topological insulator in perovskite iridates”. In: Physical Review B 85.11 (2012), p. 115105.

[142] Yun Li, Xinyuan Wei, and Jaejun Yu. “Inevitable high density of oxygen vacancies on the surface of LaAlO3/SrTiO3 heterostructures”. In: arXiv preprint arXiv:1804.04502 (2018).

[143] Rémi Arras et al. “Tuning the two-dimensional electron gas at the LaAlO 3/SrTiO 3 (001) interface by metallic contacts”. In: Physical Review B 85.12 (2012), p. 125404.

[144] Diogo Castro Vaz et al. “Growth and Electrostatic/chemical Properties of Metal/LaAlO3/SrTiO3 Heterostructures.” In: Journal of visualized experiments: JoVE 132 (2018).

[145] E Lesne et al. “Highly efficient and tunable spin-to-charge conversion through Rashba coupling at oxide interfaces”. In: Nature materials 15.12 (2016), p. 1261.

[146] Yongsu Kwak et al. “Interplay between superconductivity and magnetism in one-unit-cell LaAlO3 capped with SrTiO3”. In: arXiv preprint arXiv:1801.08022 (2018).

[147] Walter Kohn and Lu Jeu Sham. “Self-consistent equations including exchange and correlation effects”. In: Physical review 140.4A (1965), A1133.